Comprehensive review of the recent advances in PV/T system with loop-pipe configuration and nanofluid

Yuanlong Cui [a], Jie Zhu [b,*], Stamatis Zoras [a], Jizhe Zhang [c]

[a] Department of Built Environment, College of Engineering and Technology, University of Derby, Derby, DE22 3AW, UK

[b] Department of Architecture and Built Environment, University of Nottingham, Nottingham, NG7 2RD, UK

[c] School of Qilu Transportation, Shandong University, Jinan, 250061, China

Contents

* Corresponding author. Tel: +44-115-8466141 Fax: +44-115-951315
E-mail address: jie.zhu@nottingham.ac.uk

Abstract

Solar photovoltaic/thermal technology has been widely utilized in building service area as it generates thermal and electrical energy simultaneously. In order to improve the photovoltaic/thermal system performance, nanofluids are employed as the thermal fluid owing to its high thermal conductivity. This paper summarizes the state-of-the-art of the photovoltaic/thermal systems with different loop-pipe configurations (including heat pipe, vacuum tube, roll-bond, heat exchanger, micro-channel, U-tube, triangular tube and heat mat) and nanoparticles (including Copper-oxide, Aluminium-oxide, Silicon carbide, Tribute, Magnesium-oxide, Cerium-oxide, Tungsten-oxide, Titanium-oxide, Zirconia-oxide, Graphene and Carbon). The influences of the critical parameters like nanoparticle optical and thermal properties, volume fraction, mass flux and mass flow rates, on the photovoltaic/thermal system performance are for the optimum energy efficiency. Furthermore, the structure and manufacturing of solar cells, micro-thermometry analysis of solar cells and recycling process of photovoltaic panels are explored. At the end, the standpoints, recommendations and potential future development on the solar photovoltaic/thermal system with various configurations and nanofluids are deliberated to overcome the barriers and challenges for the practical application. This study demonstrates that the advanced photovoltaic/thermal configuration could improve the system energy efficiency approximately 15%-30% in comparison with the conventional type whereas the nanofluid is able to boost the efficiency around 10%-20% compared to that with traditional working fluid.

Keywords: PV/T system configuration; Nanofluids; Electrical output; Electrical efficiency; Thermal output; Thermal efficiency

1. Introduction

With the COVID-19 and post-COVID manufacturing changes, the greenhouse gases (GHG) emission has become one of the most vital social economics issues [1]. The clean energy and climate change associations have spent decades tackling a crisis that has been unfolding in motion [2]. For example, the Paris Agreement puts forward to reinforce the worldwide response to the threat of climate change by limiting the mean global temperature growth at a maximum of 2 °C in comparison with pre-industrial levels [3]. The EU's nationally determined contribution (NDC) under the Paris Agreement aims to decrease the GHG emission by at least 40% by 2030 in comparison with 1990 levels [3]. Meanwhile, the World Green Building Council (WGBC) has issued a new vision to reduce 40% GHG emissions by 2030, and achieve 100% net zero emission buildings by 2050 [4]. Furthermore, in order to bring about the carbon neutral, the city must cut as much carbon emissions as possible that come from our actions as construction, industry, business, agriculture and transport [5]. Therefore, the scientists are seeking for affordable and clean energy suppliers to resolve the global warming issue. Solar energy is one of the most promising renewable resources, which can solve the challenges associated with the climate change and environmental contamination. In terms of current solar energy technologies, photovoltaic/thermal (PV/T) system is the most efficient and widely deployed owing to its stability, non-polluting, security and good visibility features [6, 7]. To be more specific, the PV technology and solar thermal could be integrated together to form a single module and produce electricity and heat simultaneously based on the excitation of electrons in the semiconducting material [8-10]. There are various configurations for the PV/T pipe-loop. As presented in Fig. 1, they are mainly classified into traditional configurations like heat pipe, vacuum tube, roll-bond and heat exchanger as well as advanced PV/T configurations including micro-channel, U-tube, triangular tube and heat mat.

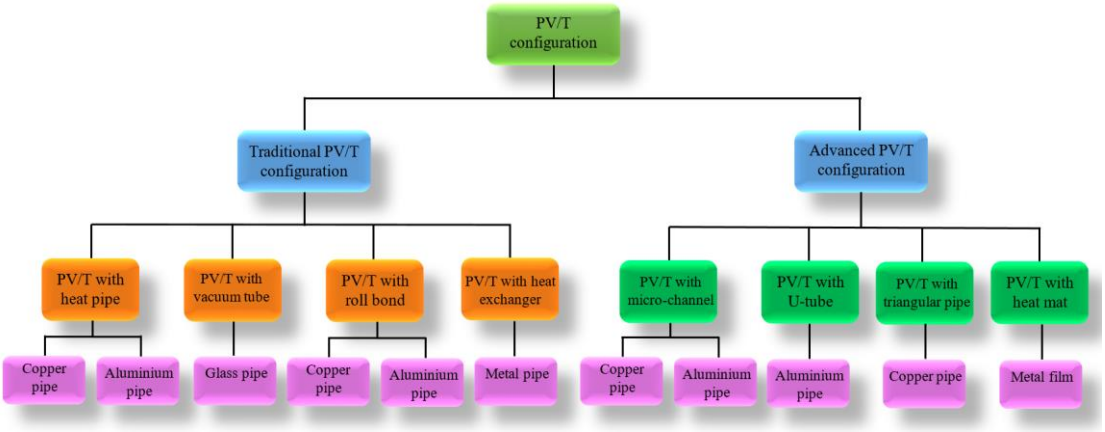

Fig. 1. Diagram of PV/T loop-pipe configurations

During the process of converting solar energy into thermal energy, some irreversibilities are produced to reduce the system performance. In order to solve this issue, the techniques based on the first and second laws of thermodynamics are able to detect these irreversibilities and could be utilized as a guideline for system performance enhancement. Kalogirou et al. [11] presented a roundup of exergy analyses of solar thermal systems based on the first and second laws of thermodynamics, and summarized the applications. Chauhan et al. [12] developed a simplified and generalized solar PV/T model to calculate the minimum entropy

generation depended on the second law of thermodynamics, and concluded that the minimum entropy generation of PVT system is in the range from 500 W to 526 W and the maximum temperature drop could reach 18 °C resulting in 8.6% of the electrical efficiency improvement. Ooshaksaraei et al. [13] established a mathematical model to evaluate the energy and exergy performance of the PV/T system, and revealed that the exergy efficiency could achieve 8.5% when the packing factor is 0.7, meanwhile, the system energy efficiency could be improved from 39% to 55% when the flow rate varies from 0.038 kg/hour to 0.14kg/hour. Rashidi et al. [14] performed a review with regards to the entropy production of various solar thermal energy systems to investigate system irreversibility. Their review indicates that it is an efficient solution in terms of the entropy generation minimization approach to optimal the solar energy system design. Gholampour et al. [15] evaluated the influences of some parameters like the fin number and height, packing factor and diameter of outlet based on the first and second laws of thermodynamics, and demonstrated that the increasing of the fin number and height has an effectively influence on the first- and second-law efficiencies. Additionally, when the packing factor is improved, it has a more considerable effect on the second law efficiency compared with the first-law efficiency. By comparison, the growth of the diameter of outlet has a positive influence on the first-law efficiency whereas it has a negative influence on the second-law efficiency.

Additionally, it is well known that the temperature reduction in PV panel leads to an increasing of the electrical efficiency [16, 17], and the high PV panel temperature is attributed to the poor heat dissipation [17]. Therefore, the effective cooling of the PV panel not only enhances the electrical efficiency, but also extends its lifetime of service because of the thermal stresses reduction [18]. So many efficient cooling technologies, including the active cooling [19, 20], passive cooling [21-23], heat pipe cooling [24, 25] and nanolfuids cooling [26-28] techniques, have been developed to tackling heat dissipation of PV panel in recently year. To be more specific, Farhana et al. [19] explored the effect of air cooling on the polycrystalline PV cell and compared the temperature difference between one with and the other without cooling, and discovered that the electrical efficiency improvement and temperature drop of the PV cell could achieve up to 8.9% and 12 °C, respectively. Du et al. [20] utilized two aluminium pipes installed at the back of a PV panel to cool the monocrystalline PV panel, and found that the efficiency could be enhanced by about 0.8% and the surface temperature of the PV cell could be decreased by 60 °C. Rosa-Clot et al. [21] employed the water passive cooling technique to cool down a PV panel, and demonstrated that the electrical efficiency is boosted by 20% and the surface temperature is maintained at 30 °C. Chandrasekar et al. [22] cooled down a monocrystalline PV module by using the capillary effect method, and discovered that the efficiency could be increased by up to 10.4 % in comparison with the non-cooled module. Maiti et al. [23] implemented a testing study of a V-through reflective panel to cool down its surface by using the passive cooling method, and revealed that the temperature reduction is in the range between 65 °C and 85 °C, resulting in 55% of electrical efficiency improvement. Tang et al. [24] analysed how to cool down the PV panel by using heat pipe, and obtained that the temperature reduction and system efficiency enhancements could reach 4.7 °C and 2.6%, respectively. Moradgholi et al. [25] utilized a set of heat pipes to decrease the surface temperature of a PV module, and demonstrated that about 13 °C of surface temperature reduction of the PV module could be obtained, leading to approximately 6% efficiency enhancement. Recently,

nanofluids are used to cool the PV cell [27]. Its pros include high thermal conductivity and heat capacity whereas its cons are entire variation in flow regime and pumping process. Karami and Rahimi [27] developed a new cooling duct with nanofluid inside that are placed at the back of a PV module to decrease the surface temperature, and found that the PV surface temperature reduction is around 4.5 °C in comparison to water cooling type's. This indicates that the nanofluid has a significant effectiveness on improving the PV electrical efficiency. Sardarabadi et al. [28] utilized copper pipes with silica particles fluid to cool a 40W PV module, and confirmed that when the concentrations of the nanofluid reaches 3.0% wt., the PV electrical efficiency could be improved by about 1.5% compared with water cooling type's.

Although these PV/T collectors can convert natural sunlight into electricity and heat, their efficiencies are still relative low owing to low thermal conductivity of their working fluids, which provides a void in achieving adequate heat exchange. Consequently, using nanofluid within the PV/T system is one of the effective approaches to enhance the efficiency of heat transfer [29, 30]. The nanofluid consists of nanoparticles with diameter from 1 to 100 nm dissolved within a fluid [31, 32]. They are divided into two phases including the base fluid in liquid state and nanoparticles in solid state [33, 34]. Some of the nanoparticles and base fluids utilized in the PV/T system are illustrated in Fig. 2.

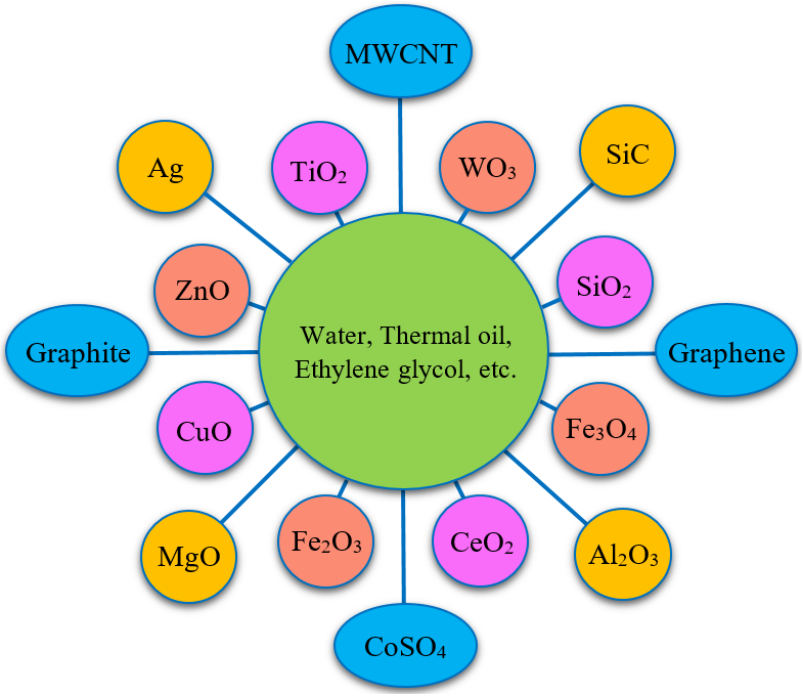

Fig. 2. Categories of normal nanopatiles and base fluids utilized in nanofluids for PV/T system [34]

Many researches reveal that the nanofluid within the PV/T system contributes to improving thermal physical properties [35, 36], mass diffusivity [37, 38] and radioactive heat transfer properties [39, 40]. Meanwhile, nanofluid volume concentration has important influence on the PV/T system performance [35, 41, 42]. Nanofluid is regarded as either a homogenous mixture of base fluid (single phase) or a heterogeneous mixture (two phase) [43]. For example, Purohit et al. [44] studied the convective heat transfer of aluminium/water nanofluid applied in a PV/T module based on the single-phase model, and demonstrated that the

enhancement of heat transfer efficiency and decrement of entropy generation could reach 25.2% and 15.2%, respectively. Sadeghi et al. [45] studied the influences of the nanocluster and its structure on the convection heat transfer coefficient of alumina nanofluids within a circular tube based on the two-phase Eulerian/Eulerian model, and demonstrated that Brownian motion has a significant effect on the heat transfer of Al_2O_3 nanofluid. Reeser et al. [46] discovered the optimal design of a two-phase concentrated photovoltaic cell (CPV) by using the R134a, and found that the two-phase cooling of the CPV could achieve higher COP and lower pumping power compared with the single-phase. Bianco et al. [47] numerically analysed heat transfer features of Al_2O_3 nanofluid by using both single phase and two-phase methods, and confirmed that the maximum difference of the mean heat transfer coefficient between single- and two-phase models is around 11%. Davarnejad et al. [48] assessed the heat transfer performance of MgO/Water nanofluid via using single- and two-phase model approaches, and concluded that the mean error from testing results for single-phase model is approximately 11% while it is around 2% for two phase model.

Currently, there is a research gap in the light of generalizing various PV/T types with loop-pipe and nanofluid for improving the PV/T electrical and thermal efficiencies. The aim of this study is to bridge this knowledge gap via supplying a systematic summary of the PV/T technology. Therefore, in this review paper, the different configurations of the PV/T absorber are clarified in Section 2, then, the nanofluids as working fluid applied in the PV/T system are generalized in Section 3, what is more, the structure and manufacturing of solar cells, micro-thermometry analysis of solar cells and recycling process of PV panels are illustrated in Section 4, furthermore, the challenges and future technological developments are investigated in Section 5, finally, the vital conclusions are shown in Section 6.

2. PV/T with loop-pipe

PV/T with loop-pipe is regarded as an attractive technology for building application. Different loop-pipe configurations, for example heat pipe, vacuum tube, roll-bond, heat exchanger, micro-channel, U-tube, triangular tube and heat mat, have been studied numerically and experimentally. They have the merits of high heat transfer capacity, great adaptability to different arrangement conditions, mechanical flexibility and low thermal resistance. Consequently, the effects of different loop-pipe configurations on the performance of PV/T system are investigated in the following section.

2.1 PV/T with heat pipe

Hu et al. [49] presented two PV/T systems including heat pipes with wire-meshed and wickless to study the effect of the heat pipe inclination angle on system thermal efficiency. Fig. 3 shows the structure and section view of the PV/T with heat pipe system. To be more specific, the base panel consists of aluminium plate with an area of 1270 mm × 780 mm and thickness of 1.16 mm. 9 heat pipes with dimension of ø24mm × 1mm × 90 mm for the condensing section and ø8mm × 1mm × 1300 mm for the evaporating section are placed at the back of the aluminium plate. There is about 80 mm gap between the two neighbouring heat pipes. This system consists of the PV/T with heat pipe, a water pump, a 120 L water tank, a solar PV controller and power sensor as exhibited in Fig. 4. Their results illustrate from Fig. 5 that the PV/T with wickless heat pipe could be utilized at latitudes

exceeding 20° while the PV/T with wire-meshed heat pipe is suggested for latitudes lower than 20°. In addition, the thermal efficiency of the PV/T system could reach the highest value when the inclination angle is at 40°.

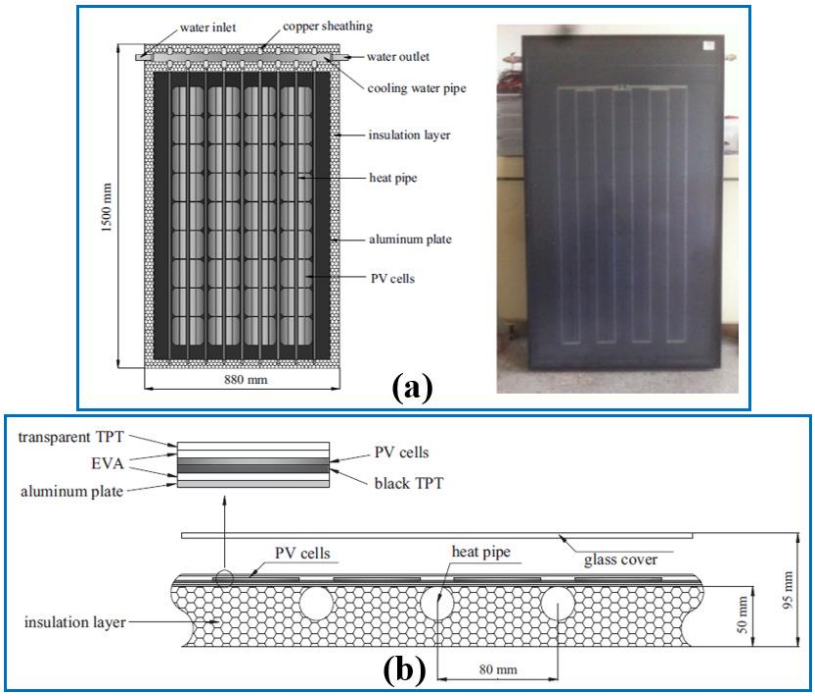

Fig. 3. Schematic diagram of: (a) PV/T heat pipe module (b) sectional view [49]

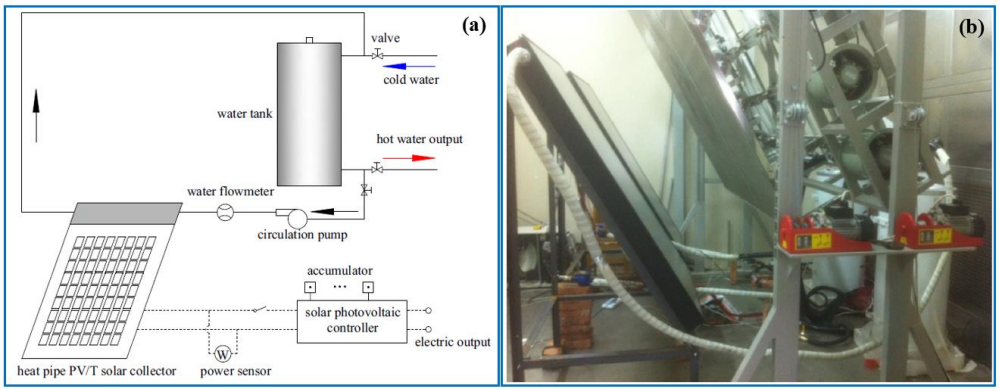

Fig. 4. Experimental setup: (a) schematic diagram; (b) photograph [49]

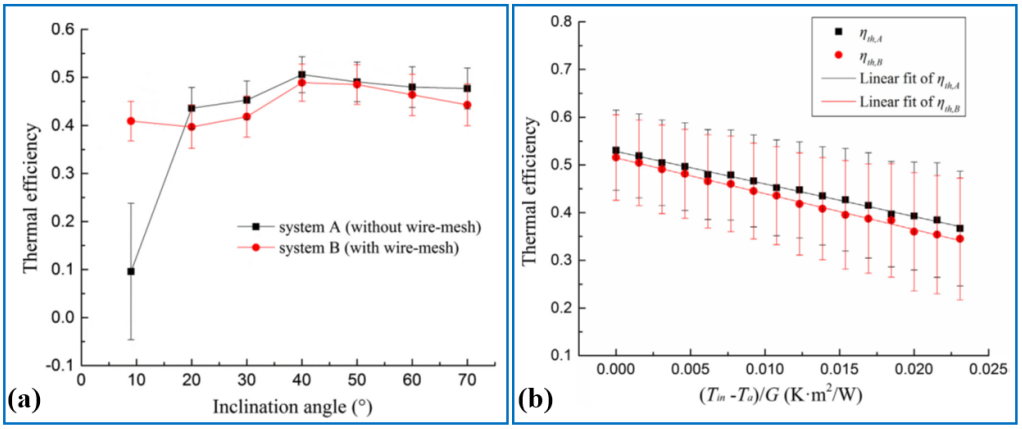

Fig. 5. Experimental results of thermal efficiency [49]

Li and Sun [50, 51] proposed a novel photovoltaic loop heat pipe/solar-assisted heat-pump (PV-LHP/SAHP) system to supply hot water for domestic building. This system integrates a PV/T, a loop heat pipe (LHP) and an air source heat pump (ASHP) as presented in Fig. 6 (a). The photograph of the system is exhibited in Fig. 6 (b). Moreover, the mathematical model of the whole system is presented in Table 1, which is on the basis of the law of energy conservation.

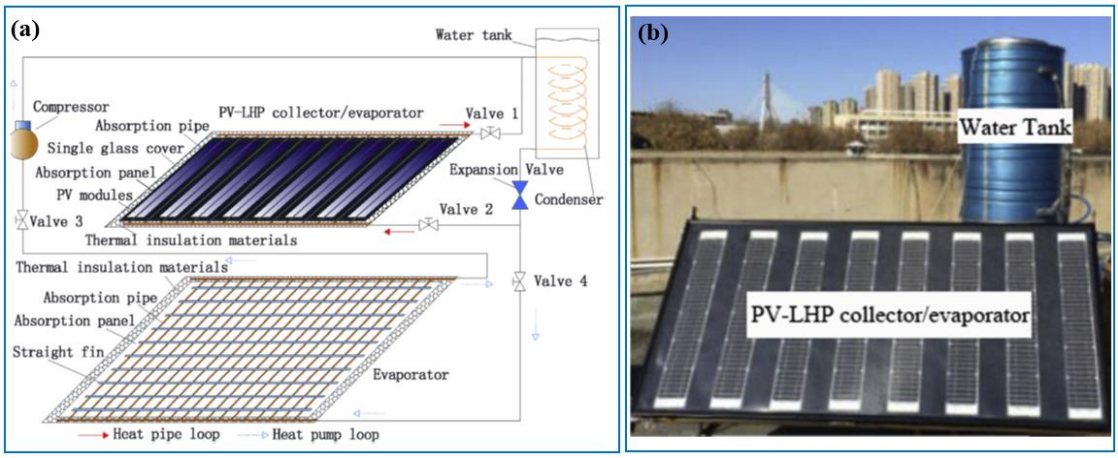

Fig. 6. PV/T-LHP system (a) schematic diagram; (b) test prototype [50, 51]

Table 1 Mathematical model of the PV/T-LHP system [50, 51]

Description	Equations
PV/T module	$\rho_c C_c l_c \frac{\partial T_c}{\partial t} = \frac{T_p - T_c}{R_{p,c}} - \frac{20A_{bi}}{A_c}\frac{T_c - T_{p,e}}{R_{c,b}} - \frac{T_c - T_a}{R_{c,a}}$ $M_{p,e}c_{p,e} l_c \frac{\partial T_{p,e}}{\partial t} = 20 \cdot A_{bi}(\frac{T_c - T_{p,e}}{R_{c,b}} - \frac{T_{p,e} - T_{p,c}}{R_{c,a}})$
The overall thermal resistance	$R_{e,c} = R_{e,p} + R_{e,wick} + R_{c,i} + R_{c,p}$ $R_{e,p} = \frac{\ln(\frac{D_{e,o}}{D_{e,i}})}{2\pi N_{hp} L_{p,e} k_{p,e}}$ $R_{e,wick} = \frac{\ln(\frac{D_{wick,o}}{D_{wick,i}})}{2\pi N_{ap} L_{p,e} k_{wick}}$ $R_{c,i} = \frac{1}{\pi D_{c,i} L_{p,c} h_{c,i}}$ $R_{c,p} = \frac{\ln(\frac{D_{c,o}}{D_{c,i}})}{2\pi L_{p,c} k_{p,c}}$
Immersed coil condenser	$M_{p,c}c_{p,c}\frac{\partial T_{p,c}}{\partial t} = \frac{T_{p,e} - T_{p,c}}{R_{e,c}} - \frac{T_{p,c} - T_w}{R_{c,w}}$
Thermal efficiency	$\eta_c(j) = \frac{Q_c(j)}{A_c I(j)}$
Overall photo-thermal efficiency	$\eta_o(j) = \eta_c(j) + \xi \cdot \eta_p(j)$

Heat pump COP	$COP_{SASHP}(j) = 10^{-3} \cdot [72.3 \cdot [T_a(j) - 273.15) - 29.5 \cdot [T_{w,in}(j) - 273.15 + 1.64 \cdot I(j)] + 2.6$ $COP_{ASHP}(j) = 10^{-2} \cdot [72.3 \cdot [T_a(j) - 273.15) - 2.95 \cdot [T_{w,in}(j) - 273.15] + 2.6$
Environmental benefits	$CR_{PV-LHP/SAHP} = (E_{nc,ASHP} - E_{nc,PV-LHP/SAHP}) f_{el,CO_2}$ $CR_{SA-ASHP} = (E_{nc,ASHP} - E_{nc,SA-ASHP}) f_{el,CO_2}$
Life cycle cost	$P = A[\frac{(1+i)^n - 1}{i(1+i)^n}]$

It is confirmed from Fig. 7 that the daily mean electrical efficiency could reach 11.59% in cooling season, 11.91% in transition season and 12.38% in heating season, and the daily mean overall thermal efficiencies of the three seasons are 53.64%, 52.63% and 47.84%, respectively. Furthermore, the monthly mean power consumption is around 0.024 kWh/L in heating season, which is almost six times of that in the other months. This is because winter climate condition has an adverse influence on the system operating and the heat pump has to operate in comparative low COP. It is notably that the monthly mean heat pump COP is approximately 3.1. Afterwards, they implemented social-economic assessment including electricity consumption, economic feasibility and CO_2 emission for the conventional ASHP and PV-LHP/SAHP systems. Compared to the traditional ASHP unit, electricity consumption and life cycle cost of the PV-LHP/SAHP system can be decreased by 79.4% and 57.3%, respectively, in the meantime, CO_2 emission can be saved 10.12 tons.

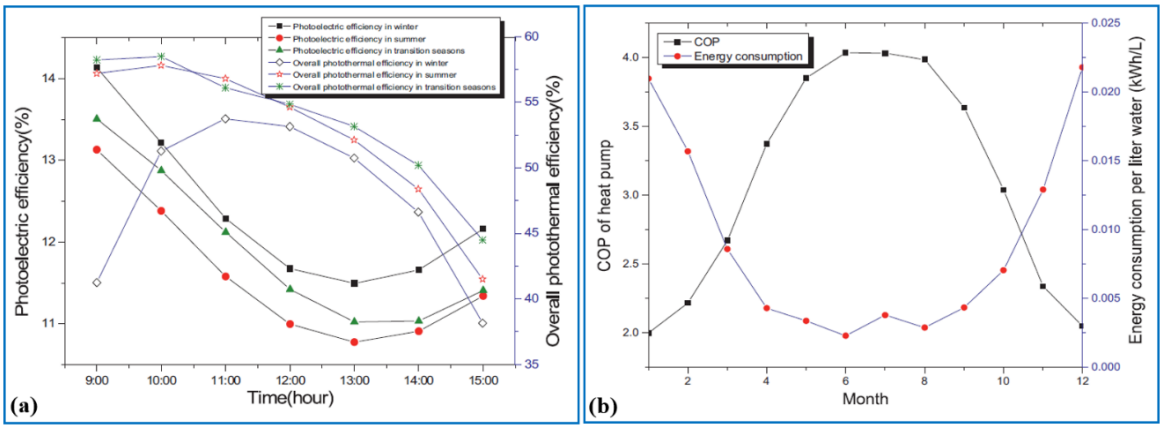

Fig. 7. Simulation results: (a) efficiency; (b) COP and power consumption [50]

Yu et al. [52] proposed an analytical model of novel PV/T-micro-channel loop heat pipe (MCLHP) based on the Newton-Raphson approach in order to explore the influence of the wick structure's fractal parameter on effective porosity. Fig. 8 depicts the whole system configuration. The collector involves 20 mini-channel heat pipes with 10 ports. The LHP system includes the condenser, evaporator mini-heat pipe channel, vapour and liquid headers, vapour and liquid transportation lines and the liquid collector. The pores distribution in porous media is non-fractal when porosity is less than 0.07 as demonstrated in Fig. 9. This indicates that a bigger pore diameter and a greater effective porosity could result in a growth of wick fractal dimension. What is more, the growth of tortuosity of capillaries, the reduction of pores portion and effective porosity contribute to improving the system performance.

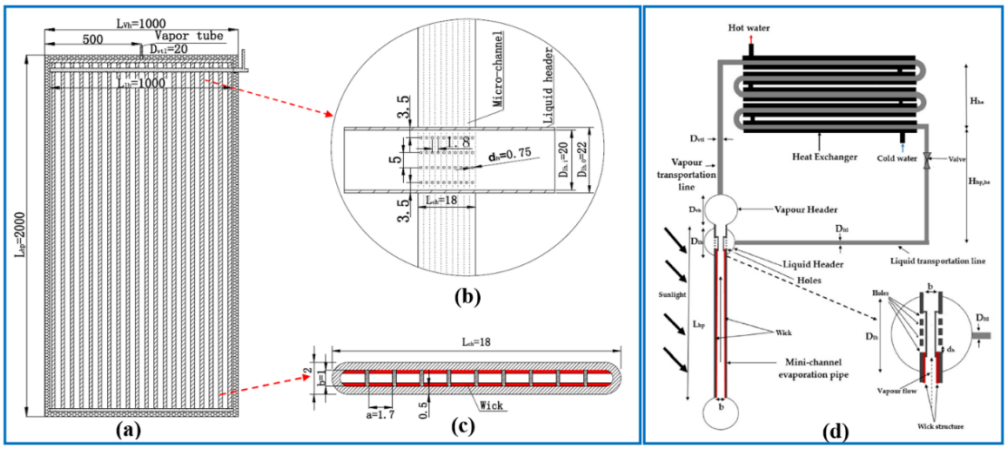

Fig. 8. The schematic of the novel PV/T-MCLHP system: (a) collector; (b) holes position; (c) top view of the mini-channel; (d) LHP with porous wick structure [52, 53]

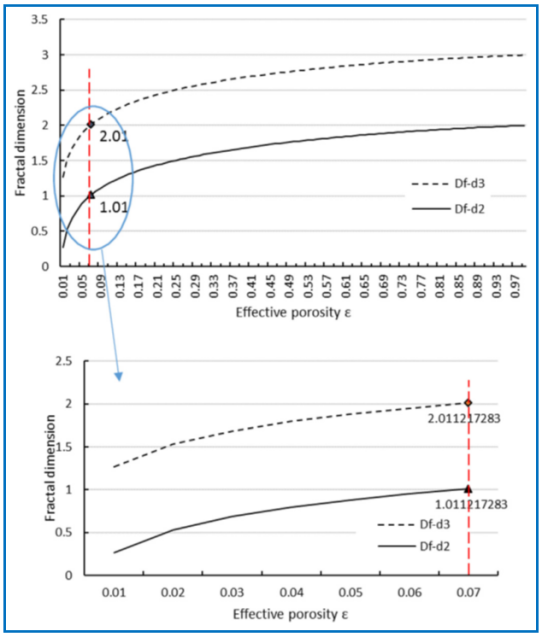

Fig. 9. The variation between fractal dimension and porosity [52]

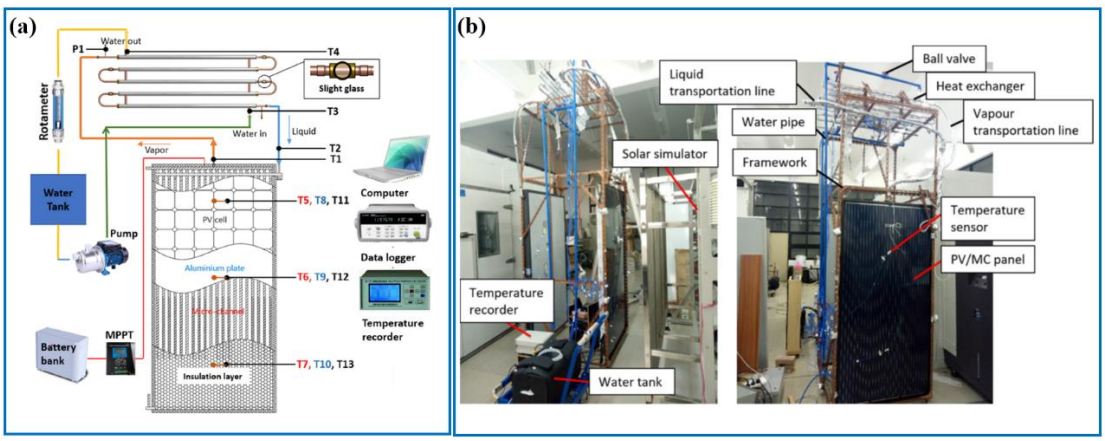

Fig. 10. Schematic of: (a) experimental setup and instrumentation; (b) field testing [54]

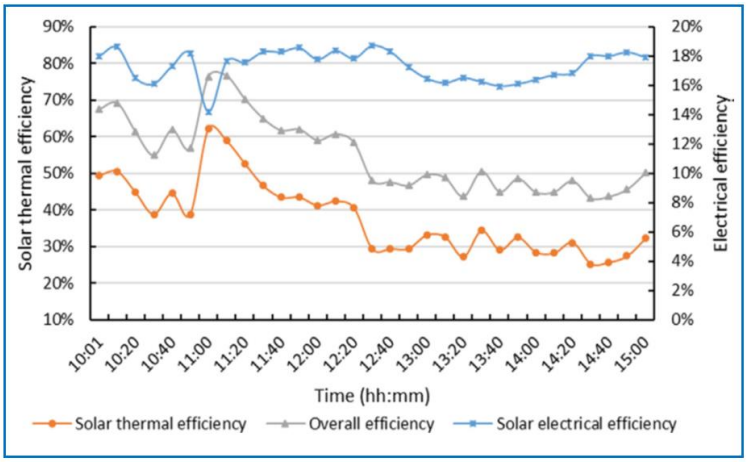

Fig. 11. System efficiency with time variation [54]

Later, they carried out an experimental investigation of the PV/T-MCLHP system to assess thermal and electrical efficiencies. Fig. 10 depicts the experimental setup and instrumentation. It is observed from Fig. 11 that the system performance indicators have relative fluctuations, which could reach the average value of 16.54%, 38.36% and 54.90% for electrical, thermal and overall efficiencies, respectively. Specifically, the solar thermal efficiency varies in the range between 25.2% and 62.2%. This is because it is impacted by the flow rate of coolant fluid, inlet temperature, weather condition and height difference between the evaporator and condenser. Meanwhile, the system electrical efficiency fluctuates ranging from 15.59% to 18.34%. Additionally, the novel system could achieve 33.31% and 17.20% higher overall solar efficiency compared to the existing BIPV/T and PV/T units respectively.

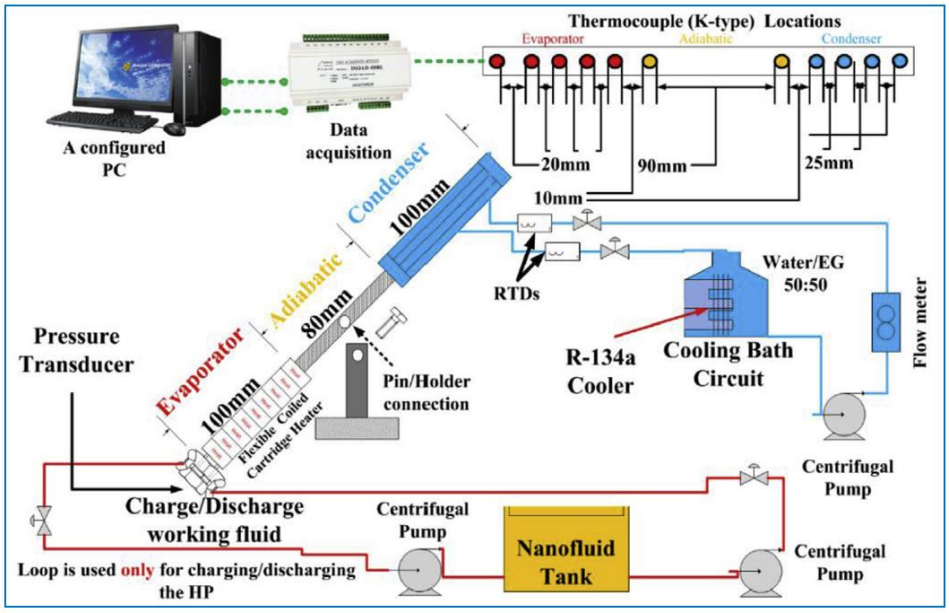

Fig. 12. Schematic diagram of experimental rig [55]

Sarafraz et al. [55] performed a test of a thermosyphon heat pipe by using the zirconia-acetone (ZrO_2-C_3H_6O) nanofluid to study the effects of tilt angle and filling ratio on the heat transfer coefficient. The thermosiphon heat pipe is constructed by using an oxygen-free copper with the internal and external diameters of 10.7 mm and 12 mm, respectively, and the axial length is 280 mm as shown in Fig. 12. Experimental results from Fig. 13 (a) show that when the filling ratio of the heat pipe varies from 10% to 60%, the heat transfer coefficient could reach a peak value of about 7500W/m^2·K, and then it begins falling when the filling ratio of the heat pipe is in the range from 70% to 90%. This means that the filling ratio is impacted by the thermal absorbency of the thermal fluid and space available inside the heat pipe. Moreover, as presented in Fig. 13 (b), the tilt angle has a significant influence on the heat transfer coefficient of heat pipe, and when the tilt angle is at 60°, the heat transfer coefficient could achieve the highest heat transfer coefficient of about 7500W/m^2·K.

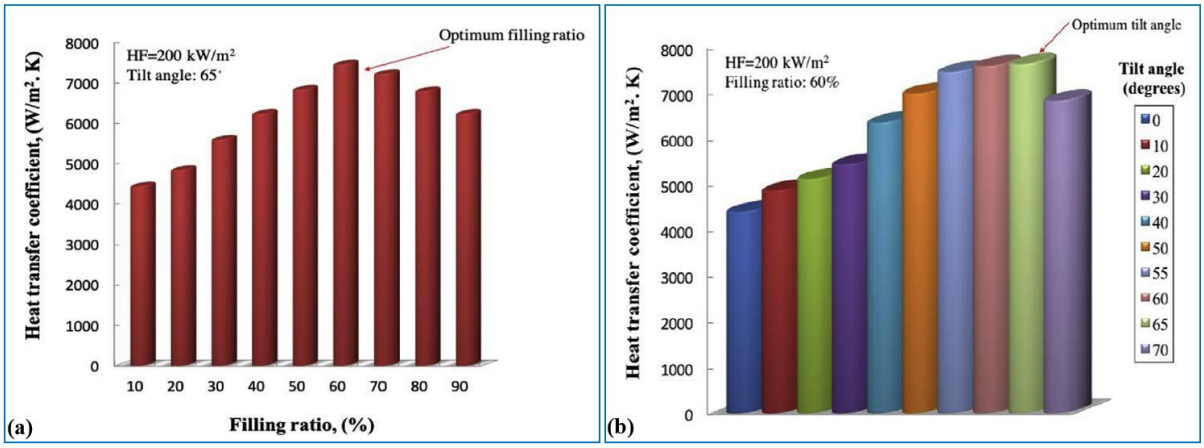

Fig. 13. Experimental results of heat transfer coefficient: (a) filling ratio; (b) title angle [55]

Sarafraz et al. [56] established a numerical model of the concentrated photovoltaic/thermal (CPV/T) to assess the system performance. The core of the system is the dual receiver involving the CPV/T module and a cavity receiver as shown in Fig. 14.

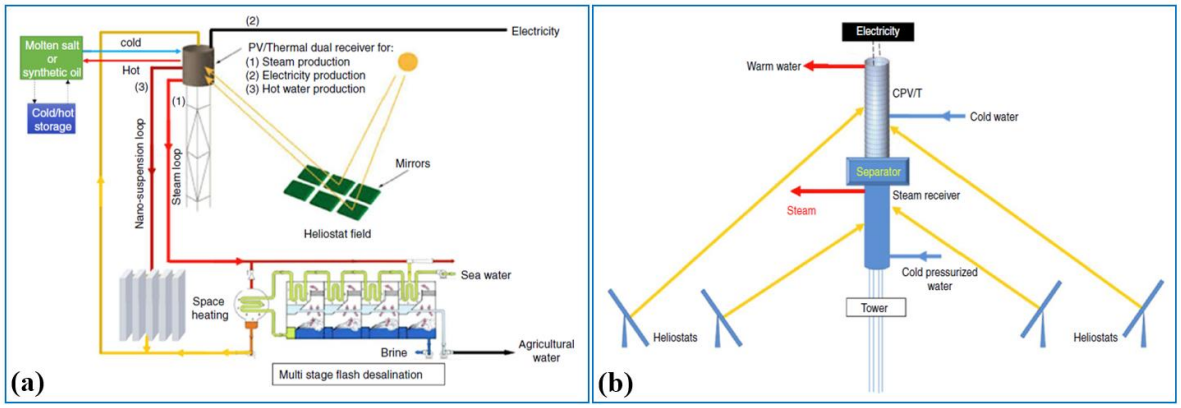

Fig. 14. Schematic diagram of: (a) CPV/T system design; (b) cavity receiver for the production of steam [56]

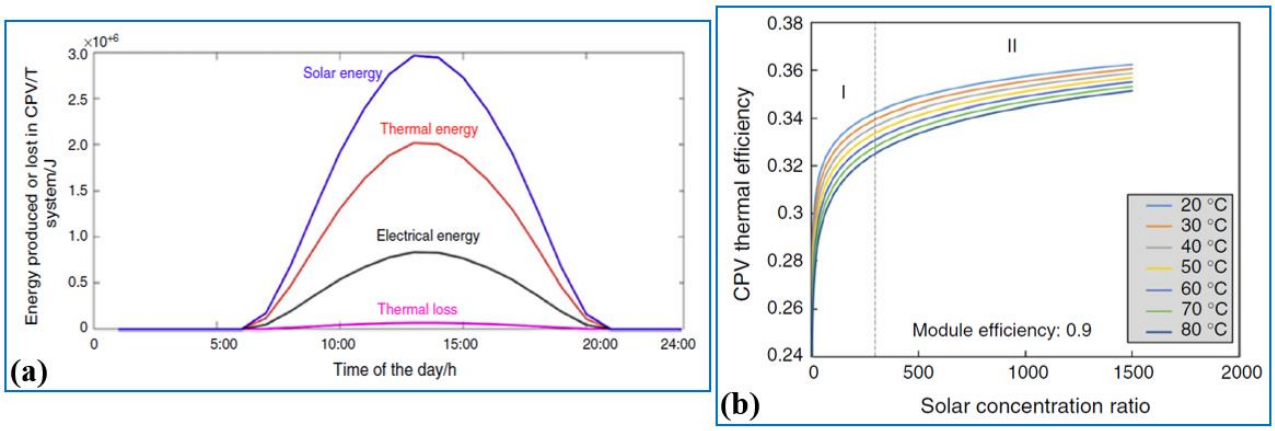

Fig. 15. Results analysis: (a) thermal and electrical energy; (b) CPV thermal efficiency [56]

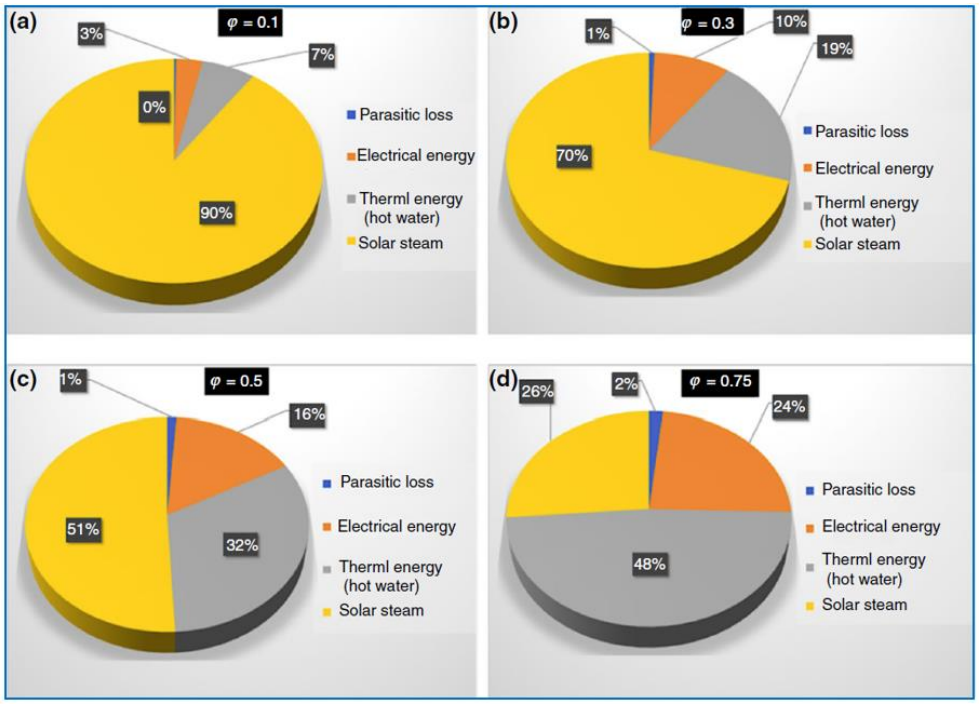

Fig. 16. Results analysis: (a) thermal and electrical energy; (b) CPV thermal efficiency [56]

Results obtained from Fig. 15 that the electrical and thermal energy could achieve 0.9 MW and 1.9 MW, respectively, meanwhile, the system thermal efficiency is improved from 0.28 to 0.36 when the solar concentration ratio increases from 10 to 1500. Additionally, it is worth noticed that the φ value plays vital influences on the system electrical, thermal and steam production as depicted in Fig. 16. Specifically, when the φ are 0.1, 0.3, 0.5 and 0.75, approximately 3%, 10%, 16% and 24%, 7%, 19%, 32% and 48% of the total solar energy are absorbed, respectively, whereas about 90%, 70%, 51% and 26% of the total solar energy could produce the steam, and the highest thermal loss could be 2% when the φ reaches 0.75.

2.2 PV/T with vacuum tube

Widyolar et al. [57] developed a hybrid PV/T collector with parabolic trough based on the Gallium Arsenide (GaAs) cell material to generate power and thermal energy simultaneously.

The collector thermal output is determined as:

$$Q_{\text{high temperature stream}} = mc_p(T_{out} - T_{in}) \quad (1)$$

where m is the mass fluid flow rate (kg/s); c_p is the heat capacity of fluid (kJ/kg·K); T_{out} is the outlet fluid temperature (°C); T_{in} is the inlet fluid temperature (°C).

The conversion efficiency is written as:

$$\eta_{GaAs} = 0.308 - 0.0008 \times T_{cell} \quad (2)$$

where T_{cell} is the cell operating temperature (°C).

The collector electrical output is given as:

$$Q_{GaAs} = \eta_{GaAs} \times G_{cell\_inc} \quad (3)$$

where G_{cell_inc} is the incoming irradiance (kW).

The equation of low temperature stream is expressed as:

$$Q_{\text{low temperature stream}} = (G_{cell\_abs} - Q_{CaAs}) - Q_{bulk\_loss} \quad (4)$$

where G_{cell_abs} is the amount of radiation obtained via the PV cells (kW); Q_{GaAs} is the power produced (kW); Q_{bulk_loss} is the bulk thermal loss (kW).

The collector energy efficiency is given as:

$$\eta_{energy} = \frac{mc_p(T_{out} - T_{in})}{G} \quad (5)$$

The total exergy efficiency is written as:

$$\eta_{exergy,\ system} = \eta_{exergy,\ high,\ temp} \cdot \eta_{Carnot} + \eta_{energy,\ low,\ temp}\eta_{Carnot} + \eta_{GaAs} \quad (6)$$

$$\eta_{Carnot} = (1 - \frac{T_{cold}}{T_{hot}}) \quad (7)$$

The novel PV/T unit is displayed in Figs. 17 (a) and (b). It mainly involves a compound parabolic concentrator (CPC), GaAs covered mini-channels and a curved involute mirror. The solar panel with junction GaAs cells is applied in the system as given in Fig. 17 (c), the micro-channels are used to connect the wings of the CPC as presented in Fig. 17 (d). The system prototype is setup and presented in Fig. 18.

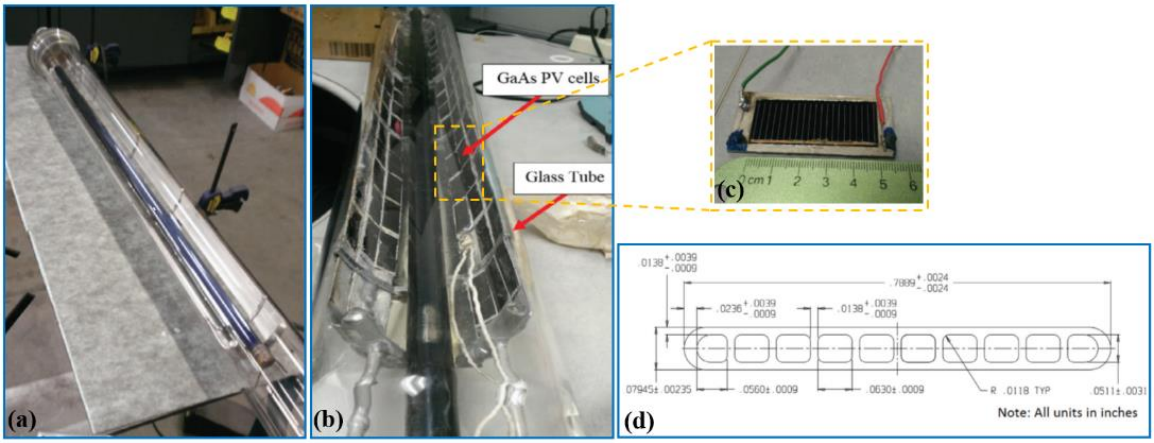

Fig. 17. PV/T with CaAs solar cell system: (a) high temperature absorber; (b) hybrid PV/T receiver; (c) GaAs solar cell; (d) micro-channel design [57, 58]

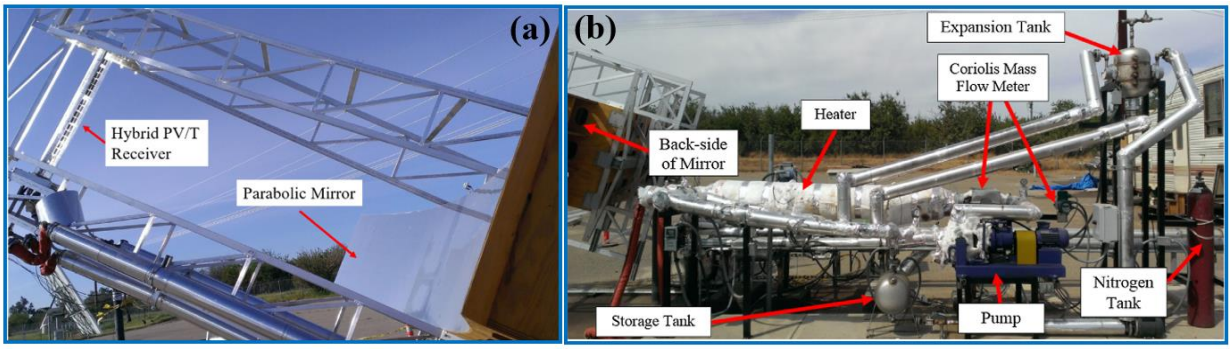

Fig. 18. System prototype during testing: (a) parabolic mirror and receiver; (b) high temperature loop setup [57, 58]

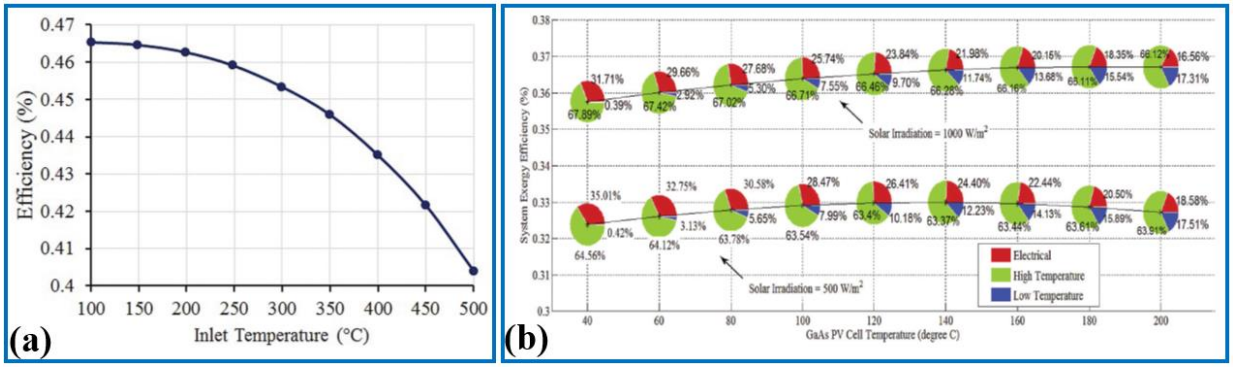

Fig. 19. Simulation results: (a) efficiency; (b) system exergy efficiency [58]

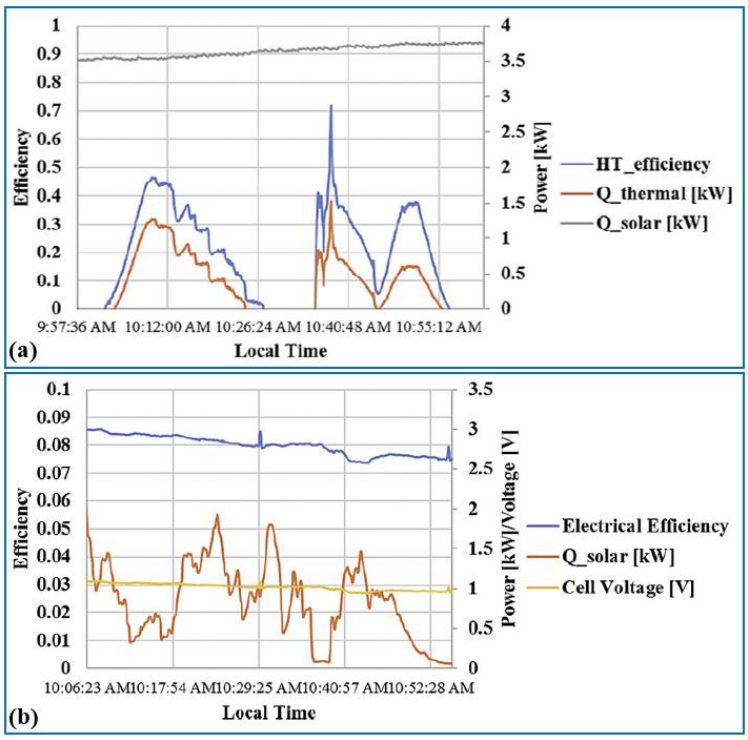

Fig. 20. Testing results: (a) thermal energy generation and efficiency; (b) electric energy generation and efficiency [57, 58]

Numerical results in Fig. 19 indicate that the system exergy efficiency is about 37% at 500 °C. Moreover, the outlet temperature achieves the maximum value of 365 °C with a thermal efficiency of about 37% as given in Fig. 20. Meanwhile, the electrical conversion efficiency is about 8%. This system is able to generate electricity directly at high temperature and has the potential to enhance the exergy efficiency of CPC greatly.

2.3 PV/T with roll-bond

Zhou et al. [59, 60] proposed a roll bond PV/T (RB-PV/T) system that is integrated with a PV module and a single-sided roll bond evaporation heat exchanger. The photo of the RB-PV/T system, layer structure and design diagram are given in Fig. 21.

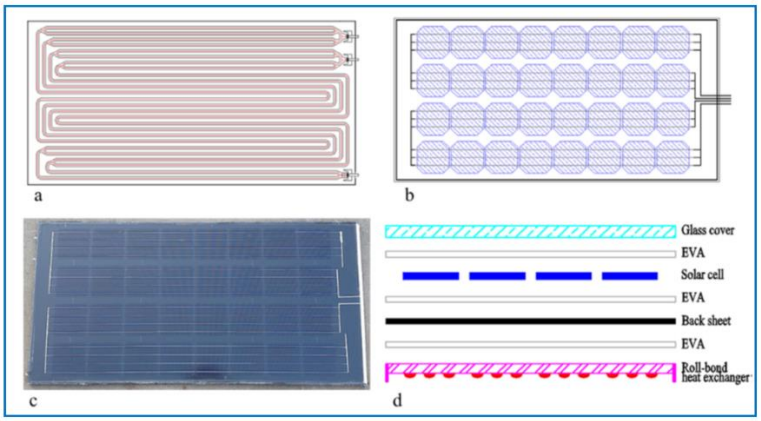

Fig. 21. RB-PV/T system: (a) working fluid path; (b) PV module; (c) prototype; (d) structure [59, 60]

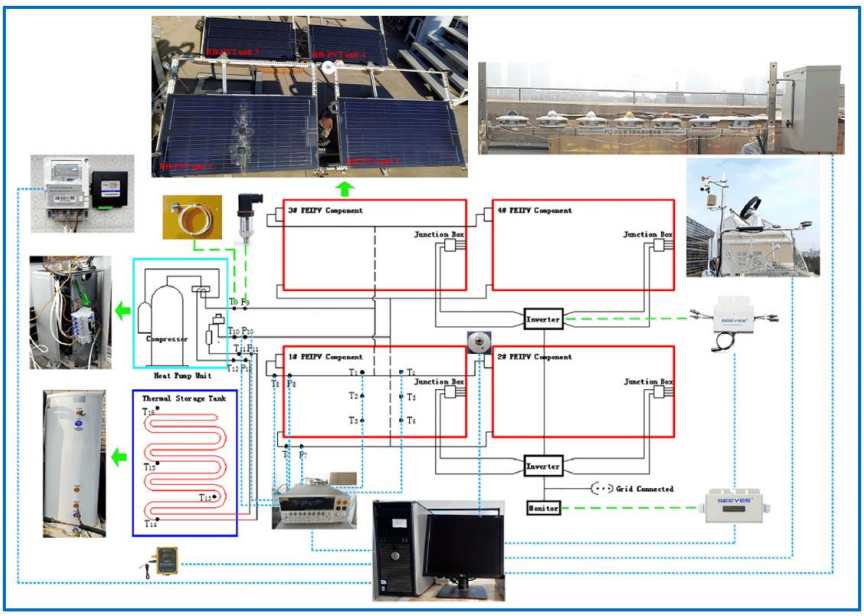

Fig. 22. Schematic diagram of RB-PV/T with heat pump system [59, 60]

According to Fig. 22, the PV/T-RB system is thought as an evaporator, then a compressor, a condenser and an electronic expansion valve, an inverter and a thermal tank are installed to achieve the grid-connected and thermal energy storage system. Results in Fig. 23 reveal that the cumulative thermal energy is 19.8 MJ and the maximum of thermal output is approximately 5.88 kW during this testing period. The maximum and mean COPs are 9.12 and 7.18, respectively. Additionally, it can be demonstrated from Fig. 24 that the mean electricity production from the PV module is approximately 250 W during the test period, and the cumulative electrical production is 2 kWh for the whole day. The mean and maximum efficiencies of the PV module are 8.7% and 17.3% individually based on the fluctuation of solar radiation intensity. This means that the RB-PV/T unit could be adopted for the large-scale practically feasible application.

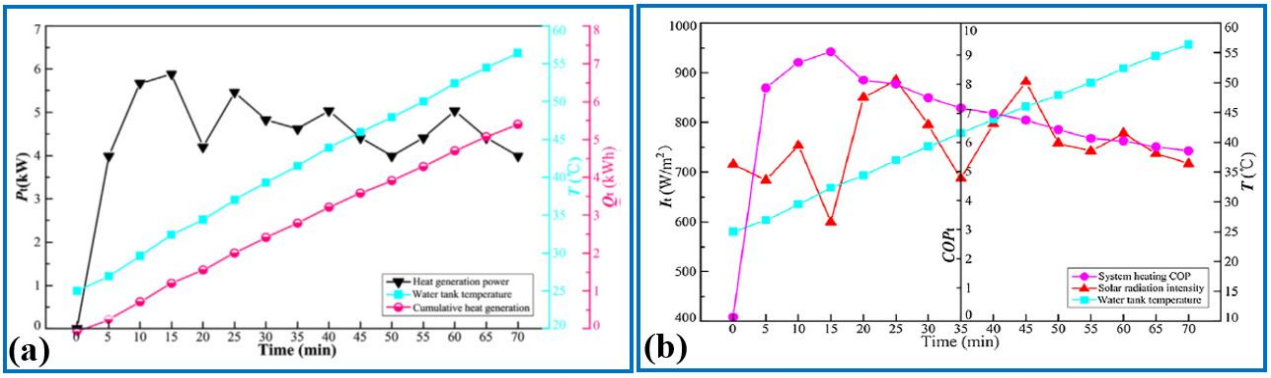

Fig. 23. System performance results: (a) thermal energy (b) system COP [59]

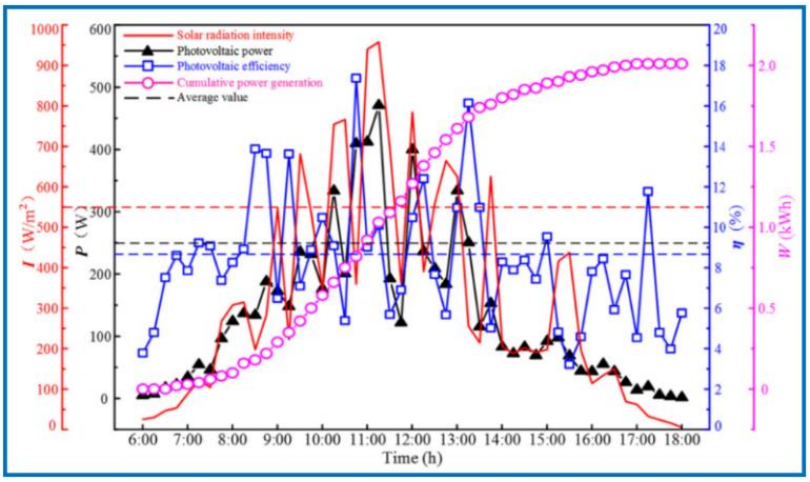

Fig. 24. System power output performance [60]

Lu et al. [61] developed a PV/T system with a heat pump based on vapor injection (VI) cycle (PV/T-VISHP) and studied the system performance in winter. The system prototype is given in Fig. 25. To be more specific, the outdoor unit of the whole PV/T-VISHP system is installed at Institute of Building Energy of Dalian University of Technology, China. 620 L water within a thermal water tank is heated by the PV/T-VISHP system with temperature rise from around 17 °C to 50 °C. According to Fig. 26 (a), the system maximum heating capacity is 8.36 kW, and the mean COP_{PVT} and heating COP_{th} of the PV/T-VISHP unit are 3.45 and 3.27, respectively. Moreover, results observe from Fig. 27 (a) that the PV/T modules' thermal output and efficiency are 6.724 kW and 49.9%, respectively. Meanwhile, the mean PV electrical output and efficiency are 1.039 kW and 7.51% individually as presented in Fig. 27 (b).

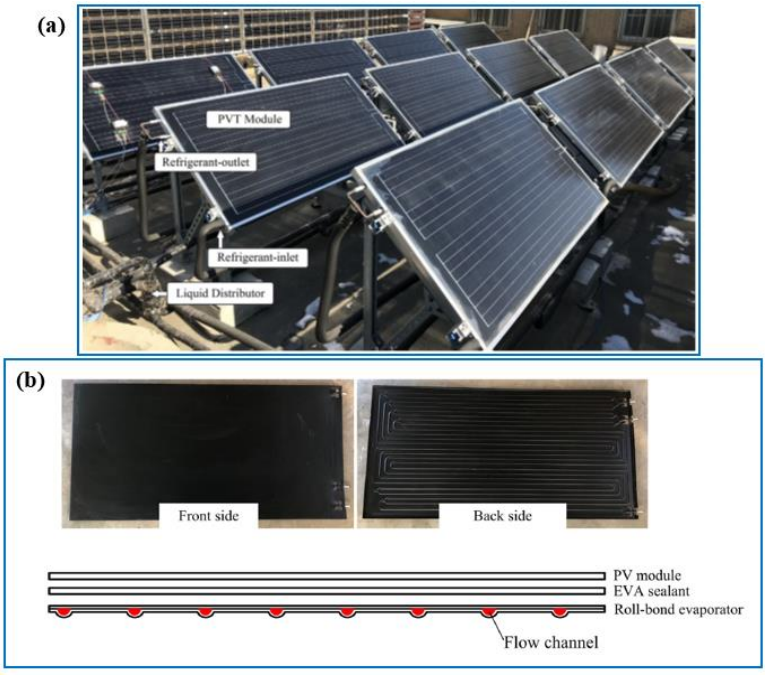

Fig. 25. Photograph of PVT-VISHP system: (a) testing prototype; (b) heat exchanger plate [61]

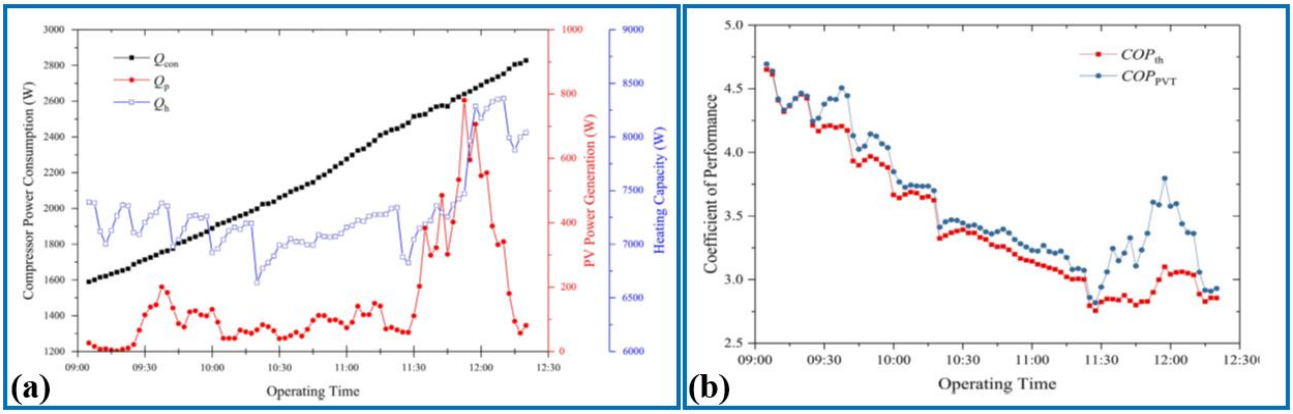

Fig. 26. Experimental results: (a) system performance; (b) system COP [61]

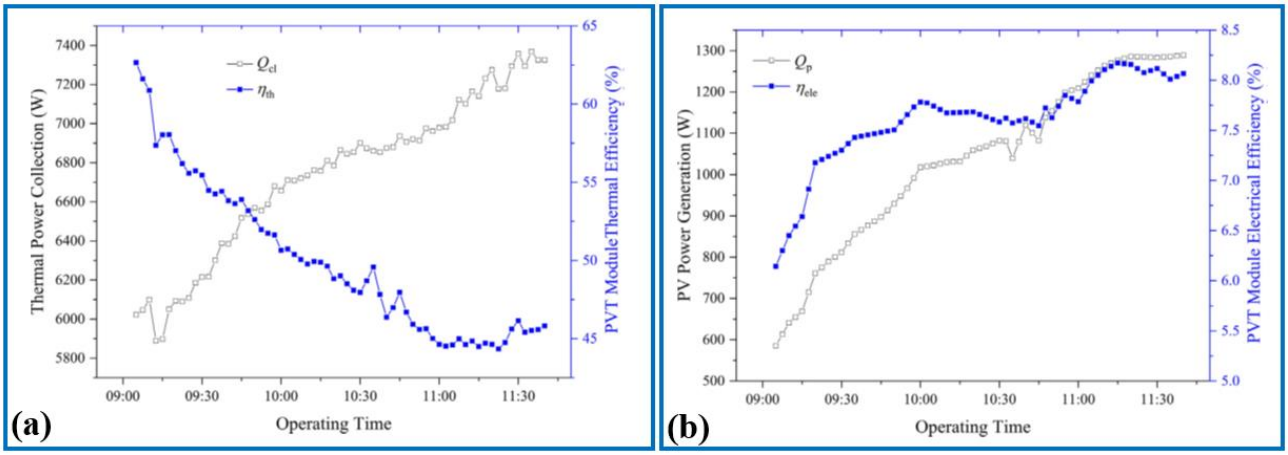

Fig. 27. Experimental results of system performance: (a) thermal; (b) electrical [61]

Fayaz et al. [62] developed a numerical model of PV/T with multi walled carbon nanotube (MWCNT) to investigate system efficiencies at the mass flow rate range of 30 litre/hour to 120 litre/hour based on the COMOSL Multiphysics. The governing equations of the PV/T with MWCNT are given in Table 2. The whole system testing equipment is shown in Fig. 28. The flow pipe has 3.5 m of length with 10 mm of diameter and is made of aluminium alloy because of low cost and high thermal conductivity as descripted in Fig. 29.

Table 2 The governing equations of PV/T with MWCNT system [62]

Description	**Equations**
PV/T system	$\rho_{nf}(u\frac{\partial u_i}{\partial x}+v\frac{\partial u_i}{\partial y}+\omega\frac{\partial u_i}{\partial z})=-\frac{\partial p}{\partial x}+\mu_{nf}(\frac{\partial^2 u_i}{\partial x^2}+\frac{\partial^2 u_i}{\partial y^2}+\frac{\partial^2 u_i}{\partial z^2})$ $(\rho C_p)_{nf}(u\frac{\partial T_{nf}}{\partial x}+v\frac{\partial T_{nf}}{\partial y}+\omega\frac{\partial T_{nf}}{\partial z})=k_{nf}(\frac{\partial^2 T_{nf}}{\partial x^2}+\frac{\partial^2 T_{nf}}{\partial y^2}+\frac{\partial^2 T_{nf}}{\partial z^2})$
PV/T received energy from module surface	$E_r=\tau_g\alpha_{sc}P_{sc}GA$
PV/T electrical energy output	$E_p=\eta_{sc}P_{sc}\tau_g\alpha_{sc}P_{sc}GA[1-\mu_{sc}(T_{sc}-T_r)]$
PV/T thermal energy output	$E_t=mC_{pnf}(T_{out}-T_{in})$

PV/T electrical-thermal-overall efficiency	$\eta_e = \frac{E_p}{E_r}, \eta_t = \frac{E_t}{E_r}, \eta_o = \frac{E_p + E_t}{E_r}$

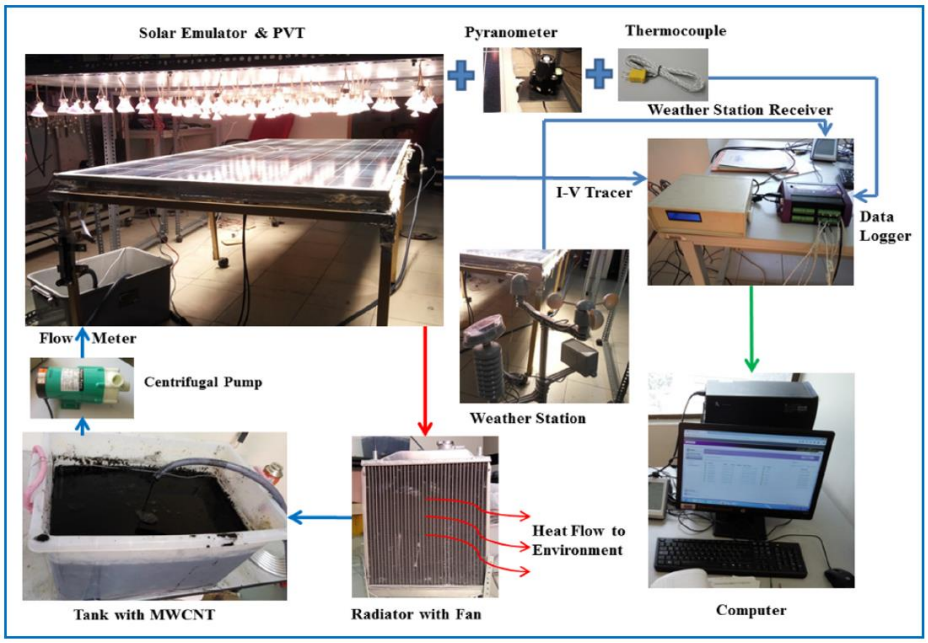

Fig. 28. Schematic of experimental rig [62, 63]

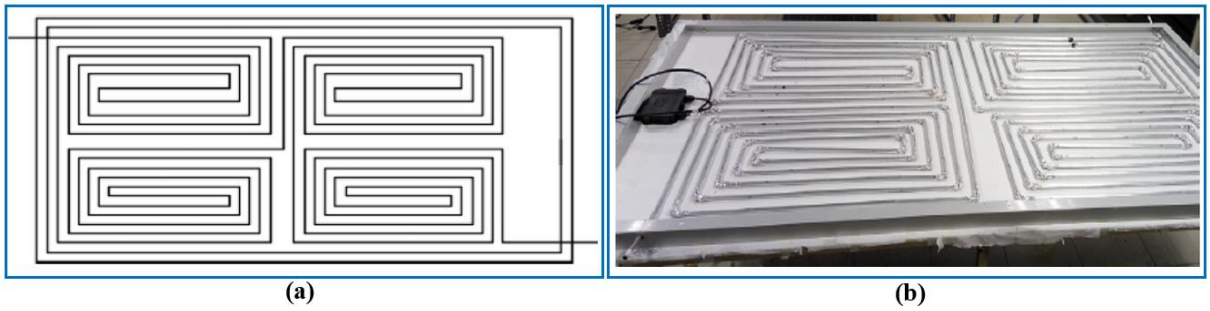

Fig. 29. MWCNT: (a) 2D model; (b) prototype [62, 63]

The electrical output and efficiency of the PV/T-MWCNT system are presented in Figs. 30 (a) and (b), it is found that the maximum electrical production in terms of numerical and experiment results are given as 187.96W and 185.93W at the flow rate of 120 litre/hour, respectively. In comparison, the least electrical outputs are 180.96 W and 179.33W individually at the flow rate of 30 litre/hour. What is more, the thermal energy raises directly with the flow rate as shown in Fig. 30 (c). The maximum thermal energy output on the basis of the numerical and testing results are 1221W and 1190W at the flow rate of 120 litre/hour, respectively, whereas the minimum value at the flow rate of 30 litre/hour is about 1152W and 1127W, respectively. According to Fig. 30 (d), the maximum numerical and experimental thermal efficiencies are 81.24% and 79.1% respectively when the nanofluid flow rate is 120 litre/hour. By comparison, the minimum values are 76.61% and 74.97% individually when the flow rate is 30 litre/hour. This indicates that more thermal energy is transferred to the working fluid at the higher flow rate. This is

because the greater temperature gradient at higher flow rate is kept, which rises the convective heat transfer between the refrigerant and pipe.

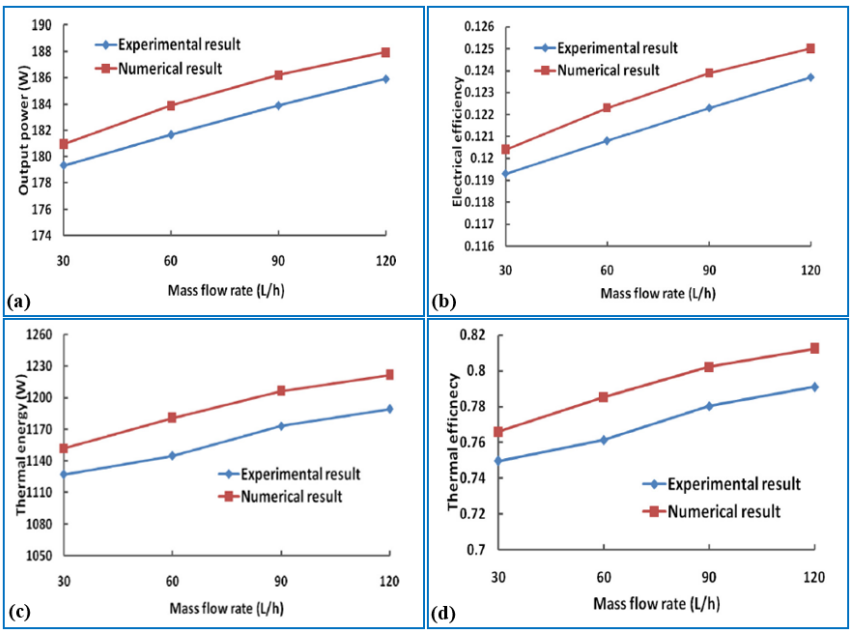

Fig. 30. Results comparison: (a) electrical output; (b) electrical efficiency; (c) thermal output; (d) thermal efficiency [62, 63]

Abdallah et al. [64] implemented an experimental work for a PV/T with multi-walls carbon nano-tubes (MWCNT) to investigate the system performance. The schematic diagram and prototype of the PV/T-MWCNT system are displayed in Fig. 31. The whole circulating system consists of a serpentine shapes pipe and a 5 L tank. Specifically, the heat collector installed on the back side of PV module has a serpentine shape coil which is made of 0.3mm thickness of copper sheet with 0.25 mm diameter tube of 4 paths. The experimental data illustrate that the MWCNT nanofluid contributes to enhancing the system performance. The system could achieve the maximum efficiency of 83.62% and the average efficiency of 61.23% as presented in Fig. 32.

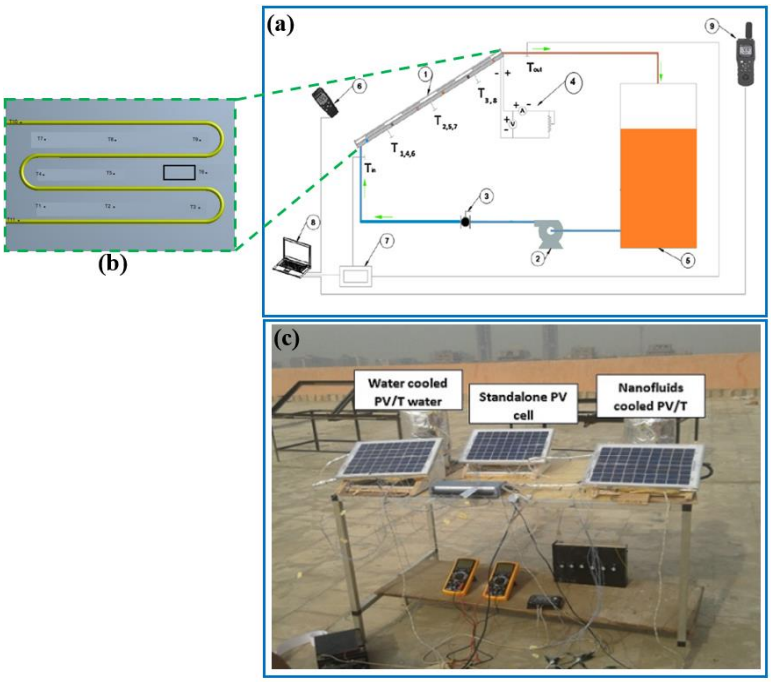

Fig. 31. (a) Schematic diagram; (b) testing prototype [64]

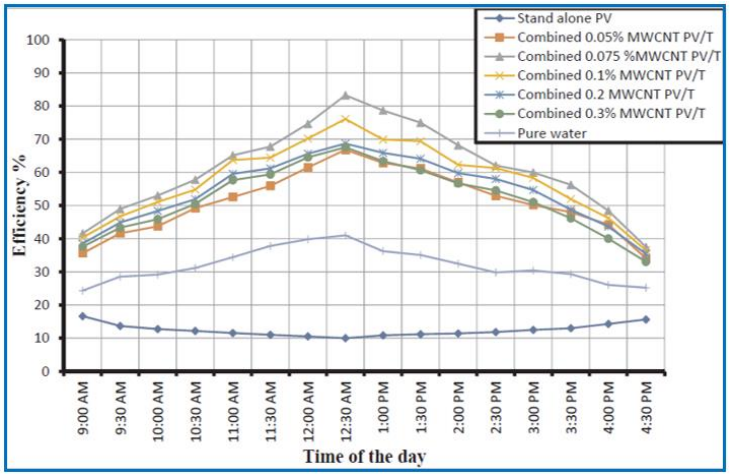

Fig. 32. System performance at different refrigerants concentrations [64]

Aste et al. [65] setup a mathematical model of PV/T with roll-bond aluminium absorber and verified via testing results, their purpose is to assess the system performance at three different locations. As shown in Fig. 33, the whole system involves a PV module, a thermal reflective insulation plate and an aluminium frame. The thermal reflective insulation plate is positioned on the back side of the absorber plate to decrease thermal loss. It is significant for the manufacturing of PVT absorbers because it is able to achieve the maximum flexibility with the low cost.

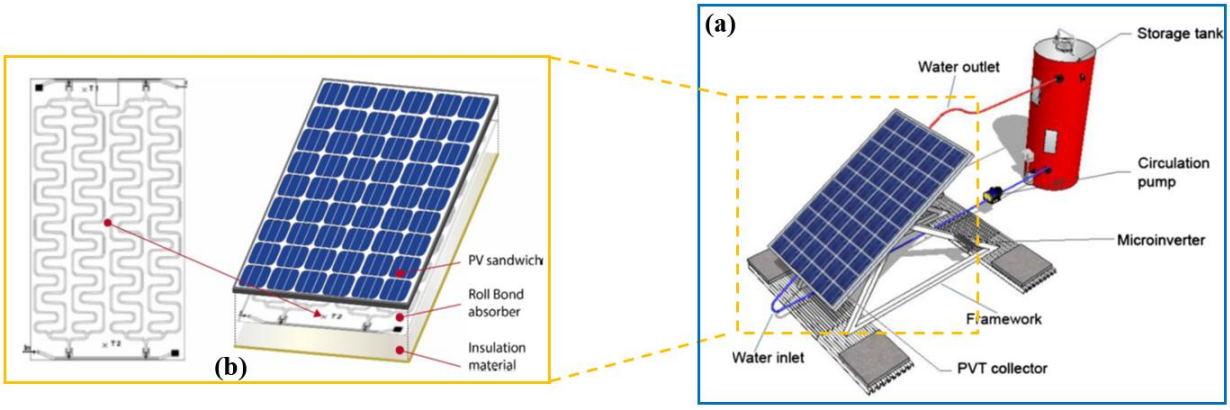

Fig. 33. Schematic diagram of: (a) PV/T with roll bond absorber system; (b) roll-bond absorber collector [65]

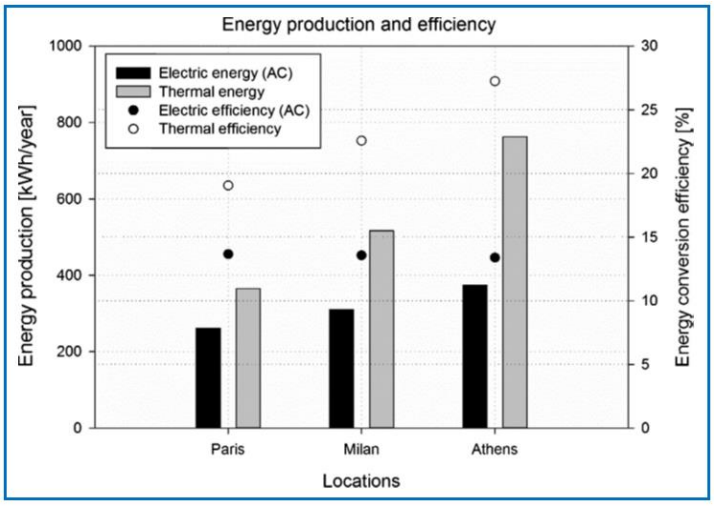

Fig. 34. Comparison of system energy and efficiency in Paris, Milan and Athens [65]

Their results in Fig. 34 reveal that the annual system thermal efficiencies are 40.6%, 36.1% and 32.7% whereas the annual system electrical efficiencies could reach 13.4%, 13.6% and 13.7% for Athens, Milan and Paris, respectively. Furthermore, the thermal efficiency increases yearly from Paris to Athens, the electrical efficiency slightly reduces because of high average module temperature.

2.4 PV/T with heat exchanger

Zhang et al. [66] investigated a novel hybrid PV/T-heat exchanger with a heat pump to supply power and heat for a domestic building in Beijing. The system is shown in Fig. 35 (a), which involves a heat-pipe-type PV/T absorber, a heat pump and a three-fluid heat exchanger. The area of the PV/T module is 1.6m^2 (1m ×1.6 m) with 95% of PV cell coverage ratio. The structure of heat pipe evaporator involves 8 vertical flat micro-channel aluminium flat tubes as presented in Fig. 35 (b). In winter, the system could collect energy from the surrounding air and solar simultaneously, meanwhile, the PV array could be cooled passively or actively through heat pipe in summer.

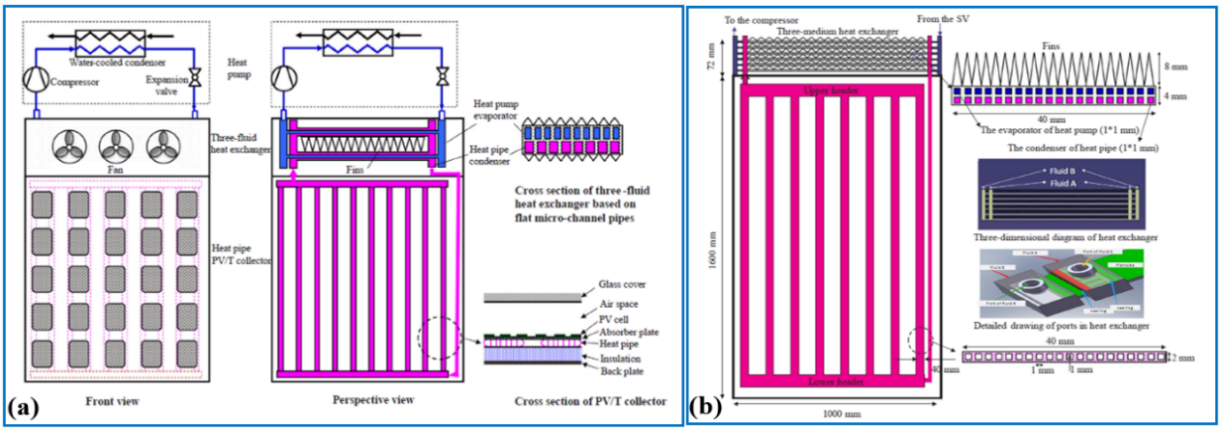

Fig. 35. Hybrid PV/T system: (a) structure; (b) standardized module [66]

Results in Fig. 36 (a) confirm that electricity consumption of the fans and compressor could be decreased by 222 kWh and 411 kWh respectively in winter, and the overall energy consumption could be reduced by 13.1% in comparison with traditional ASHP system. In the meantime, results illustrate from Fig. 36 (b) that the electrical output is improved by 712 kWh, and the PV cell temperature is reduced by 17.3 °C in the daytime.

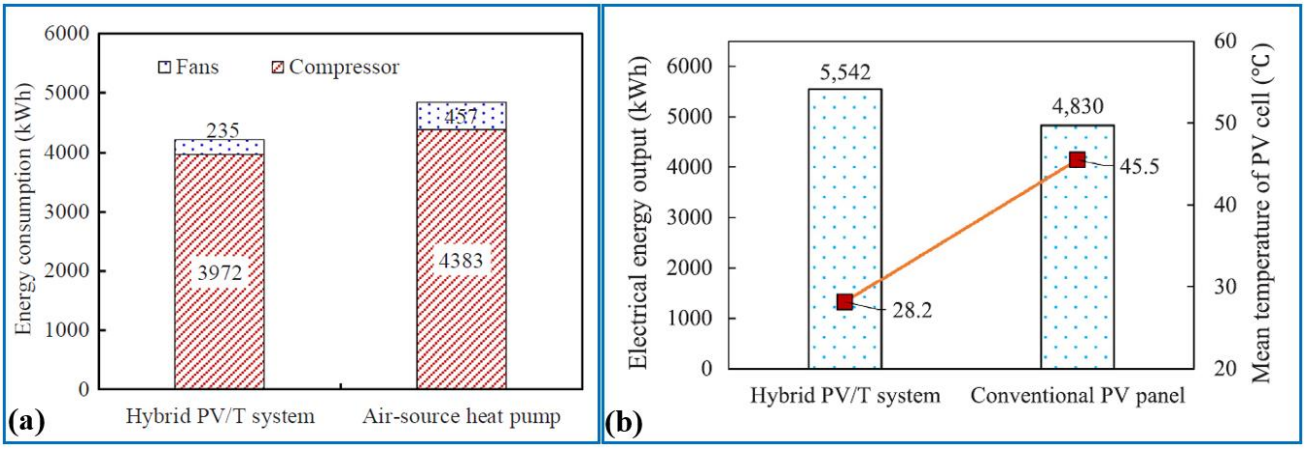

Fig. 36. Annual system performance: (a) energy consumption; (b) electrical energy output [66]

Khelifa et al. [67] implemented theoretic and testing analyses of the PV/T with heat exchanger in Ghardaia to explore the outlet fluid temperature variation and system efficiency. It can be observed from Fig. 37 that the galvanized steel heat exchanger is adhered to the back of the PV module and has a length of 130 cm with 35° inclined. The mathematical equations of the system are depicted in Table 3. Results in Fig. 38 (a) indicate that the numerical analysis are very agreement with the testing results, and the experimental outlet refrigerant temperature reaches 39 °C during the testing period. What is more, the PV/T efficiency is reduced when the solar irradiation is gradually decreased.

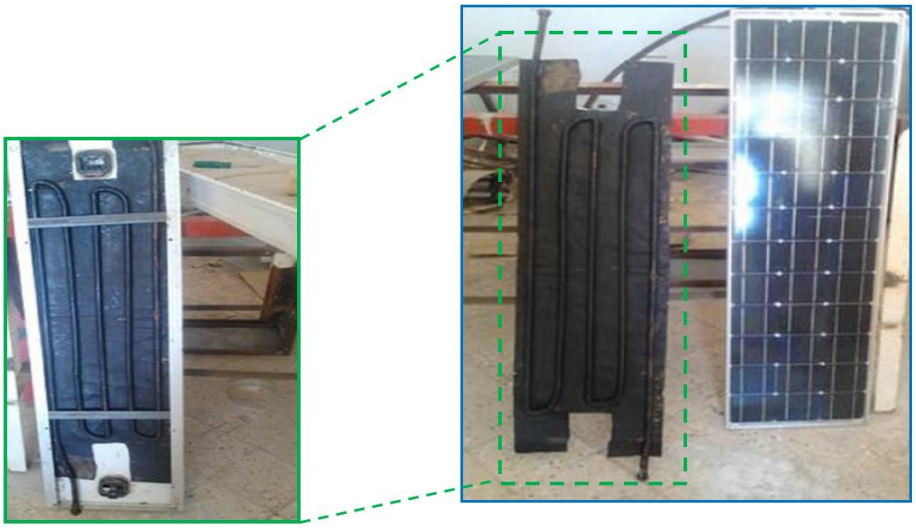

Fig. 37. PV/T with heat exchanger module [67]

Table 3 The mathematical equations of PV/T with heat exchanger of galvanized steel system [67]

Description	Equations
Glass	$T_i^{n+1} = T_i^n + \frac{\lambda_\upsilon \Delta t}{\rho_v c_v}[\frac{T_{i-1}^n - T_i^n + T_{i+1}^n}{(\Delta x)^2}] + \frac{Q_\upsilon \rho_\upsilon \cdot c_\upsilon \cdot \Delta x \Delta t}{\lambda_\upsilon}$
Cell PV	$T_i^{n+1} = T_i^n + \frac{\lambda_{PV} \Delta t}{\rho_{PV} c_{PV}}[\frac{T_{i-1}^n - T_i^n + T_{i+1}^n}{(\Delta x)^2}] + \frac{Q_{PV} \rho_{PV} \cdot c_{PV} \cdot \Delta x \Delta t}{\lambda_{PV}}$ $Q_{ele} = \tau_g A_{cel} \eta_{ref} \exp[\beta(T_{cel} - T_{ref})]$
Tedlar	$T_i^{n+1} = T_i^n + \frac{\lambda_{Ted} \Delta t}{\rho_{Ted} c_{Ted}}[\frac{T_{i-1}^n - T_i^n + T_{i+1}^n}{(\Delta x)^2}] + \frac{Q_{Ted} \rho_{Ted} \cdot c_{Ted} \cdot \Delta x \Delta t}{\lambda_{Ted}}$ $Q_{Ted} = \frac{h_{condPV-Ted}}{\rho_{Ted} \cdot c_{Ted} \cdot \frac{\Delta x}{2}}(T_{Ted} - T_{PV}) - \frac{h_{condTed-P}}{\rho_{Ted} \cdot c_{Ted} \cdot \frac{\Delta x}{2}}(T_P - T_{Ted})$
Tube	$T_i^{n+1} = T_i^n + \frac{\lambda_{tub} \Delta t}{\rho_t c_t}[\frac{T_{i-1}^n - T_i^n + T_{i+1}^n}{(\Delta x)^2}] + \frac{Q_t \rho_t \cdot c_t \cdot \Delta x \Delta t}{\lambda_{tub}}$ $Q_t = \frac{h_{condp-tub}}{\rho_t \cdot c_t \cdot \frac{\Delta x}{2}}(T_{tub} - T_p) - \frac{h_{convtub-f}}{\rho_t \cdot c_t \cdot \frac{\Delta x}{2}}(T_f - T_{tub}) - \frac{h_{condtub-iso}}{\rho_t \cdot c_t \cdot \frac{\Delta x}{2}}(T_{iso} - T_{tub})$
Fluid	$\frac{m_f c_f}{S}\frac{dT_f}{dt} + \frac{mc_f}{l}\frac{dT_f}{dy} = h_{convf}(T_{tub} - T_f)$
Useful heat gain	$Q_{use} = A_c F_R (\tau\alpha)_{PV} G$ $Q_{use} = -A_c F_R U_{pv-a}(T_{in} - T_a)$
PV/T efficiency	$Q_{use} = F_R[(\tau\alpha) - U_L \frac{T_s - T_{amb}}{G}]$

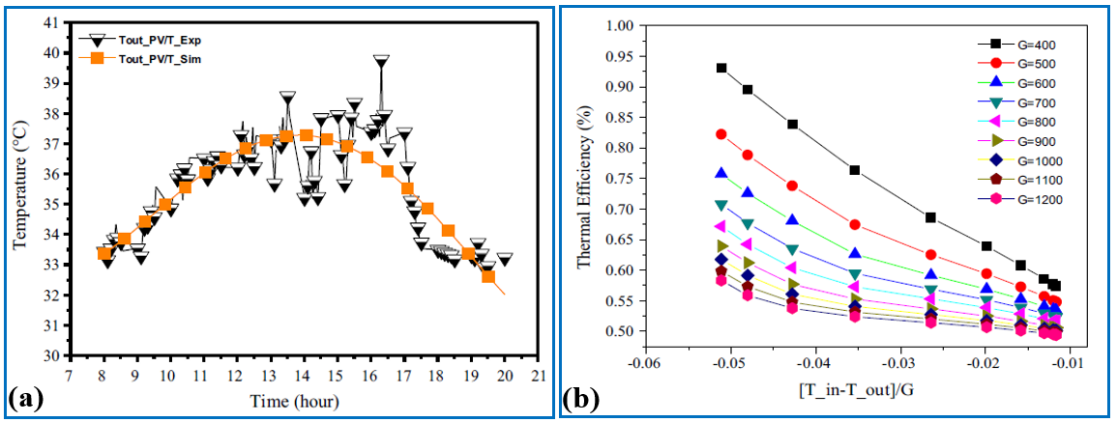

Fig. 38. Results analysis: (a) outlet temperature; (b) thermal efficiency [67]

2.5 PV/T with micro-channel

Zhou et al. [68] developed a PV/micro-channel module with a heat pump, and carried out the field testing as presented in Figs. 39 and 40. This system comprises of 11 PV/T modules, a 5P condenser that is regarded as the heat exchanger to transfer the heat from the refrigerant to the working fluid, a brushless motor to drive a compressor, and an electro-magnetic expansion valve (2-19.3 kW). Moreover, several supplementary components, such as PV controller, inverter, batteries and a storage tank are adopted in the system.

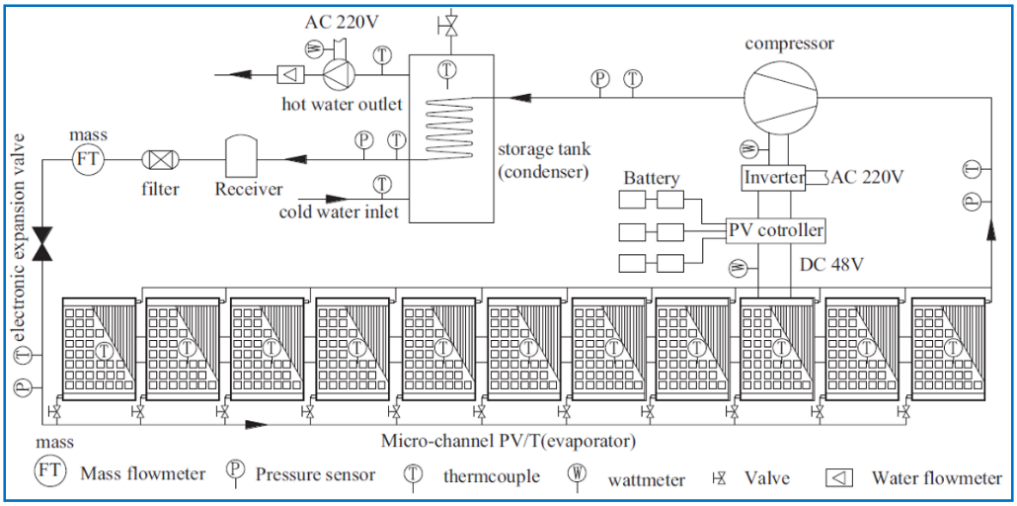

Fig. 39. Schematic diagram of the PV/T with micro-channel heat pump system [68, 69]

Fig. 40. Photos of the experimental rigs [68, 69]

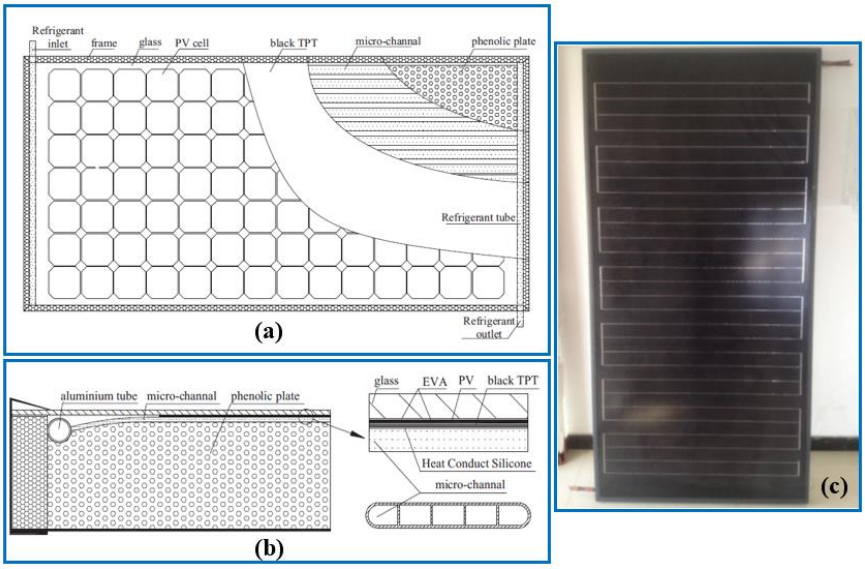

Fig. 41. Schematic diagram of PV/T module structure: (a) vertical view (b) sectional view; (c) prototype [68, 69]

Fig. 41 presents the structure of a PV/T module which involves glazing cover, PV layer, Tedlar-Polyester-Tellar (TPT), micro channel layer, air vents, insulation layer and holding-up framework. In order to assess the system performance, the mean power efficiency is given as:

$$\eta_e = \frac{\sum_{j=1}^{11} P_{PVj}}{\sum_{j=1}^{11} (G \cdot A_{PV})_j} \tag{8}$$

where η_e is the electrical efficiency (%); p is the power generation (W); G is the solar radiation (W/m^2); A is the area of PV module (m^2).

The mean thermal efficiency of the PV/T modules is shown as:

$$\eta_t = \frac{M_R (h_o - h_i)}{\sum_{j=1}^{11} (G \cdot A_{PVT})_j} \tag{9}$$

where M is the mass flow rate of refrigerant (g/s); h is the enthalpy of refrigerant (J/g);

The overall energy efficiency of the PV/T module is written as:

$$\eta_{overall} = \varepsilon \eta_e + \eta_t \tag{10}$$

where ε is the PV cell conversion factor;

$$\varepsilon = \frac{A_{PV}}{A_{PVT}} \tag{11}$$

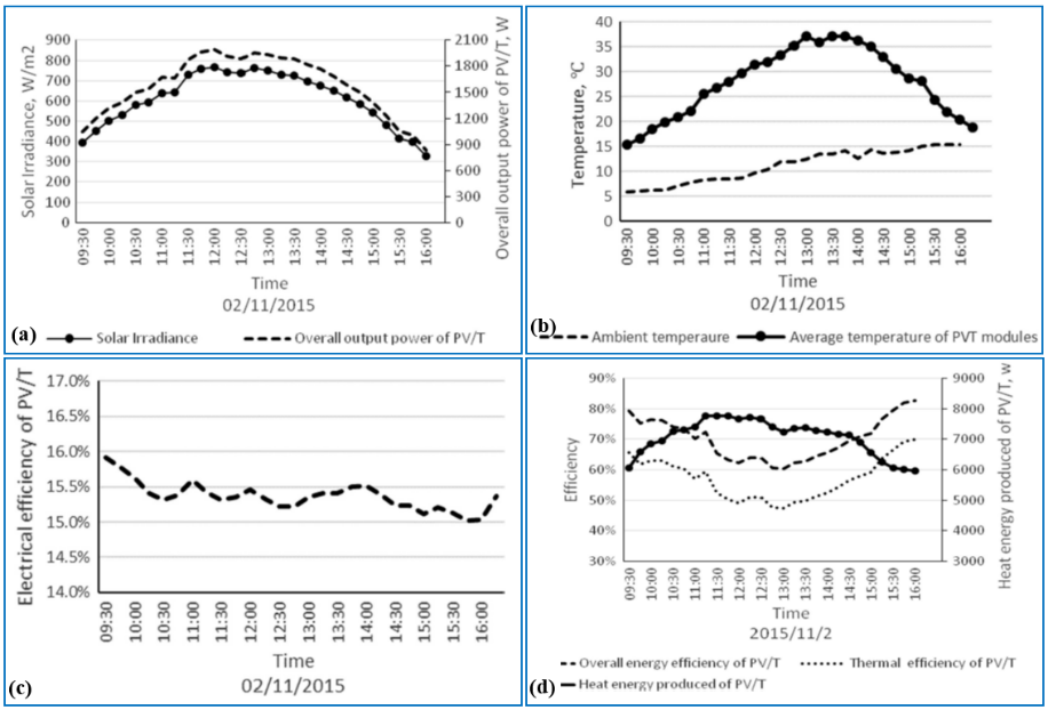

Fig. 42. Experimental results of PV/T module: (a) power output; (b) mean temperature; (c) electricity efficiency; (d) thermal energy output, thermal and overall efficiencies [68, 69]

Experimental results demonstrate from Fig. 42 (a) that electrical production of the PV/T module raises from 1050 W to 2000 W when the solar radiation level increases from 390 W/m^2 to 760 W/m^2 in the morning whereas the PV/T module's electricity output decreases from 2000 W to 900 W when the solar radiation level reduces from 760 W/m^2 to 300 W/m^2 in the afternoon. The means that the electricity production is in positive proportion to the solar radiation level. According to Fig. 42 (b), the ambient temperature increases continuously from 5 °C at 9:30 to 15 °C at 16:00, in comparison, the surface temperature of the module could improve from 15 °C at 9:30 to 36 °C at 13:30 and decreases from 36 °C at 13:30 to 18 °C at 16:00. This means that the module surface temperature is less influenced through the air temperature as well as instead, it is significantly affected

via the solar radiation. Moreover, results from Fig. 42 (c) confirm that the electrical efficiency is higher at the beginning, then becomes steady with the mean value of 15.4%. This shows that the electrical efficiency is less impacted via the environmental factors whereas it is principally determined by its construction and material. Finally, the mean PV/T thermal energy output is about 6.99 kW for the testing period as illustrated in Fig. 42 (d) [68, 69].

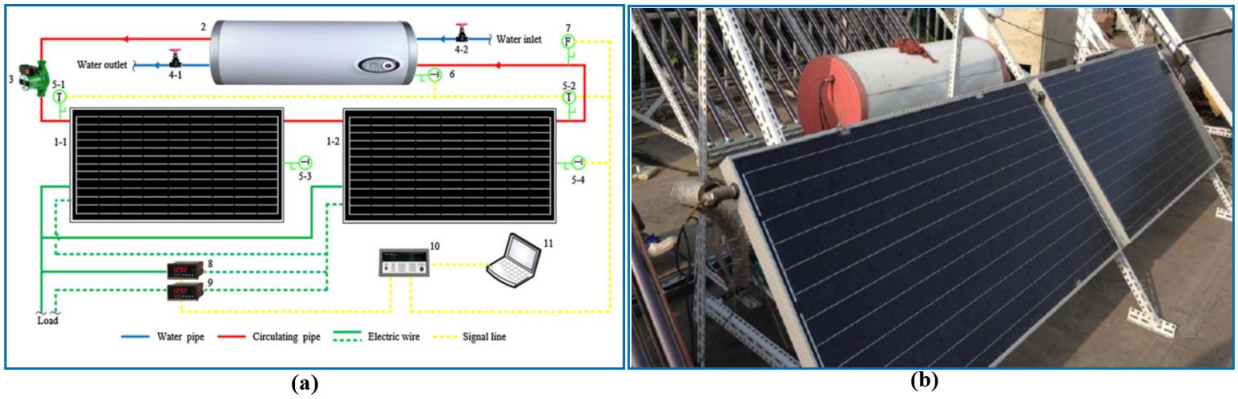

Fig. 43. Experimental rig: (a) schematic diagram; (b) test prototype [70]

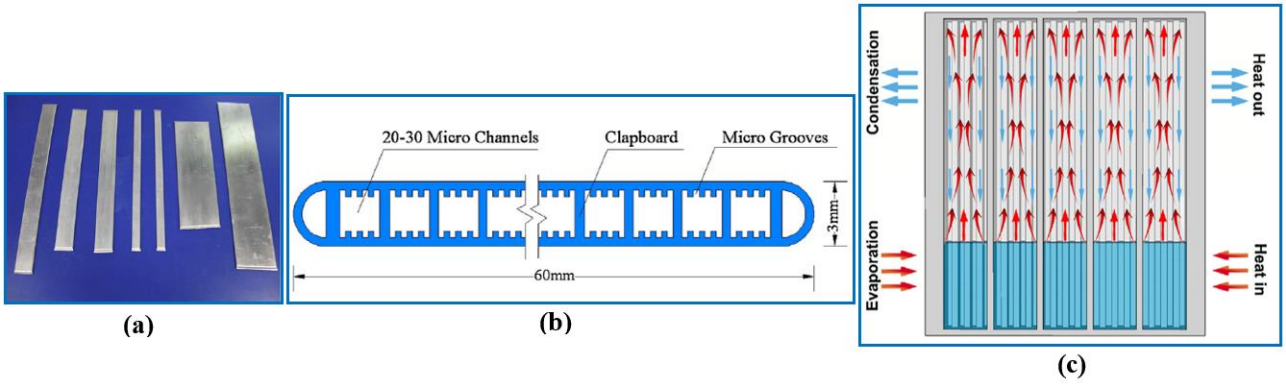

Fig. 44. Schematic diagram of MHPA [70]

Table 4 The merits of the MHPA [70]

Merits	Description
High heat transfer capability	Micro grooves can improve the region of heat exchange, thereby, the heat transfer capability is able to be strengthened dramatically.
Strong confined ability	The clapboards within the micro-channel play an important reinforcement influence and significantly enhance the confinement ability of MHPA.
Good reliability	One damaged micro-channel does not affect other micro-channel operating as they are all operating independently.
Small contact thermal resistance	This structure could conquer the demerits of cylindrical heat pipe and significantly decreases thermal resistance among the interface.
Low cost	One-time extrusion aluminium material is applied in the MHPA, and its price is more cost-effective compared to copper pipes.

Hou et al. [70] implemented an experimental analysis of PV/T with micro heat pipe array (MHPA) to investigate its performance. The system includes two PV/T-MHPA in series, a water pump and a water tank as depicted in Fig. 43. The photograph and cross-section view of the MHPA are presented in Fig. 44. It can be observed that phase change medium changes its phase from liquid

to gas in the evaporation section when heat is provided. Afterwards, the gas state medium is delivered to the condensation section and changes its phase from gas to liquid. At the end, the liquid medium returns to the evaporation section along the heat pipe wall forming the inner heat circulation. Compared with conventional heat pipe, the merit of the MHPA is illustrated in Table 4. Results reveal from Fig. 45 that the system thermal efficiency could achieve up to 40% during the cooling season and goes down to less than 20% during the heating season, so it is primarily influenced by seasonal temperature. When the temperature of water tank is equivalent to the mean air temperature, about 30% of thermal efficiency is achieved. Nevertheless, the electrical efficiency is comparatively steady at about 13% in comparison to the thermal efficiency. Additionally, the overall system efficiency varies from 30% to 50% for the whole year.

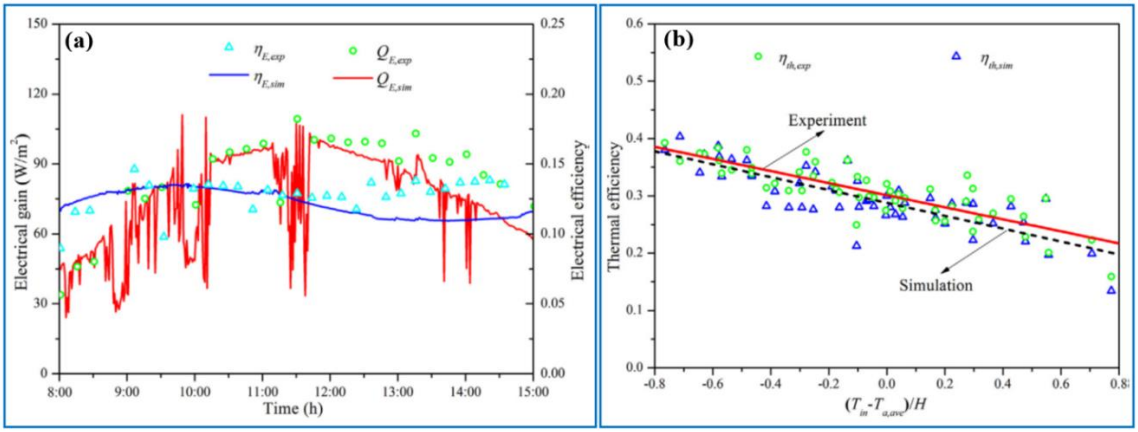

Fig. 45. Results analysis: (a) electrical gain and efficiency; (b) thermal efficiency [70]

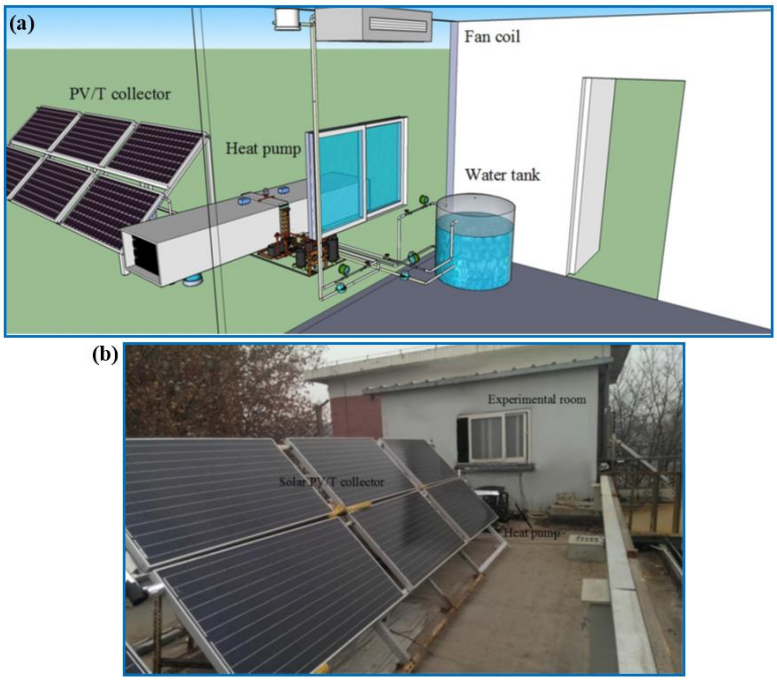

Fig. 46. PVT with MHPA system: (a) schematic diagram; (b) test prototype [71]

Wang et al. [71] setup a multi-function solar PV/T with a heat pump to provide thermal and electrical energy for a domestic building. The experimental setup of the multi-function system is displayed in Fig. 46. The PV/T module is installed with a tilted

angle of 45°. The areas of the PV module and micro-channel array are 1.125 m^2 and 1.28 m^2, respectively, and six PV/T modules with 195 W peak power are applied in this study. As shown in Fig. 47, the flat micro-channel pipe array comprises of plentiful independent microgrooves within the channel to enhance heat transfer rate. This contributes to decreasing the contact thermal resistance. The results from Fig. 48 indicate that the mean thermal efficiencies of the PV/T-W&ASHP and PV/T-WSHP could reach 36.45% and 37.5% and average COPs of 3.18 and 2.53, respectively. Furthermore, in heating mode, the COPs of the PV/T-W&ASHP and PV/T-WSHP are 2.53 and 3.18 individually, which are much higher than the ASHP system COP (2.23).

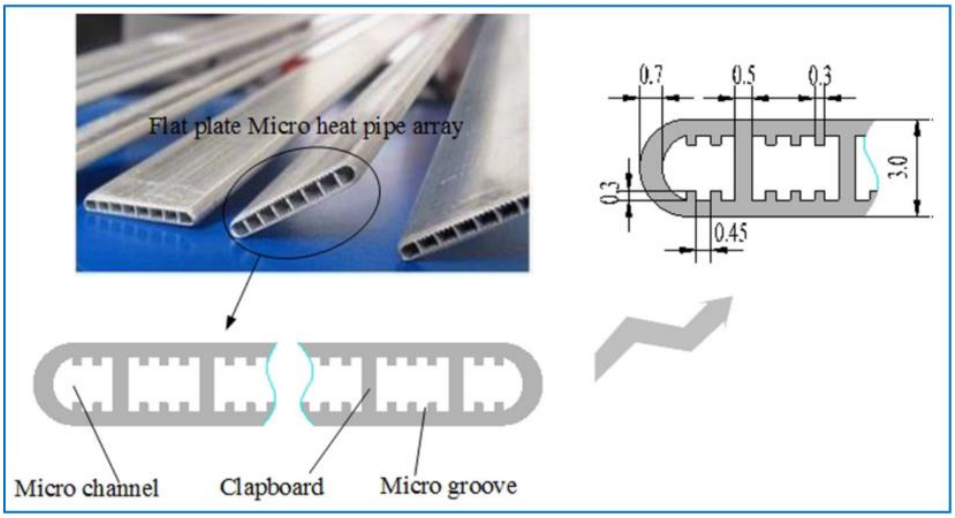

Fig. 47. Structure of micro-channel pipe [71]

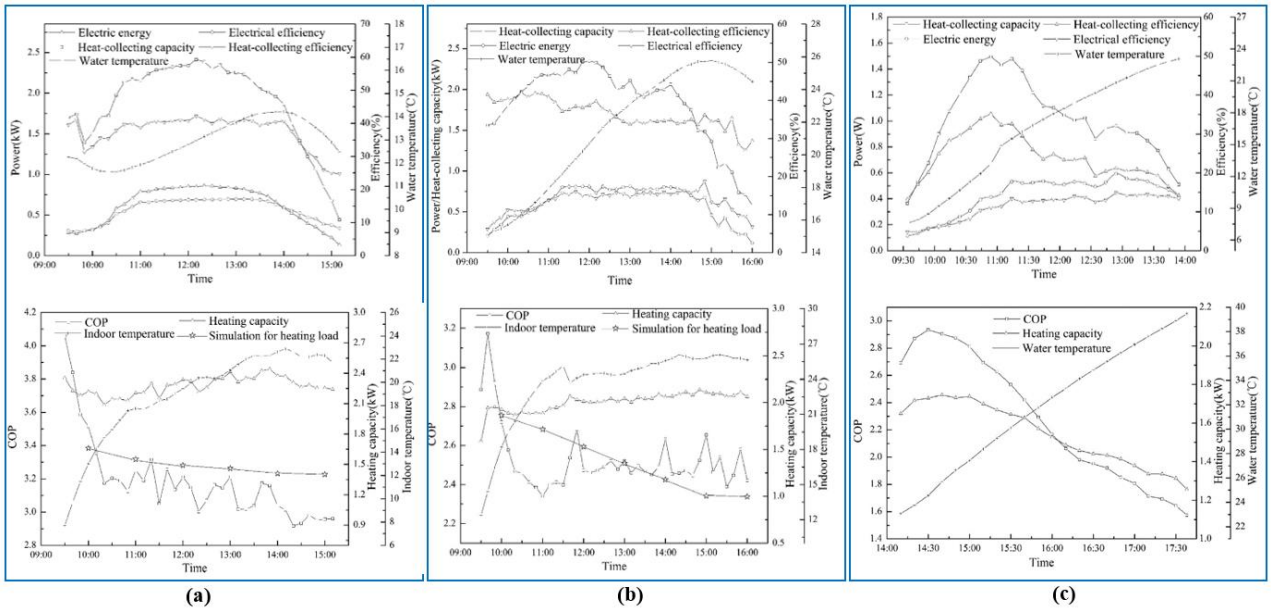

Fig. 48. Comparison of different systems performance analysis: (a) PV/T-WSHP; (b) PV/T-W&ASHP; (b) PV/T-ASHP [71]

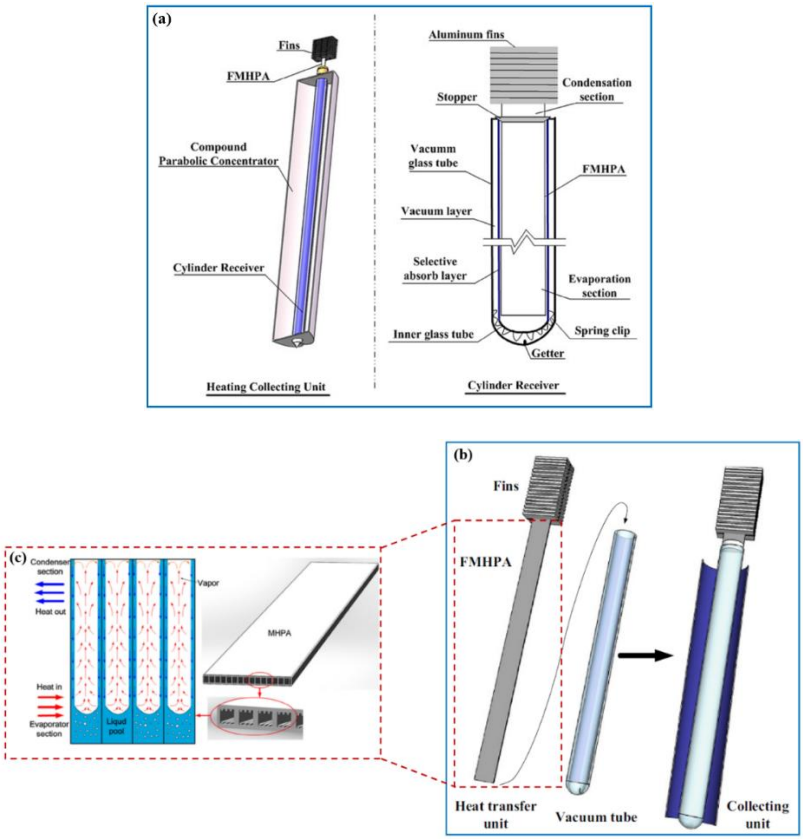

Fig. 49. Schematic diagram of the CPC system: (a) cylinder receiver; (b) structure; (c) FMHPA [72]

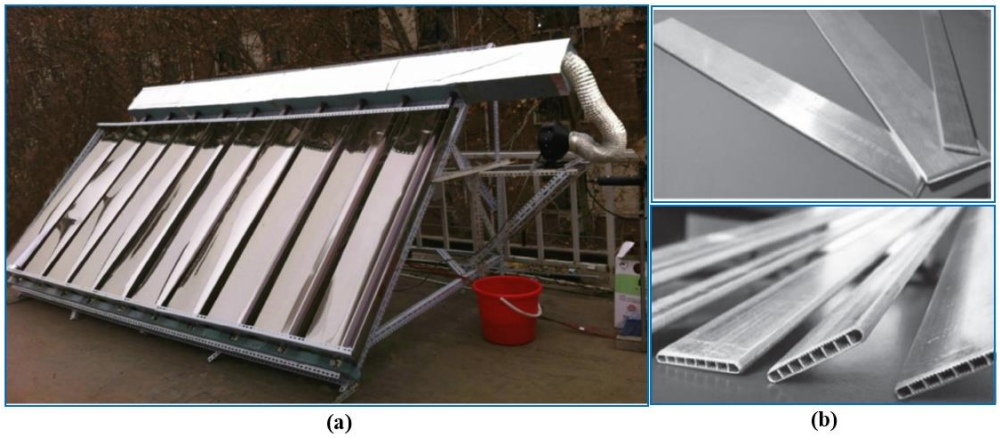

Fig. 50. Photos of: (a) CPC experimental system; (b) FMHPA [72]

Zhu et al. [72] investigated a kind of compound parabolic concentrator (CPC) solar air collector (SAC) with flat micro-heat pipe arrays (FMHPA) as shown in Fig. 49 (a) and (b). In each micro-channel tube, there involves lots of miniatures axially grooves to improve heat exchange rate. Each FMHPA could be classified into evaporator and condenser segments. According to Fig. 49 (c), the condenser of the FMHPA is inserted into the gap of two back-to-back fins whereas the evaporator of the FMHPA is embedded within the vacuum tube. The photographs of the experimental prototype and FMHPA shape are presented in Fig. 50.

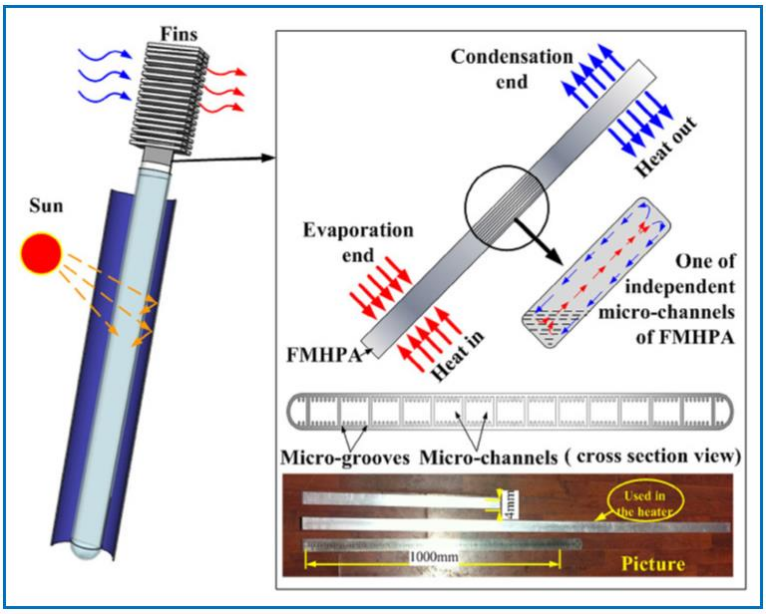

Fig. 51. The working principle of CPC with flat micro-channel pipe [72]

As illustrated in Fig. 51, the working principle of the system is that some of the incident solar radiation through the vacuum glass are directly absorbed, and the remaining of the solar radiation is subsequently reflected to the vacuum tube. Afterwards, the heat is transported to the evaporator segment of the FMHPA, and the refrigerant within the evaporator section absorbs the heat and evaporates. Meanwhile, the vapor moves up to the condenser section and condenses, then returns to the evaporator section based on capillary and gravity force. At the end, the air is warmed when it flows through the fins in the condenser section.

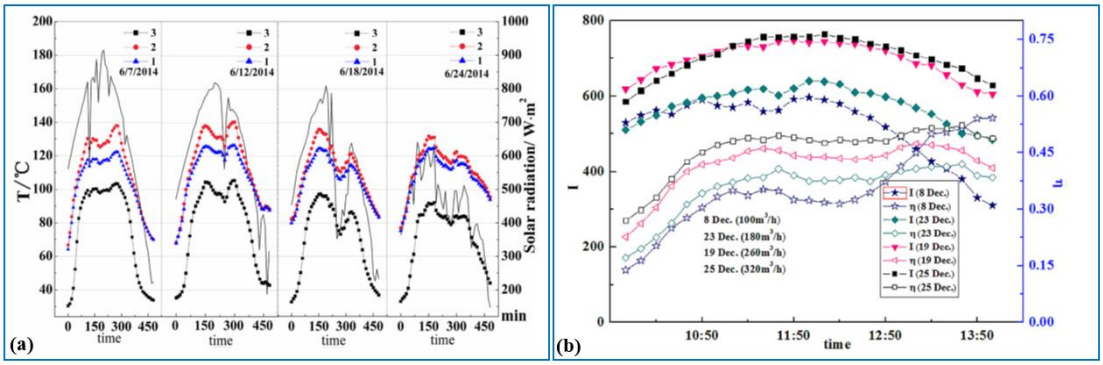

Fig. 52. Experimental results: (a) FMHPA temperature variations; (b) thermal efficiency versus time [72]

The condenser and evaporator temperature variations of the FMHPA during four days testing period are presented in Fig. 52 (a). It is found that the condenser and evaporator temperatures could reach 115.8 °C and 126.2 °C, respectively. The solar energy absorbed through the CPC is increased due to the growth in the intensity of solar radiation. Furthermore, results demonstrate from Fig. 52 (b) that the weather condition, air volume flow rate and solar radiation have significantly impact on the system thermal performance.

2.6 PV/T with U-tube

Korres and Tzivanidis [73] developed a mini-compound parabolic concentrator (CPC) with a U-type evacuated tube module in order to assess heat loss coefficient, thermal efficiency and effect of secondary flow on the absorber's temperature. As presented in Fig. 53, the straight portion of the U-tube snaps mechanically on the absorber through two circular slots formed in the last one's body. The module's equations are given in Table 5.

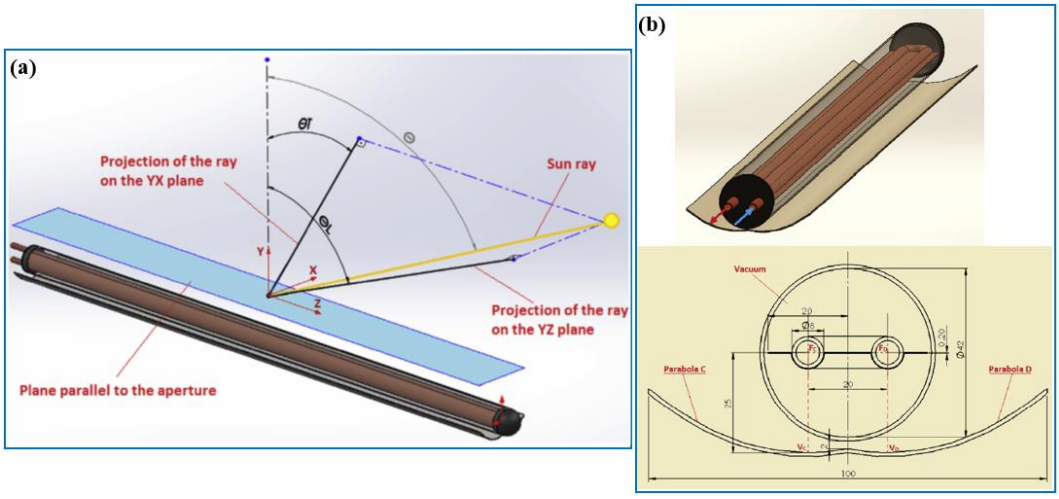

Fig. 53. Schematic diagram of: (a) CPC system; (b) novel U-type [73]

Table 5 The module's equations [73]

Description	Equations
Thermal section	$Q_u = m \cdot c_p \cdot (T_o - T_i) = h_f \cdot A_s \cdot (T_s - T_f)$ $Q_L = [h_w \cdot (T_g - T_\alpha) + \varepsilon_g \cdot \sigma \cdot (T_g^4 - T_\alpha^4)] \cdot A_{g,o} = \frac{A_p \cdot \sigma \cdot (T_g^4 - T_\alpha^4)}{\frac{1}{\varepsilon_p} + \frac{1-\varepsilon_g}{\varepsilon_g} \cdot \frac{D_p}{D_{g,i}}}$ $Q_s = A_a \cdot G_T$
Thermal efficiency	$\eta = \frac{Q_u}{Q_s}$
Total heat loss coefficient	$U_L(\text{Absorber} - \text{Glass}) = \frac{\sigma \cdot (T_p^4 - T_g^4)}{\frac{1}{\varepsilon_p} + \frac{1-\varepsilon_g}{\varepsilon_g} \cdot \frac{D_p}{D_{g,i}}} \cdot \frac{1}{T_p - T_a}$ $U_L(\text{Glass} - \text{Ambient}) = \frac{h_w \cdot (T_g - T_a) + \varepsilon \cdot \sigma \cdot (T_p^4 - T_g^4)}{T_p - T_a} \cdot \frac{A_{g,o}}{A_p}$
Optical efficiency	$\eta_{opt,\Theta} = \gamma_\Theta \cdot (\tau \cdot \alpha) \cdot [1 - (1-\rho) \cdot \frac{Q_{R,0}}{Q_s}] = \gamma_\Theta \cdot (\tau \cdot \alpha) \cdot f(\rho)$

The effects of longitudinal and transversal incident angles of the sun rays on the optical efficiency are investigated by comparing its optical performance with the flat collector's. Results in Fig. 54 reveal that the longitudinal incident angle has less influence on the collector performance whereas the transversal one contributes to enhance the optical performance. Meanwhile, it can be found from Fig. 55 that the absorber temperature rises along the direction of fluid flow and reduces neighbouring the bend and

the exit of the collector. It is discovered that the longitudinal incident angle has a little influence on the PV/T system performances whereas the circular absorber appears better optical performance in comparison with the flat one.

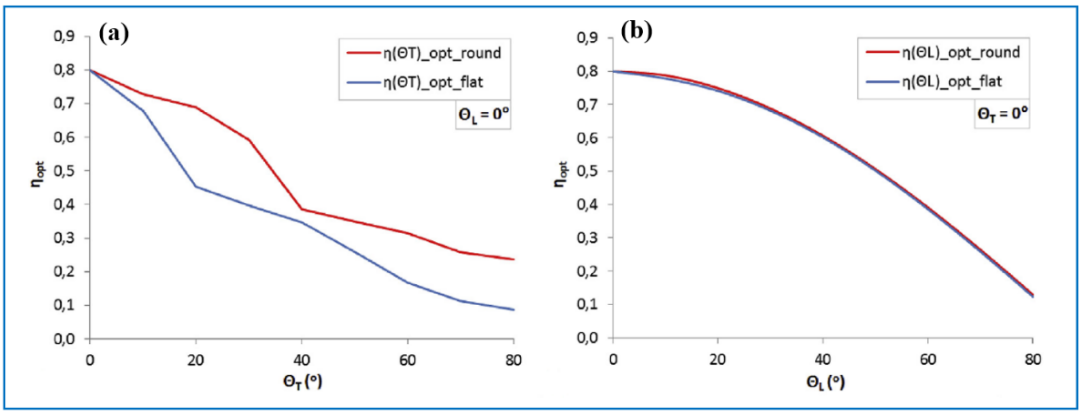

Fig. 54. Optical performance results of angle of incidence: (a) transversal; (b) longitudinal [73]

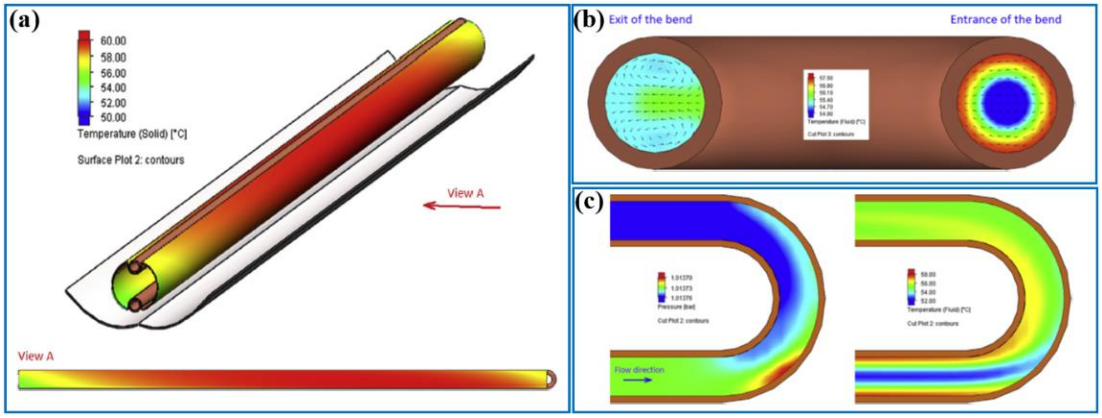

Fig. 55. Effect of secondary flows on the absorber' temperature: (a) absorber's surface temperature distributions; (b) vertical view; (c) cross-sectional view [73]

Gu et al. [74] performed an economic analysis of a CPV/T system to assess the effects of concentrator initial cost on the levelized cost of energy (LCOE), net present value (NPV) and payback period (PP) by using the Monte Carlo method in Sweden. Their results shown from Fig. 56 that when the concentrator initial cost is increased from 3000 SEK/m^2 to 5500 SEK/m^2, the LCOE varies from 0.81 SEK/kWh to 1.48 SEK/kWh and the PP goes up from 5.63 years to 11.89 years. This means that high concentrator initial cost causes high system capital investment and loan cost, thereby, it has the negative influence on the three economic indicators, decreasing NPV and increasing PP/LCOE. Therefore, it is recommended that the initial cost of the concentrator should become as low as possible for a better market penetration.

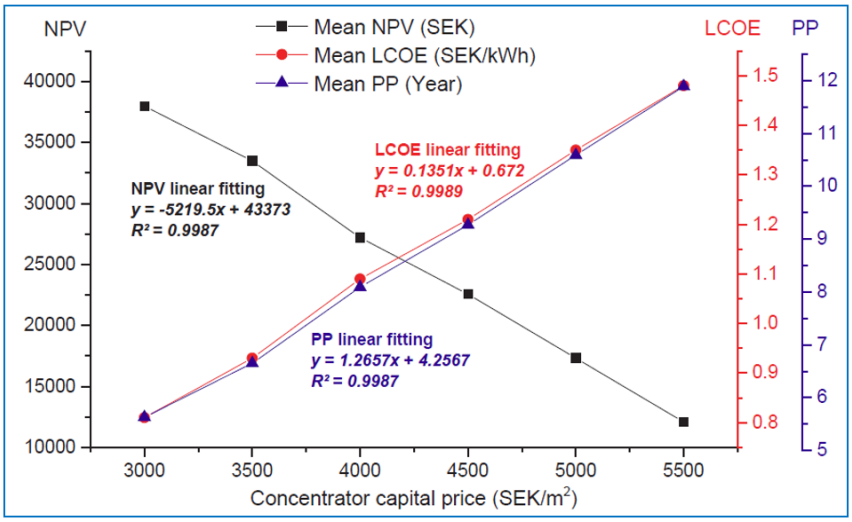

Fig. 56. Concentrator initial cost vs NPV, PP and LCOE [74]

Riggs [75] implemented an economic assessment of a CPV/T system by using the levelized cost of heat (LCOH) method in the USA. It can be observed from Fig. 57 that when the initial cost is increased by 75% of the whole investment, the LCOH could be reduced by 60%. Boudries et al. [76] implemented an economic assessment of a CPV/T system in Algeria. Results concluded from Fig. 58 that when the solar concentration ratio (C) is relatively low, the cost of CPV/T system is dominated by the concentrating photovoltaic unit-elated cost. Meanwhile, the solar irradiation and system efficiency are improved when this fractional cost drops, while the CPV-related cost drops rapidly with the growth of solar concentration.

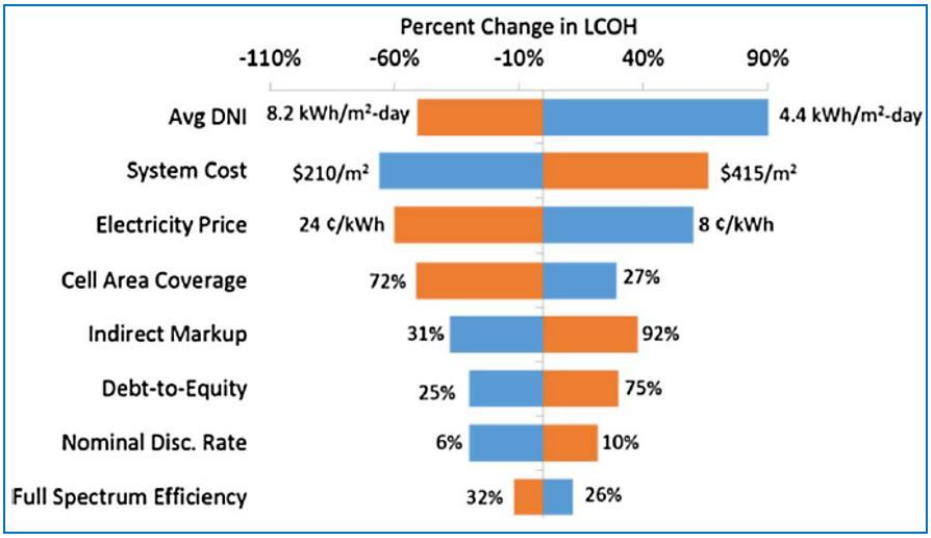

Fig. 57. Tornado analysis of CPV/T system [75]

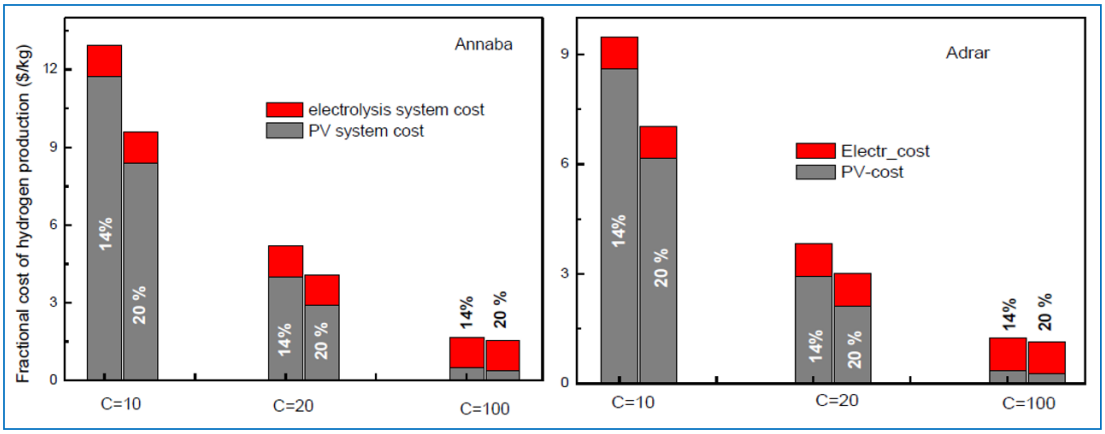

Fig. 58. Comparison of the solar CPV/T system based on different cell efficiency [76]

2.7 PV/T with triangular tube

Gunasekar et al. [77] developed a mathematical model and implemented a testing analysis for a solar PV/T with triangular tubes to predict the system performance in India. Fig. 59 gives the photographic vision of the system.

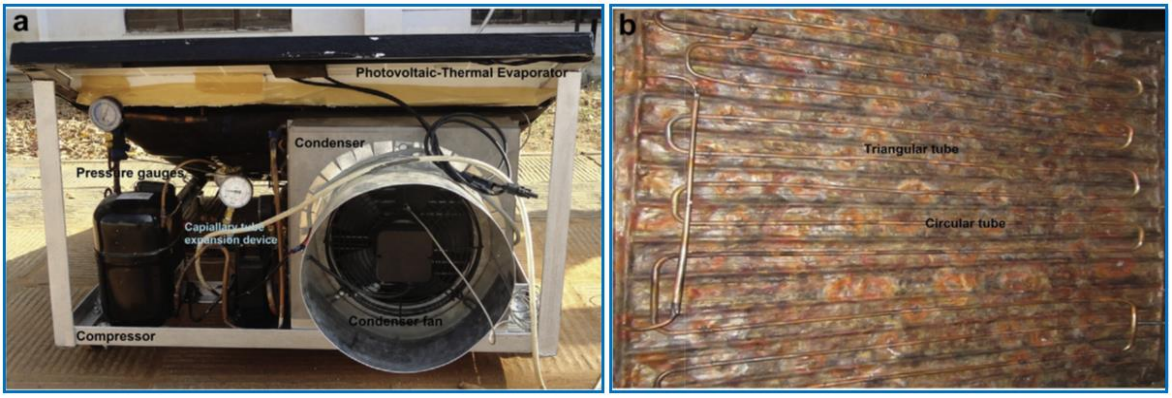

Fig. 59. Photos of: (a) testing bench; (b) triangular tubes [77]

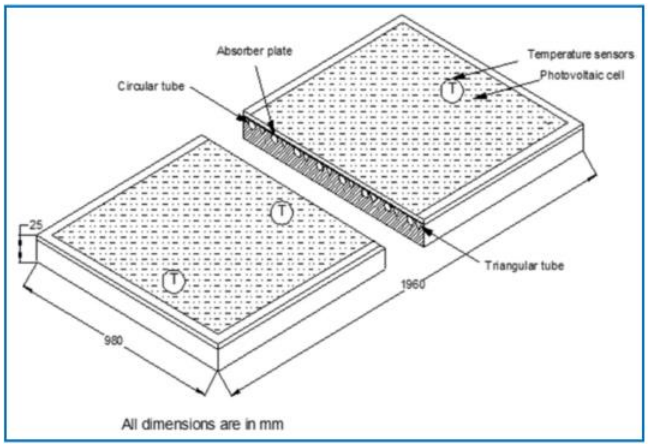

Fig. 60. Sectional views of PV/T with triangular tubes [77]

It can be observed from Fig. 60 that the PV/T module has an area of 1.92m^2 (1.96m × 0.98m), a copper plate of 1.2 mm thickness and 10 mm equilateral triangular tubes. The PV array is utilized to cover the collector plate at the top surface, meanwhile, 10

mm thickness poly-euro-ethylene foam that is placed at the bottom of the plate contributes to decrease heat interaction. The mathematical equations of the PV/T with triangular tubes are illustrated in Table 6.

Table 6 The mathematical equations of PV/T with triangular tubes [77]

Description	Equations
Solar energy input ratio	$\delta SEIR = [(\frac{\delta m_a}{m_a})^2 + (\frac{\delta P}{mP})^2 + (\frac{\delta T_6}{T_6})^2 + (\frac{\delta I}{I})^2 + (\frac{\delta T_5}{T_5})^2 + (ANN)^2]^{1/2}$ $SEIR = \frac{A \times I \times \alpha}{Q_{PV/T}}$
PV efficiency	$\eta = \frac{PV_{output}}{A \times I}$
Fraction of absolute variance (R^2)	$R^2 = 1 - \frac{\sum_{m=1}^{n}(y_{pre,m} - t_{mea,m})^2}{\sum_{m=1}^{n}(t_{mea,m})^2}$
Root mean square error (RMS)	$RMS = \sqrt{\frac{\sum_{m=1}^{n}(y_{pre,m} - t_{mea,m})^2}{n}}$
Coefficient of variance (COV)	$COV = \frac{RMS}{\sum_{m=1}^{n}(t_{mea,avg})} \times 100$

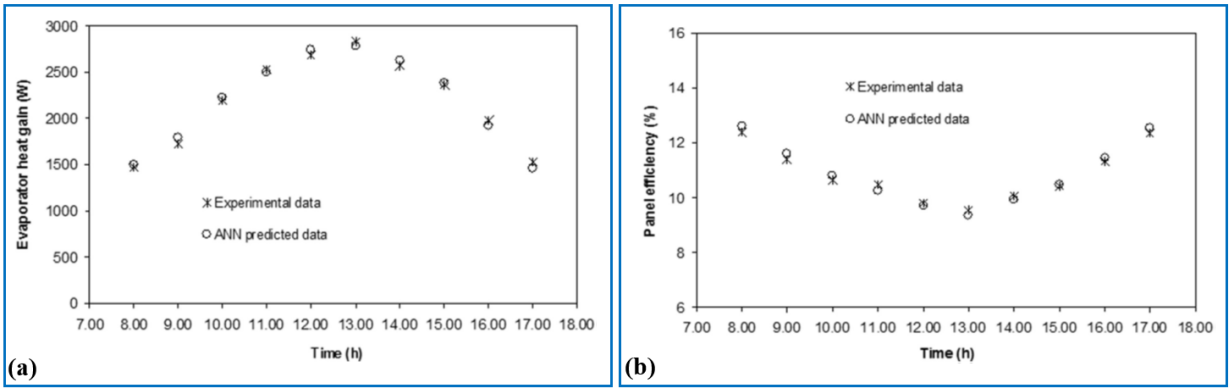

Fig. 61. Results comparison: (a) evaporator heat gain; (b) PV efficiency [77]

The artificial neural networks (ANN) expected and experimental evaporator heat obtained data are presented in Fig. 61. Results indicate that the minimum root mean square (RMS), the maximum fraction of absolute variance and coefficient of variance (COV) values are 2.036 W, 0.9999 and 0.0932 respectively.

2.8 PV/T with heat mat

Jouhara et al. [78, 79] developed a PV/T with heat mat system, and found that the mat material can be combined with a building envelope to form a roof as described in Fig. 62 (a). Specifically, the heat mat has a unique inner fin faced the solar irradiation, which is utilized to improve heat transfer. Meanwhile, it is cooled by employing a manifold which is attached to the back of the heat pipe using removable securing device. The heat mat length and width are 4m and 0.4m, respectively. The construction of the panel and its cross-section view are given in Fig. 62 (b) and (c).

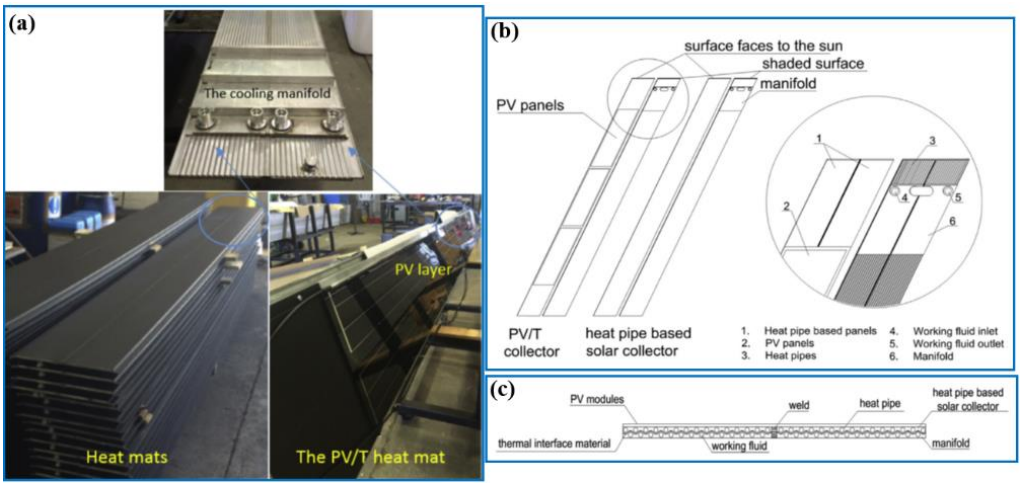

Fig. 62. Schematic diagram of PV/T with heat mat: (a) prototype; (b) construction; (c) cross-section view [78, 79]

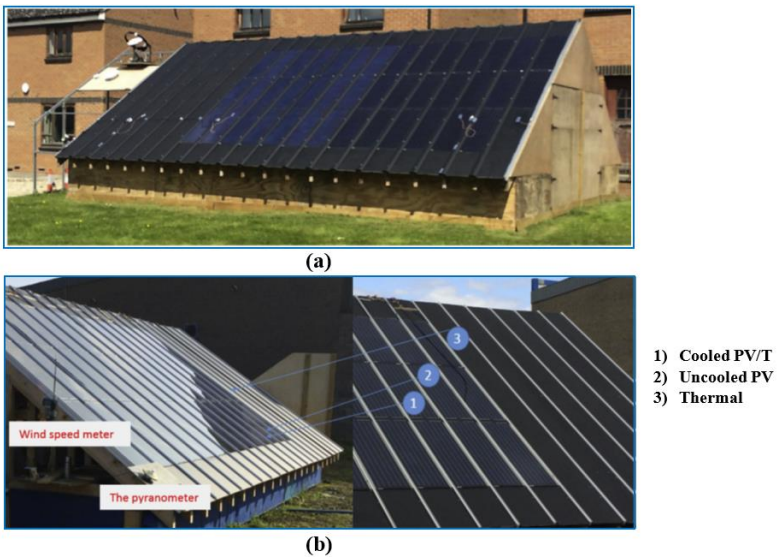

Fig. 63. Photos of: (a) PV/T with heat mat system test field; (b) selected panel [78]

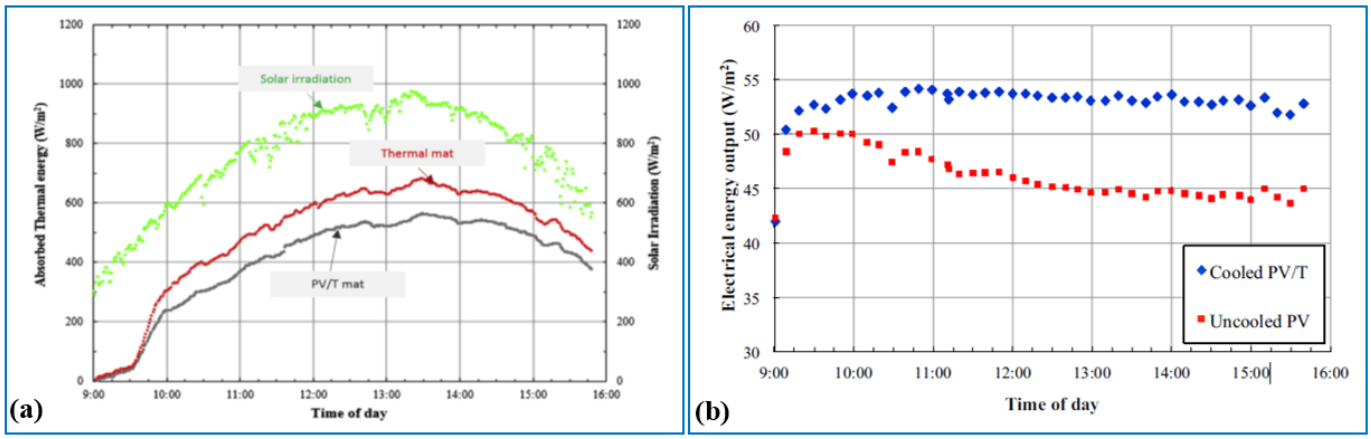

Fig. 64. Experimental results: (a) thermal output; (b) influence of cooling on the electrical output [78]

The experimental apparatus of the PV/T with heat mat is given in Fig. 63. The testing is performed for 4 days from 9:00 to 16:00 in September of 2014. The working fluid flow rate is constant for each cooling manifold at 1 L/min. As indicated in Fig. 64 (a),

the absorbed thermal energy from thermal mats is greater. The mean energy conversion efficiencies are about 50% for the PV/T mat and 64% for the thermal mat. According to Fig. 64 (b), the cooling of the PV/T heat mats results in a growth in electrical efficiency approximately 15%. Later, Khordehgah et al. [80] setup a detail simulation model to study the system performance for heating application by the TRaNsient System Simulation (TRNSYS) software, the simulation process is shown in Fig. 65.

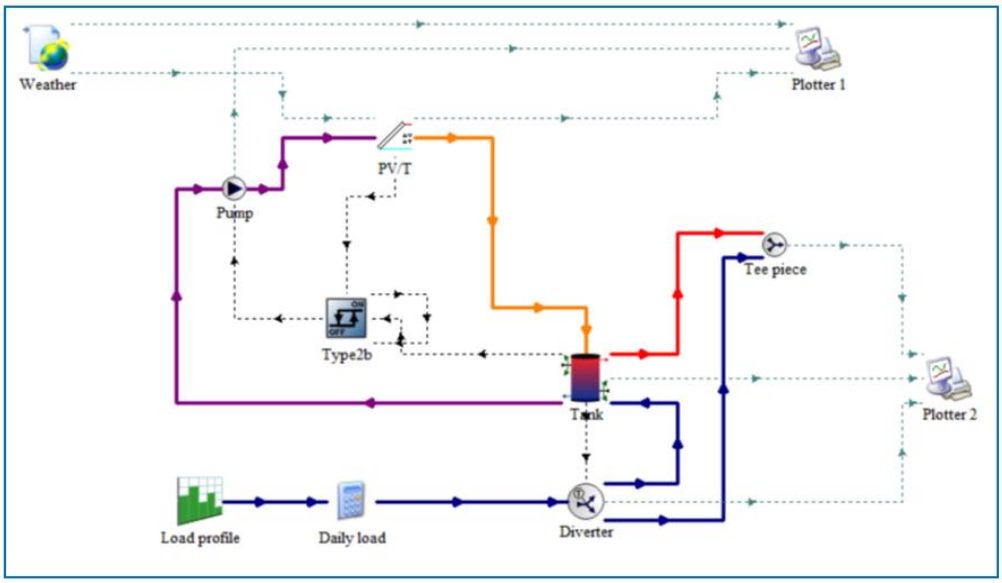

Fig. 65. Simulation process of PV/T with heat mat system in TRNSYS [80]

One-year simulation period is adopted to study hot water and electrical productions under various solar radiation conditions. According to Fig. 66, results confirm that the surface temperature of the module is declined by about 25%, in the meantime, the cooling of the PV array could rise the system power output by about 15% as illustrated in Fig. 67.

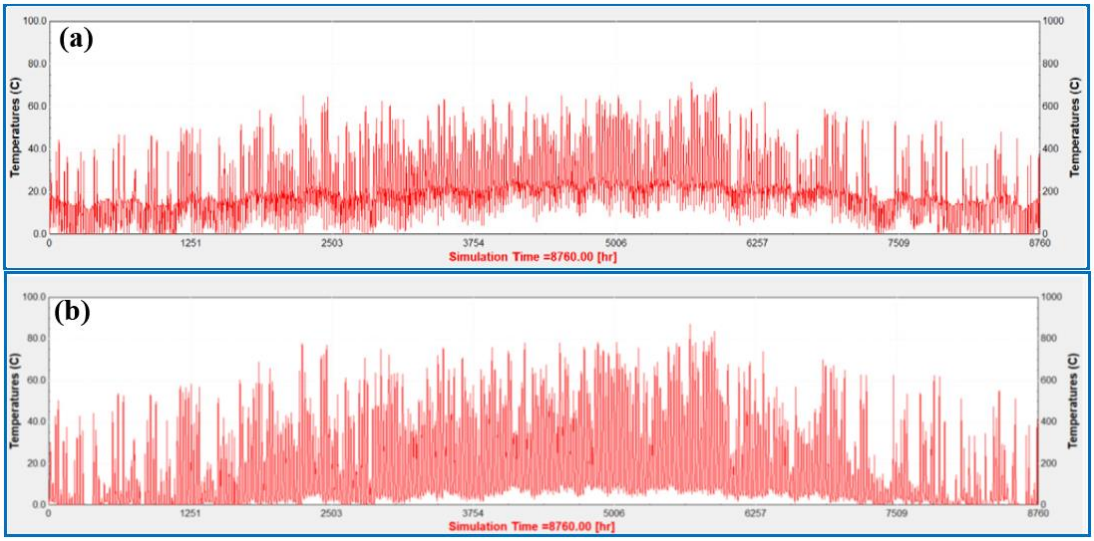

Fig. 66. Solar cell temperature: (a) without cooling; (b) with cooling [80]

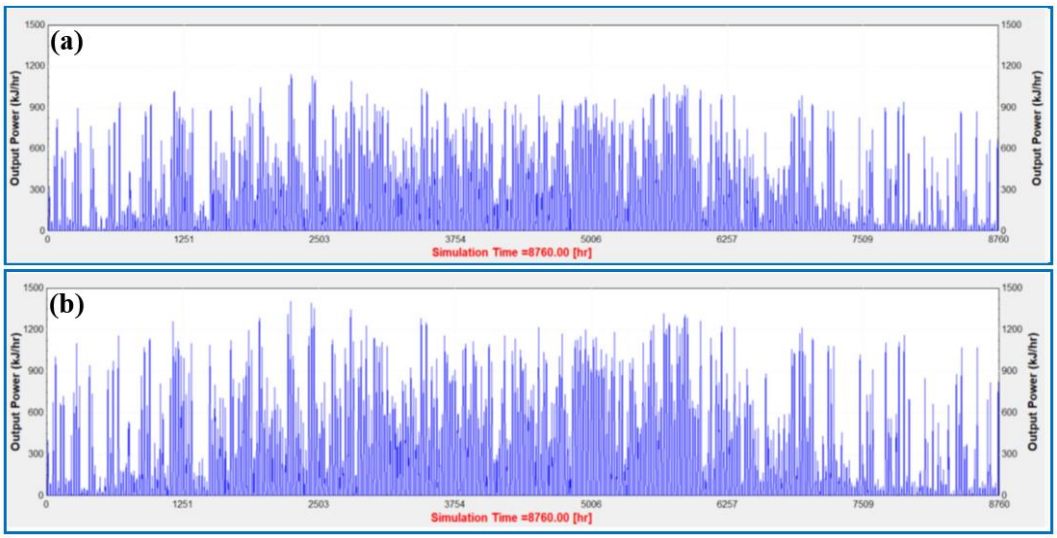

Fig. 67. Power output: (a) without cooling; (b) with cooling [80]

2.9 Comparison of different configurations

Various PV/T configurations have been generalised based on the different loop-pipes, such as the micro-channel, heat pipe, U-tube, vacuum tube, roll-bond, triangular tube, heat mat and heat exchanger to enhance thermal and electrical output and their efficiencies. These innovative configurations have higher heat transfer rate, higher electrical and thermal energy output as well as lower heat loss in comparison with traditional system's. As a result, the most recent investigations on the PV/T configurations, materials of loop-pipes, working fluid and their system applications associated with the remarks and critical findings are illustrated in Table 7.

Table 7 Comparison of PV/T configurations

Authors	Types of configurations	Climate region	Flow channel material	Working fluid	System description	Remarks and key findings
Hu et al. [49]	Wickless and wire-meshed heat pipe	Hefei, China	Copper	Water	• This system includes a PV/T with heat pipe module, 120 L of thermal tank, water pump and several valves. • The dimension of evaporating and condensing sections are Φ8 × 1 × 1300 mm and Φ24 × 1 × 90 mm, respectively.	• The system thermal efficiency with wickless and wire-meshed heat pipe are individually 52.8% and 51.5%. • The two types of system could achieve the highest thermal efficiencies when the inclination angle is setup at 40°.
Li and Sun [50, 51]	LHP	Qinhuangdao, China	Aluminum	R22	• This system consists of flat-plate PV/T module, a vertical coil condenser inserted into thermal tank, valves and connection pipes • The dimension of PV module is 125 × 125 × 64 mm. • The thickness of glass cover is 3.2 mm, the aluminum of LHP is 1.87 m^2. • 3600 r/min speed of compressor and 30 mm diameter of coil within the condenser are applied in the experimental system. • The fitting angle of the module is setup at 50°.	• The system average daily thermal efficiencies could achieve 47.25% and 42.09% in summer and winter, respectively. • The system average daily electrical efficiencies could attain 12.38% and 11.59%, respectively. • The yearly energy consumption of PV/T-LHP system is around 586 kWh which is lower than the 881.7 kWh of ASHP system. • The heat pump COP could achieve around 3.1. • Compared with traditional ASHP system, almost 30% of LCC could be saved.
Yu et al. [52, 54]	MCLHP	Shan xi, China	Aluminum	R134a	• This system involves a PV with micro-channel pipes array that is regarded as the evaporator and a condenser that is made of the co-axial tubular heat exchanger. • 0.75mm diameter of micro-channel pipes is applied. • The active area of PV module is 1.769 m^2 with 18.6% electrical efficiency.	• The thermal efficiency of the system is in the varied from 25.2% to 62.2% whereas the power efficiency is in the range from 15.59% to 18.34%. • The PV/T-MCLHP unit could achieve about 33.31% and 17.2% higher whole energy efficiency in comparison with the BIPV/T and PV/T units. • The 561W/m^2 radiation is the most suitable level for the thermal efficiency.
Widyolar et al. [57] and Abdelhamid et al. [58]	CPC with vacuum tube	USA	Aluminum	Water	• This system component contains CPC module, aluminum mini-channel pipes, GaAs covered curved mirrors, absorber and external glass tube. • CPC has an aperture width of about 110 mm, and 120 mm internal diameter of glass tube is inserted. • 5 m^2 of the parabolic mirror with half rim angle of 90 ° are applied within the system.	• The system efficiency of the CPC with U-tube is about 37% whereas the power efficiency of GaAs cells reaches 8%. • The maximum outlet fluid temperature achieves 365 °C. • The system is able to generate electricity under high temperature condition.
Zhou et al. [59, 60]	RB	Dalian, China	Aluminum	R22	• This system contains four PVT-RB modules, electronic expansion valve, 600 L ice storage tank, 150 L thermal water tank, two micro-inverters and measuring instruments. • The module's dimension is 1560 × 780 × 32 mm.	• The system electrical output and efficiency are about 250W and 8.7%, respectively. • The system thermal output and COP are about 4kW and 5.3, respectively. • The cumulative thermal energy production is about 22.1 MJ. • The cooling output ranges between 1.7 to 3.1 kW.
Lu et al. [61]	RB	Dalian, China	Aluminum	Water	• This system includes 12 PV/T modules as evaporator, a coil heat exchanger as condenser, an	• The system module average power and thermal efficiencies are about 7.51% and 49.9%, respectively.

					interior heat exchanger (IHX) and two electronic expansion valves (EEVs). • 41 cc/revolution of scroll compressor and 620 L water tank are utilized in the testing.	• The entire system module heating output, power output and consumption are individually 23.68 kWh, 0.51 kWh, and 7.24 kWh during the test period. • The mean system COP could reach 3.45.
Fayaz et al. [62] and Nasrin et al. [63]	RB with MWCNT	Malaysia	Aluminum	Water/ MWCNT nanofluid	• This system consists of PV/T with MWCNT module and solar emulators. • The aluminum pipe has a 35mm of length and 10 mm of internal diameter. • Thermal insulation is made of 5 mm thickness polyethylene foam with an R-value of 4.5. • 120 halogen bulbs as solar emulator is utilized to supply energy input.	• The system thermal, electrical and overall efficiencies are individually 75.69%, 11.96% and 87.65% based on the water/MWCNT nanofluid. • In comparison with the conventional working fluid, thermal, electrical and overall efficiencies are improved approximately 3.67%, 0.12% and 3.79%, respectively.
Abdallah et al. [64]	RB with MWCNT	Egypt	Copper	Water/ MWCNT nanofluid	• This system involves water and nanofluid cooled PV/T, standalone PV cell, 5L thermal water tank and circulation pump. • 0.3mm copper sheet is utilized as heat absorber on the back of PV module. • The properties of MWCNT contain length, internal and external diameters in the range from 5 to12 nm and from 30 to 50 nm.	• This overall system efficiencies of average daily and noontime reach 61.23% and 83.26%, respectively. • The optimum module efficiency is obtained at 0.075% V of MWCNT.
Aste et al. [65]	RB absorber	Italy	Aluminum	Water	• This system includes a PV/T module, water pump, heat storage tank and micro-inverter. • The size of PV module is 1.62 m^2 with efficiency of 14.17%. • The PV/T towards south with a tilt angle of 30°, which is connected to 200 L thermal storage tank.	• The annual total PVT module efficiencies in Athens, Milan and Paris achieve 40.6%, 32.7% and 36.1%, respectively. • The electrical efficiencies in Athens, Milan and Paris are individually 13.4%, 13.7% and 13.6%.
Zhang et al. [66]	Heat exchanger	Nanjing, China	Aluminum	R134a	• This system contains a PV/T-heat exchanger, heat pump and three-fluid heat exchanger. • The brushless fans have power of 6 W and pressure head of 40 Pa. • 5 HP scroll compressor is utilized in the system. • The fitting angle of PV/T modules is about 30°.	• Thermal energy output and efficiency are individually in the range from 2.37 kW to 2.311 kW and from 60.1% to 61.5%. • Electrical energy output and efficiency are individually in the range from 0.445 kW to 0.489 kW and from 13.9% to 15.3%. • Heat pump COP varies from 2.43 to 4.13. • In comparison with a traditional PV module, the yearly power output could increase by 14.7% while thermal energy output could improve by 31%.
Khelifa et al. [67]	Heat exchanger	Algeria	Galvanized steel	Water	• This system contains a PV/T with the galvanized steel heat exchanger that has a 130 cm length. • An absorption sheet is installed in the rear face of the PV cells which are coupled to the pipes to cool them. • The fitting angle of PV/T modules is about 35°.	• The outlet fluid temperature varies ranging between 24 °C and 40 °C. • The efficiency of PV module reduces when the PV surface temperature rises.
Zhou et al. [68, 69]	Micro-channel-evaporative module	Shan xi, China	Aluminum	R410A	• This system includes eleven PV/T with micro channel modules, condenser, 5P of compressor and electro-magnetic expansion valve (2-19.3 kW). • The PV module size is 2 m^2 (1× 2m).	• The novel PV/T with micro-channel system could reach mean overall, electrical and thermal efficiency of 69.7%, 56.6% and 15.4% respectively. • System mean COP could achieve 4.7.

					• The size of micro-channel rectangular pipe is 2 × 6 × 4 mm weld to a black chromium plate.	• Higher shear stress results in the reduction on liquid film thickness, the growth of refrigerant evaporation rate, thermal and electrical output.
Hou et al. [70]	MHPA	Beijing, China	Aluminum alloy	Water	• This system composes of two PV/T with MHPA in a series, water pump and thermal tank. • The PV module size is 1.28 m^2 (1580 × 808 × 50mm) with 185 W. • The power of pump and water tank volume are individually 50W and 100L. • 30mm of insulation material is installed on the PV module back to decrease heat loss.	• Thermal efficiency achieves 20% and 40% in heating and cooling seasons, respectively. • The electrical efficiency is comparatively steady at about 13%. • The whole system efficiency is in the range from 30% to 50% per annum.
Wang et al. [71]	FMHPA	Beijing, China	Aluminum alloy	Water	• This system involves six PV/T with MHPA modules with peak power of 195 W and with angle of 45 °. • The size of PV module is 1.125 m^2, and connected to a 200 L thermal tank. • The MHPA is fabricated based on numerous microgrooves to improve heat transfer. • The 1.3m^2·k/W thermal resistance of thermal insulation material is installed outside the module to decrease heat loss. • The compressor of heat pump has a rate of 735W.	• The mean COPs of PV/T-WSHP and PV/T-W&ASHP modes are individually 3.18 and 2.53, which are superior to the ASHP model with 2.23. • The whole PV/T system efficiency could reach 55.4% in heating season.
Zhu et al [72]	CPC-FMHPA	Beijing, China	Aluminum alloy	Water	• This system includes ten novel compound parabolic concentrator (CPC) systems, and each FMHPA has fins and evacuated glass tube. • The size of the FMHPA is 1800× 40 × 3 mm^3, and the tilt is 45 ° toward south. • The internal and external diameters of the evacuated tube are individually 47 and 58 mm.	• This system mean thermal efficiency is 52% per annum. • The mean system optical efficiency could reach 62%. • The pressure drop is lower than 36.8 Pa when the air volume flow rate ranges between 60 and 320m^3/h.
Korres and Tzivanidis [73]	Mini CPC with a U-tube type	Greece	Copper	Water	• This system consists of mini-CPC module, flat absorber and U-type evacuated collector. • The thicknesses of glass tube and flat absorber are 1 and 0.6 mm, respectively.	• The longitudinal incident angle has a little influence on the system performance. • The configuration of flat absorber has an important influence on the optical performance in comparison with the flat one.
Gunasekar et al. [77]	Triangular tubes.	India	Copper	R134a	• This SPV-THP system contains of a PV/T module with 1.92 m^2 (1.96m×0.98m), compressor, condenser and capillary tube expansion device. • The fitting angle of the system module is about 20°.	• This electricity efficiency is in the range from 9.5% and 12.5% with a mean value of approximately 11.2%. • The heat energy obtained is in the range from 1.47 to 2.83 kWh with a mean value of approximately 2.19 kWh. • The factors of solar intensity and air temperature have significant effects on the system energy performance.
Jouhara et al. [78]	Heat mats	Cardiff, UK	Aluminum	Ammonia	• This system includes 6 flat heat pipe solar panels, pumps, storage tank and value. • Each PV module has a width of 0.4m and length of 4m. • The working fluid flow rate is about 1 L/min. • The fitting angle of the system module is about 51°.	• The thermal energy conversion of the system varies from 45.4% and 64.2%. • The system thermal efficiency could achieve ranging between 35% and 52%. • The system could overlay approximately 60% of the hot water need when the solar radiation is relative low.

						• The system could cover 100% of the hot water need when the solar radiation is high.
Jouhara et al. [79] and Khordehgah et al. [80]	Heat mats	Cardiff, UK	Aluminum	60% water and 40% glycol	• This system includes flat heat pipe solar panels, pumps and 150 L of thermal storage tank. • Each PV module has a width of 0.4m and length of 4m. • The fitting angle of the system module is about 36°.	• The system thermal efficiency could achieve about 64% whereas the power efficiency is about 15%. • The heat mat is able to improve the energy efficiency even without solar radiation.

3. PV/T with nanofluid

Nanofluids can be utilized to enhance the PV/T system performance, this is owing to the nanofluid high thermal conductivity, the main nanoparticles in the nanofluid include Zinc-oxide (ZnO), Copper-oxide (CuO), Aluminum-oxide (Al_2O_3), Silicon carbide (SiC), Tribute (Hg), Magnesium-oxide (MgO), Cerium-oxide (CeO_2), Tungsten-oxide (WO_2), Titanium-oxide (Ti_2O_3), Zirconia-oxide (ZrO_2), graphene and carbon. Therefore, the influences of the nanofluids on the PV/T system performance are generalized in the following section.

3.1 PV/T with aluminium-oxide nanofluid

Ghaderian and Sidik [81] investigated the influence of using Al_2O_3 as the refrigerant on system thermal performance of a solar collector. The X-ray diffraction (XRD) results are obtained at a scan speed of 1°/min ranging from 5° to 70° by XRD machine as given in Fig. 68 (a). Meanwhile, the field emission scanning electron microscope (FESEM) photograph of Al_2O_3 nanoparticle is presented in Fig. 68 (b). In this study, a two-step method including stabilisation and low agglomeration is used to prepare the Al_2O_3 nanofluid. Furthermore, in term of calculating the Al_2O_3 nanoparticle weight, the basic expression equations are given in Table 8.

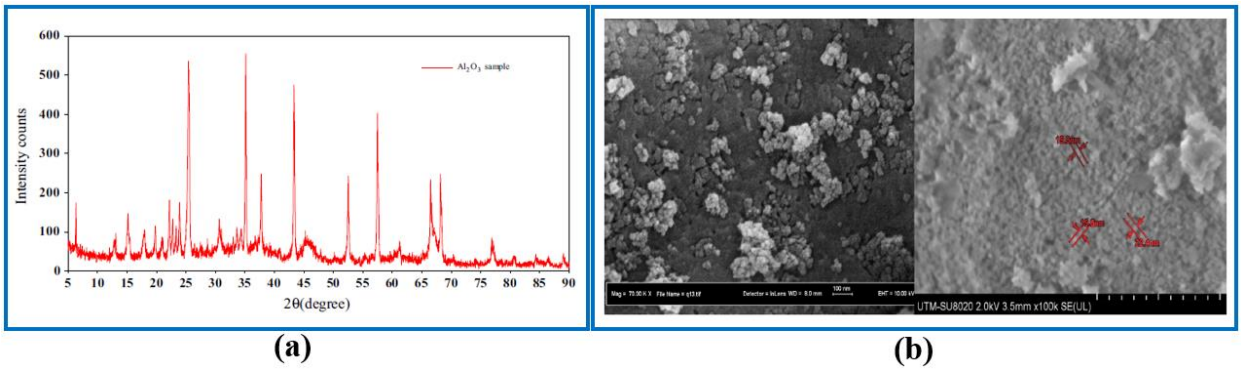

Fig. 68. (a) XRD analyses results; (b) FESEM photo of Al_2O_3 nanoparticle [81]

Table 8 The weighting equations of Al_2O_3 nanoparticle [81]

Description	Equations
Weight fraction of nanoparticles in nanofluid	$\varphi = \frac{V_{np}}{V_{nf}}$
Quantity of nanofluids	$V_{nf} = V_{np} + V_{bf}$
Quantity of base-fluid	$V_{bf} = \frac{W_{bf}}{\rho_{bf}}$
Quantity of nanoparticle	$V_{np} = \frac{W_{np}}{\rho_{np}}$

According to Fig. 69, the system maximum efficiency could achieve 57.63% at the mass flow rate of 60 litre/hour and concentration of 0.06 vol. %. This indicates that the Al_2O_3 nanofluid contributes to improving heat absorption of solar energy and thermal energy conversion efficiency.

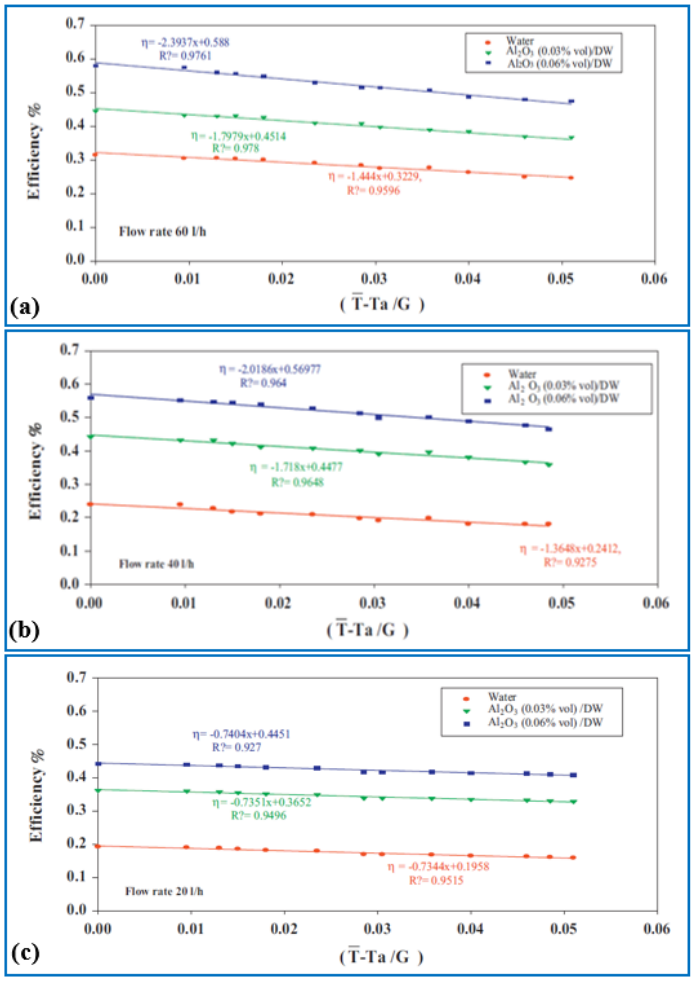

Fig. 69. Testing results of system efficiency for different flow rates: (a) 60 litre/hour; (b) 40 litre/hour; (c) 20 litre/hour [81]

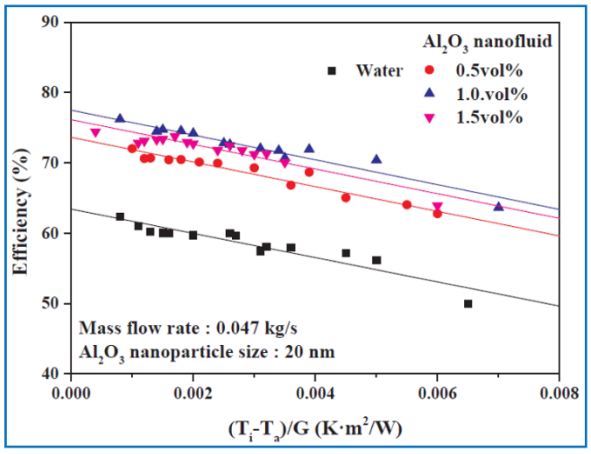

Fig. 70. Thermal efficiency comparison between water and different concentration of Al_2O_3 nanofluids [82]

Tong et al. [82] studied the performance of a PV/T system when the different concentration Al_2O_3 nanofluids are utilized as the working fluid, and found that when the concentrations of the Al_2O_3 nanofluid are 1.5 vol. %, 1.0 vol. % and 0.5 vol. %, the system efficiencies could attain up to 76.1%, 77.5% and 73.8%, respectively, and these are enhanced remarkably in comparison with that using water with 63.6% as given in Fig. 70.

3.2 PV/T with copper-oxide nanofluid

Tong et al. [82] implemented an experimental analysis of a PV/T system via using water as the refrigerant, and found that the maximum system efficiency could achieve 63.6% when the mass flow rate is setup at 0.047 kg/s as presented in Fig. 71. By comparison, when 0.7 vol. % 0.5 vol. %, 0.3 vol. % and 0.1 vol. % CuO nanofluid are adopted within the PV/T system, the efficiencies are enhanced by 10.1%, 13.4%, 16.2% and 15.6%, respectively. This means that the efficiency of the system using CuO nanofluid is higher in comparison to the case using water.

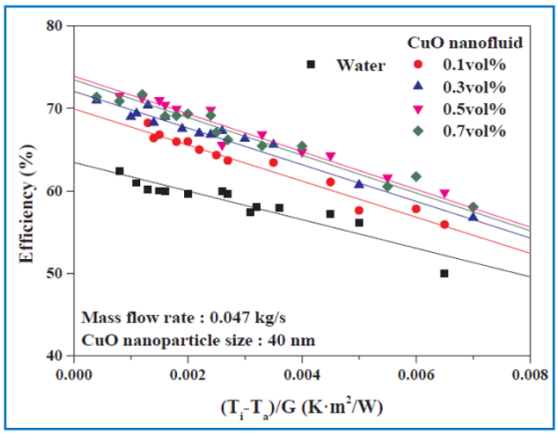

Fig. 71. Thermal efficiency comparison between water and different concentration of CuO nanofluids [82]

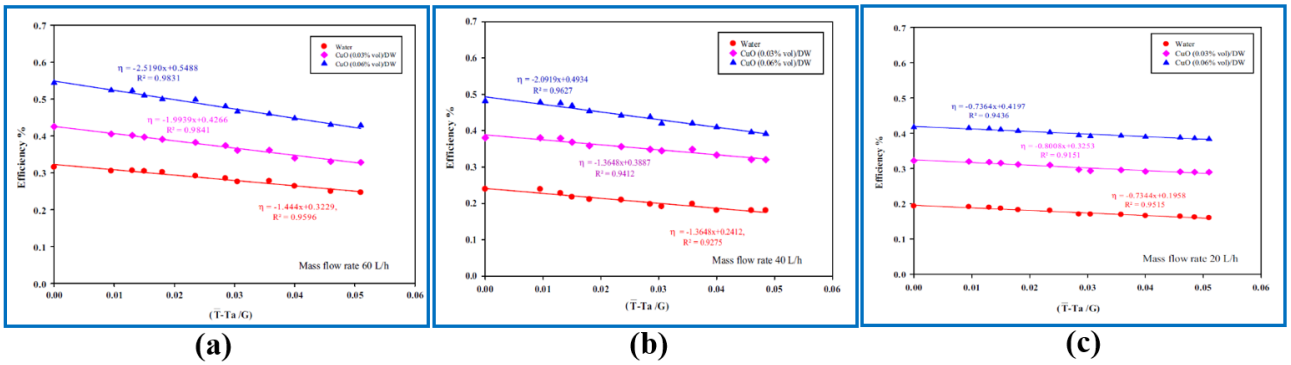

Fig. 72. Experimental results of optical efficiency at various volume flow rates: (a) 60 litre/hour; (b) 40 litre/hour; (c) 20 litre/hour [83]

Ghaderian et al. [83] exploited the effect of CuO nanofluids on the PV/T system performance for two different concentrations of 0.03 vol. % and 0.06 vol. % under three different mass flow rates (60, 40 and 20 litre/hour), and concluded that the system efficiency is proportional to the volume concentration of the CuO nanofluid, in which the efficiency is improved to 41.9% for 0.03 vol.% of CuO and 51.4% for 0.06 vol. % of CuO in comparison with water, as displayed in Fig. 72.

Qu et al. [84] compared the optical absorption and thermal-electrical conversion performance for the PV/T system with CuO-MWCNT and CuO nanofluids. The transmission electronic microscope (TEM) photographs of the two nanofluids are shown in Fig. 73. It is found that spherical CuO nanoparticle is well dispersed with comparatively uniform particle size distribution whereas the CuO nanoparticle in hybrid CuO-MWCNT/water nanofluid is largely distributed among the MWCNT fibers uniformly, meanwhile, some nanoparticles are adsorbed upon the fibre surface.

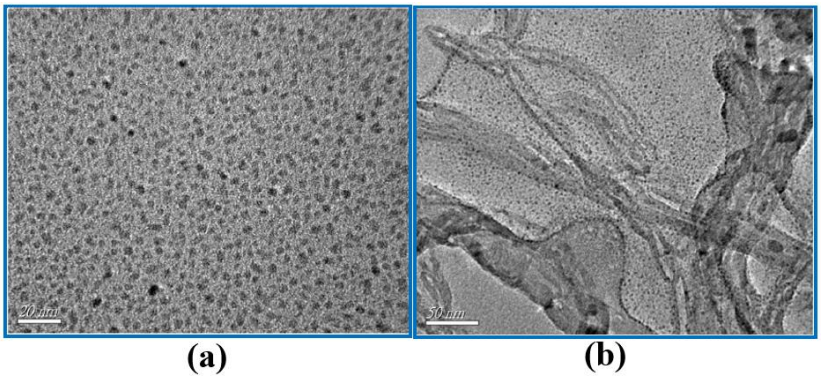

Fig. 73. (a) TEM photos of CuO/water nanofluid; (b) hybrid CuO-MWCNT/water nanofluid [84]

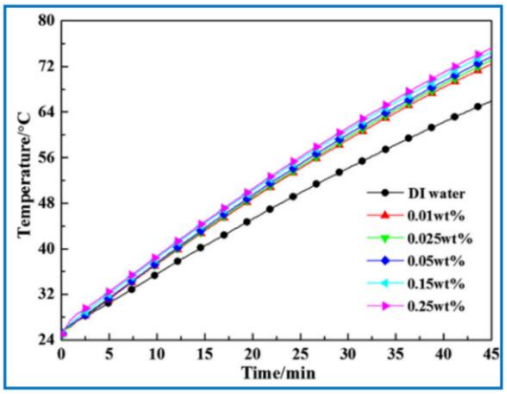

Fig. 74. Temperature variation of CuO nanofluids at various concentrations [84]

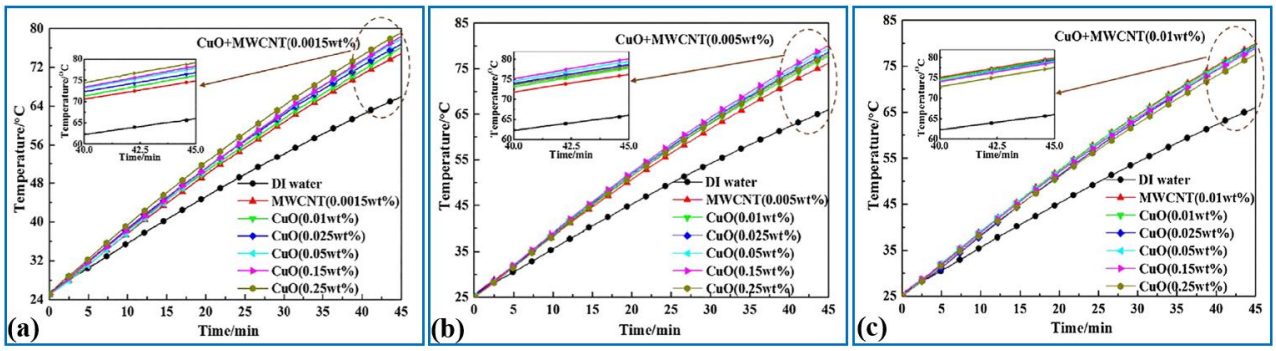

Fig. 75. System temperature variation at different concentrations [84]

As illustrated in Fig. 74, the system water conversion efficiency is obviously improved when the CuO nanoparticle is added into the system, and the temperature of the CuO nanofluid enhances with the nanoparticle concentration. When the concentration reaches 0.25 vol. %, the CuO nanofluids temperature is increased by 9.2 °C. As depicted in Fig. 75, the temperature increases at

the beginning and then decreases with the CuO concentration when the concentration of the MWCNT is 0.005 vol. %, whereas the hybrid CuO nanofluid temperature only increases about 14.1 °C superior to that of water when the concentration of the MWCNT is 0.15 vol. %.

3.3 PV/T with silicon carbide nanofluid

Al-Waeli et al. [85] explored the influence of silicon carbide (SiC) nanofluid on a PV/T system and compared with conversional PV/T system. Fig. 76 displays the FESEM photo of SiC nanoparticles. It is concluded from Fig. 77 (a) that the system with SiC nanofluid reaches 101.26% higher thermal energy output compared with that using water. Meanwhile, the proposed system electrical energy output is enhanced by 57% compared to the conventional PV module's as displayed in Fig. 77 (b). Moreover, the total system efficiency could achieve 84% and is superior to the efficiency of water cooled PV/T as shown in Fig. 77 (c).

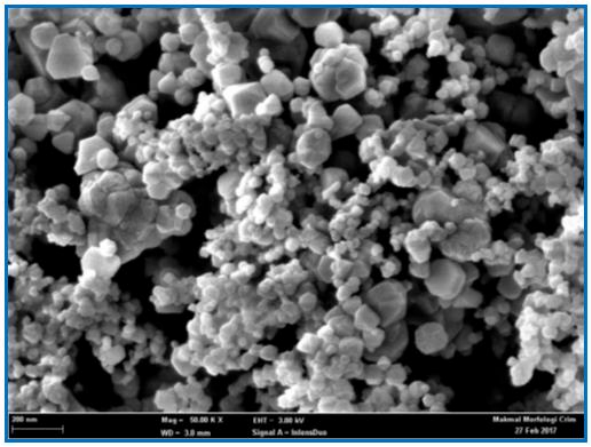

Fig. 76. FESEM photo of SiC nanoparticles [85]

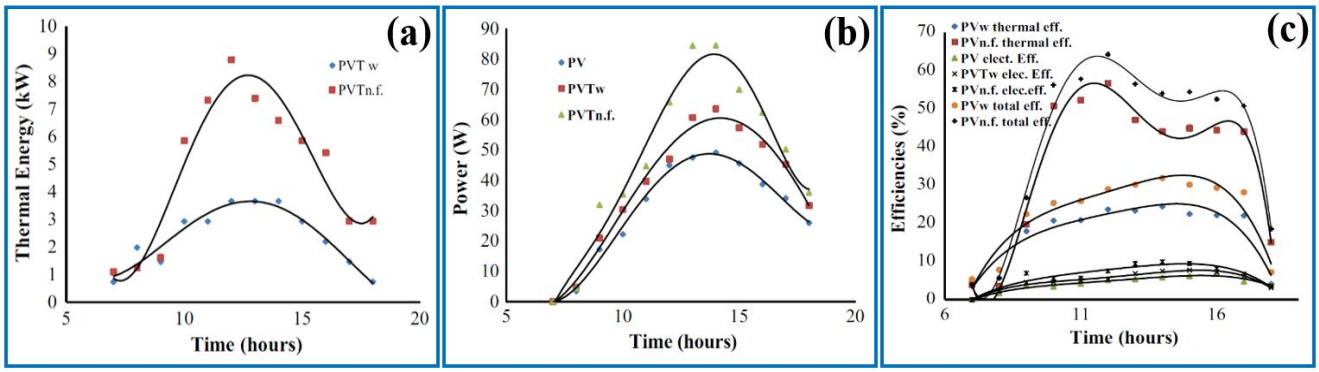

Fig. 77. The time variation vs: (a) heat energy; (b) electricity energy; (c) efficiencies [85]

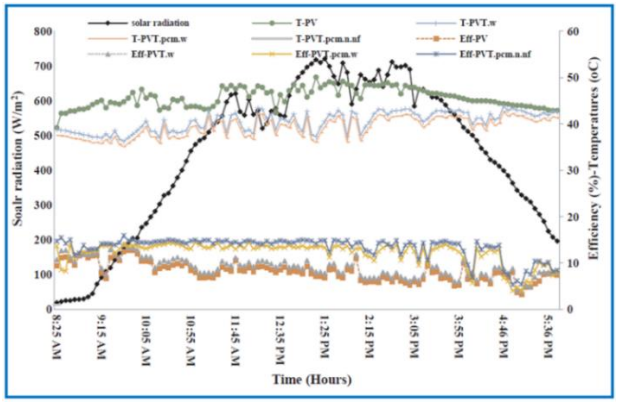

Fig. 78. Experimental results of PV/T system performance [86]

Afterwards, Al-Waeli et al. [86, 87] implemented a testing on a novel SiC nanofluid and PCM-nano (SiC-Paraffin) based PV/T system. Their results conclude that the system highest efficiency is 13.7% which is better than the SiC nanofluid system efficiency of 11.3% and the water system efficiency of 7.1% as shown in Fig. 78. These indicate that the PV/T system with the PCM-nano (SiC-Paraffin) nanofluid is capable of improving the system electrical efficiency significantly owing to the reduction of PV cell temperature.

3.4 PV/T with tribute nanofluid

Aberoumand et al. [88] used Tribute (Ag)/water nanofluid as working fluid in the PV/T system, and exploited its heat and power efficiencies by the electrical explosion of wire (EEW) method. The photos of transmission electron microscopy (TEM) and scanning electron microscopy (SEM) are exhibited in Fig. 79 (a) and (b). The structures of Ag nanoparticle and water molecule are associated with hydrogen bonds and displayed in Fig. 79 (c). It can be concluded from Fig. 80 that the nanofluid with high concentration has a significant enhancement for the system electrical energy output ranging from 8% to 10%. Meanwhile, both heat and power efficiencies of the system with Ag nanofluid could be enhanced approximately 14% compared to those with water in the same condition.

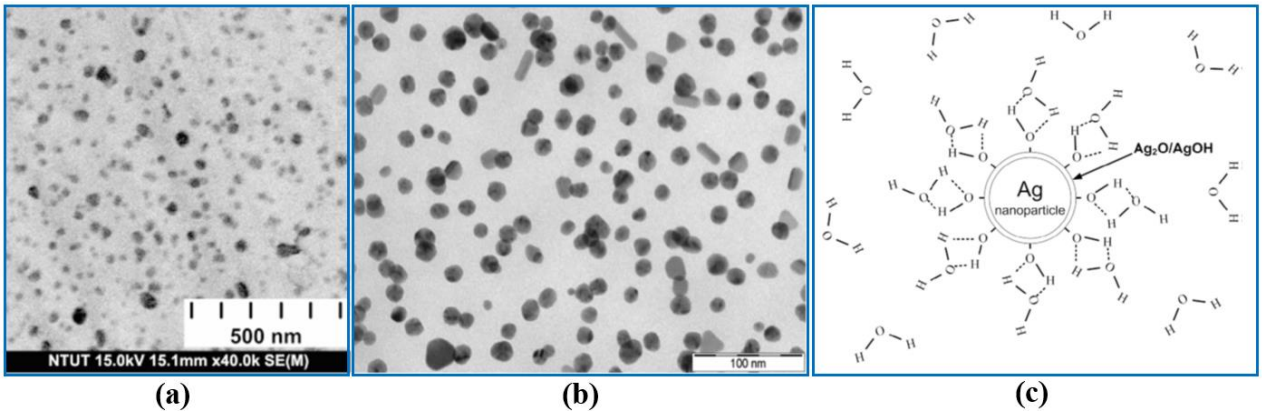

Fig. 79. Schematic diagram of Ag nanofluid: (a) SEM; (b) TEM; (c) structure [88]

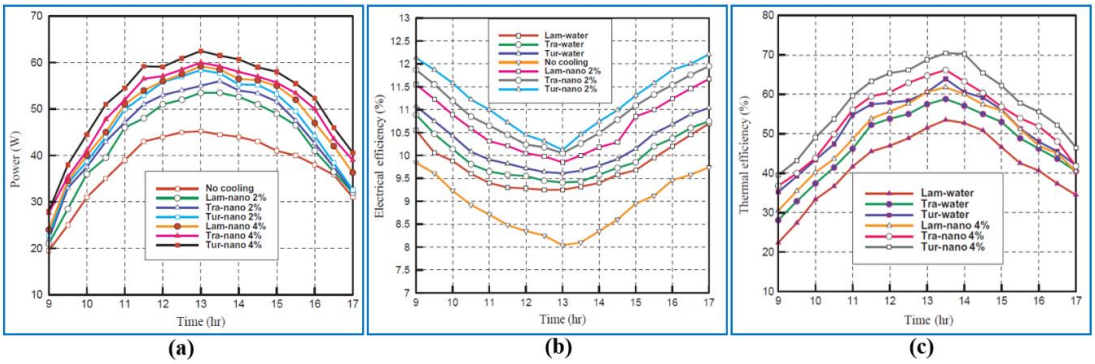

Fig. 80. Experimental results at different Ag nanofluid concentrations of 2 and 4 vol.% : (a) power output; (b) electrical efficiency; (c) thermal efficiency [88]

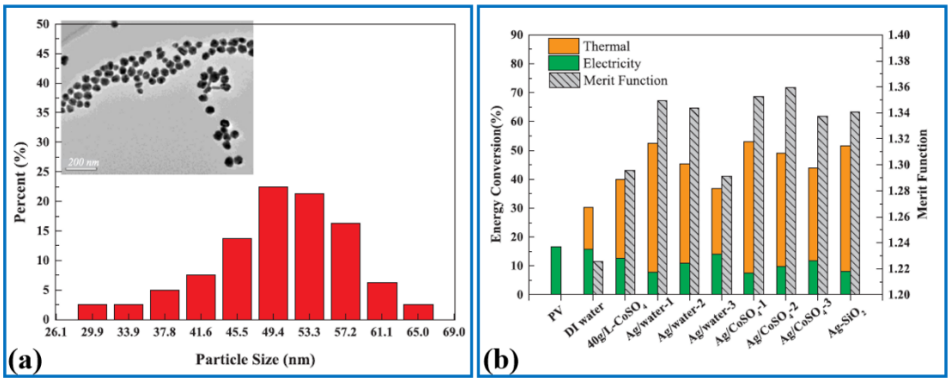

Fig. 81. Schematic diagram of: (a) Ag-$CoSO_4$ nanoparticles size; (b) energy conversion [89]

Han et al. [89] compounded a hybrid Ag-$CoSO_4$ nanofluid utilized as the working fluid within a PV/T system. The size distribution of Ag-$CoSO_4$ nanoparticles and TEM image are presented in Fig. 81 (a). Results demonstrate that the particle diameter is in the range from 41.6 nm to 57.2 nm making up around 80%. The merit function (MF), power and heat output efficiencies are illustrated in Fig. 81 (b). The highest optical efficiency of 53.1% is achieved by using Ag-$CoSO_4$-1 nanofluid in the system.

3.5 PV/T with magnesium-oxide nanofluid

Dehaj and Mohiabadi [90] proposed an evacuated heat pipe solar collector (HPSC) with Magnesium oxide (MgO) nanofluid. The optical and structural properties of the MgO nanoparticles with a mean size of 51 nm are exhibited in Fig. 82. The variations of the HPSC system efficiency at various mass flow rates are exhibited in Fig. 83. It can be found that the system efficiency with the MgO nanofluid is superior to that with water because of higher thermal conductivity of the MgO nanofluid. And also, the system efficiency increases with the volume fraction in the range of 0.014% to 0.032%.

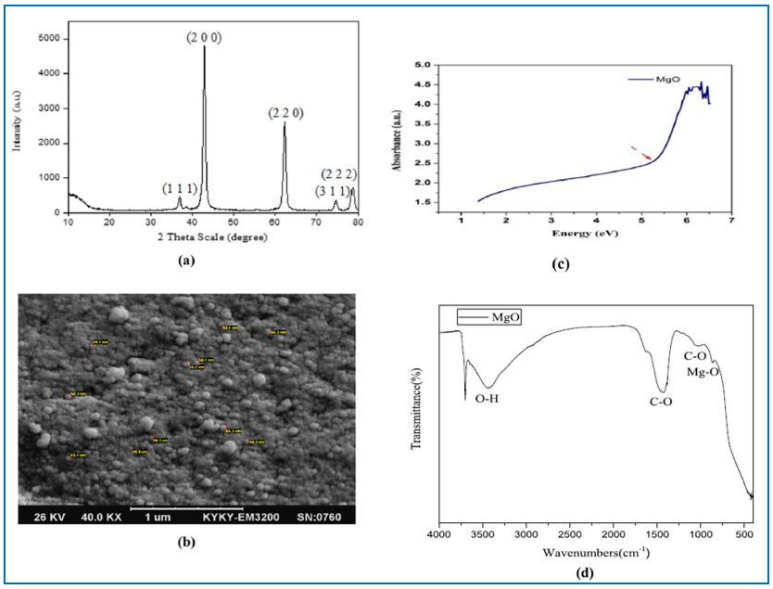

Fig. 82. Schematic diagram of optical properties and structural of the MgO nanoparticles [90]

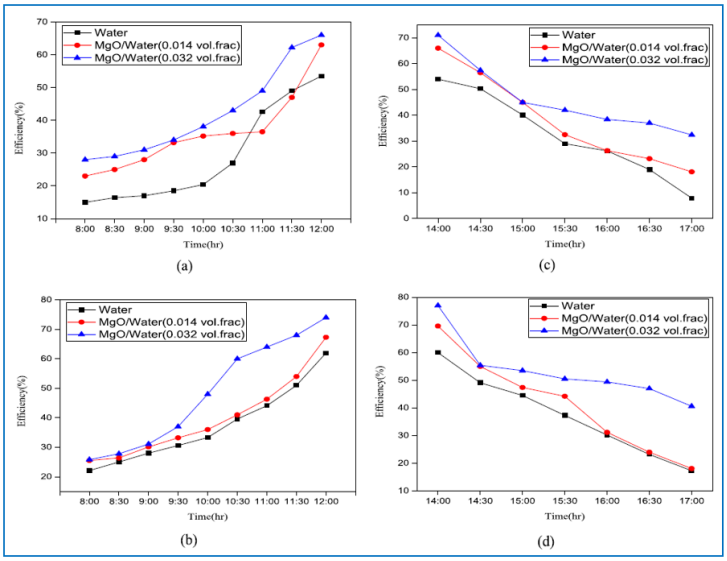

Fig. 83. Comparison of efficiency versus time bewteen water and MgO water fluid at different flow rates: (a) 5 litre/min; (b) 11 litre/min; (c) 8 litre/min; (d) 14 litre/min [90]

3.6 PV/T with cerium-oxide nanofluid

Sharafeldin and Gróf [91] implemented an experimental study of a PV/T system with CeO_2/water nanofluids, and assessed the system thermal efficiency under three concentrations of CeO_2 nanoparticle (0.035%, 0.025% and 0.015%) and three different mass flux rates (0.017 kg/s·m^2, 0.015 kg/s ·m^2 and 0.013 kg/s·m^2). According to Fig. 84 (a), the maximum system thermal efficiency for all studied cases is 0.7433 when the mass flux rate and volume fraction are 0.017 kg/s·m^2 and 0.035%, respectively, by comparison, the minimum value is 0.522 when the mass flux rate is 0.013 kg/s.m^2 at the same concentration. This indicates that the higher mass flux rate, the greater system thermal efficiency. Moreover, results conclude from Fig. 84 (b) that the thermal loss coefficient is enhanced when the nanoparticles are added.

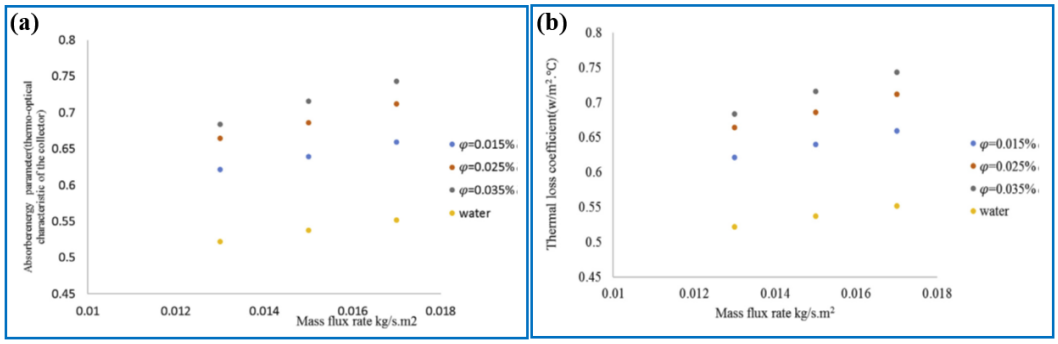

Fig. 84. Variation of CeO_2 mass flux rate vs: (a) parameter; (b) thermal loss coefficient [91]

3.7 PV/T with tungsten-oxide nanofluid

Sharafeldin and Gróf [92] investigated the thermal efficiency of a PV/T system with the diameter of 90 nm Tungsten-oxide nanoparticle (WO_3) based on various volume fractions. Their calculation process is given in Table 9. The WO_3/water nanofluid is prepared by using the 'two-step' method [63]. Their results illustrated from Fig. 85 that the temperature difference of the working fluid raises by 21% with the addition of WO_3 nanoparticles. The maximum heat obtained at the solar irradiance of 900 W/m^2 is increased by 23% when the WO_3 nanoparticles are adopted in the system. Furthermore, results observed from Fig. 86 that the system thermal efficiency is 72.83%, having an average increasing of 19.3% in comparison with that using pure water.

Table 9 The mathematical equations of the WO_3 properties [92]

Description	Equations
The WO_3 density	$\rho_{nf} = \rho_{np}(\varphi) + \rho_{bf}(1-\varphi)$
The WO_3 heat capacity	$(\rho C_p)_{nf} = (\rho C_p)_{np}(\varphi) + (\rho C_{bf})_{bf}(1-\varphi)$
The WO_3 thermal conductivity	$k_{nf} = k_{bf}\dfrac{[k_{np} + (n-1)k_{bf} - (n-1)\varphi(k_{bf} - k_{np})}{[k_{np} + (n-1)k_{bf} + \varphi(k_{bf} - k_{np})]}$

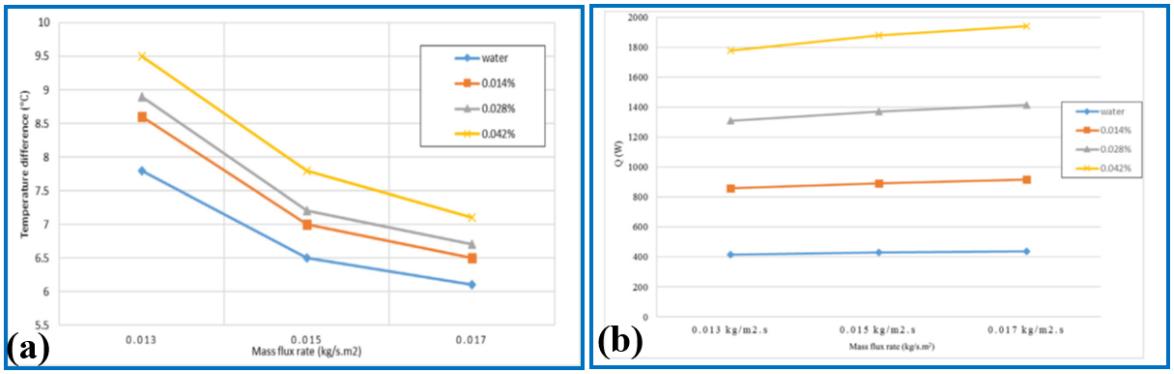

Fig. 85. Experimental results of WO_3/water at different mass flux rates: (a) temperature difference; (b) the maximum heat obtained [92]

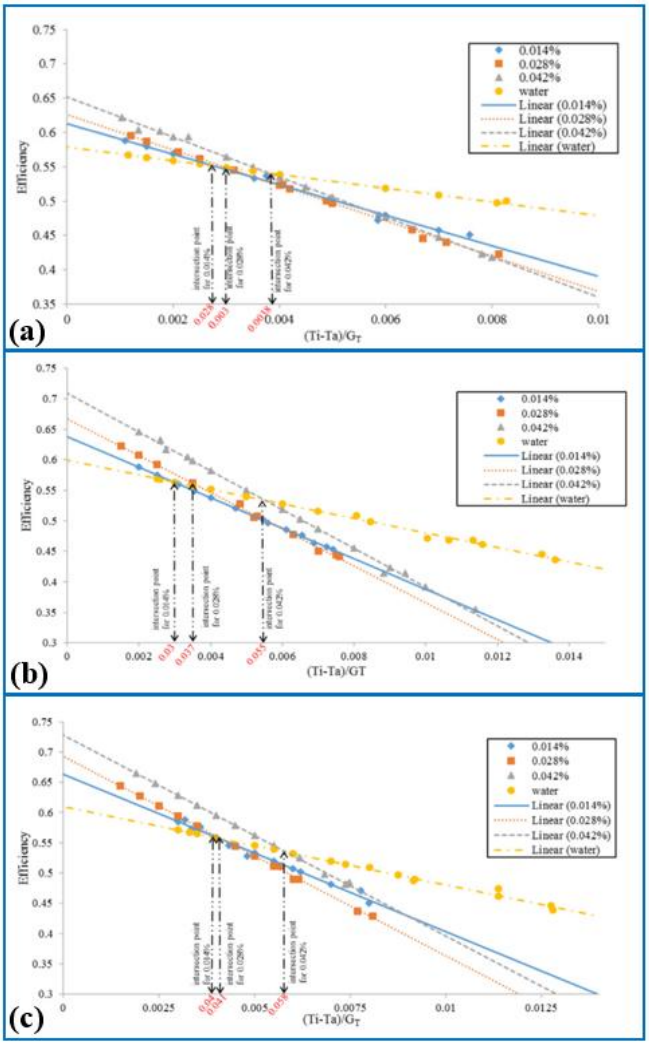

Fig. 86. Thermal efficiency for different WO_3 nanofluid concentration for different mass flux rates: (a) 0.013 kg/s ·m^2; (b) 0.015 kg/s·m^2; (c) 0.017 kg/s·m^2 [92]

3.8 PV/T with titanium-oxide nanofluid

Ebaid et al. [93] analysed experimentally the cooling influence of a PV module with Titanium-oxide (TiO_2/water) nanofluid at various mass flow rates ranging between 500 and 5000 ml/min. Their results reveal from Fig. 87 that the system electricity energy output with TiO_2 nanofluid and pure water are increased individually by 6.05% and 3.75% compared with without cooling case. This indicates that the enhancement contributes to decreasing the surface temperature of the PV module and improving the power output. Additionally, according to Fig. 88, the mean electrical efficiencies of the PV module with TiO_2 nanofluid and water are improved individually 0.82% and 0.48% in comparison to that without cooling effect.

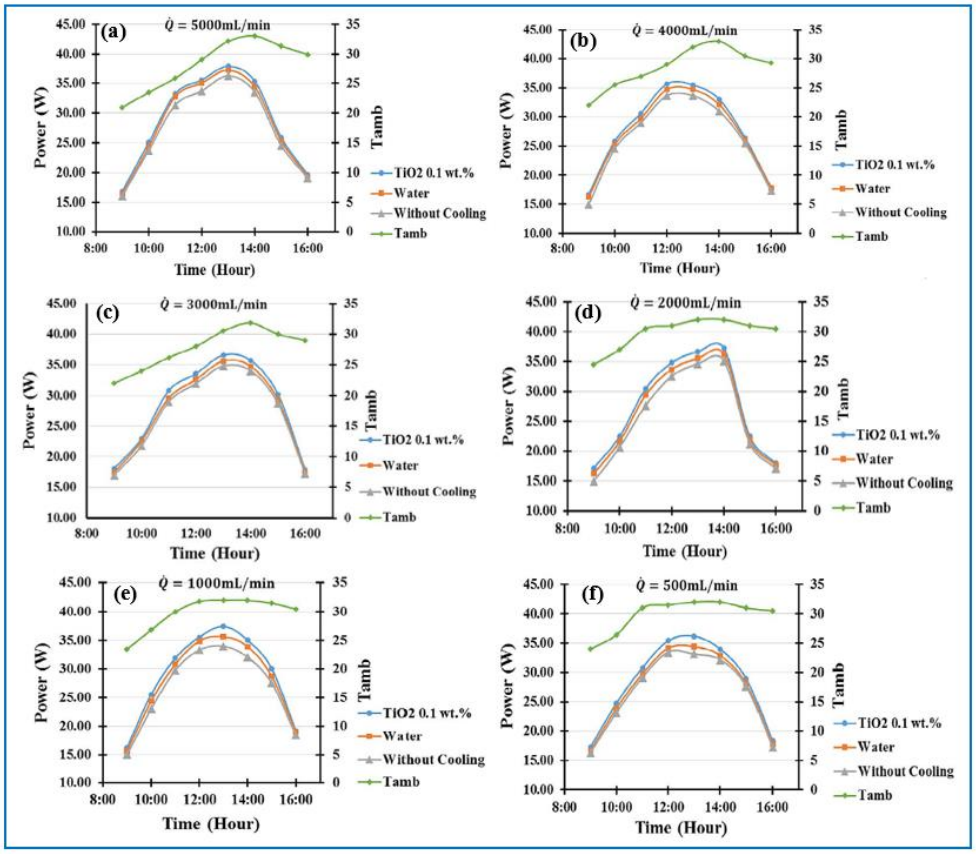

Fig. 87. PV electrical energy output based on TiO_2 at different flow rates [93]

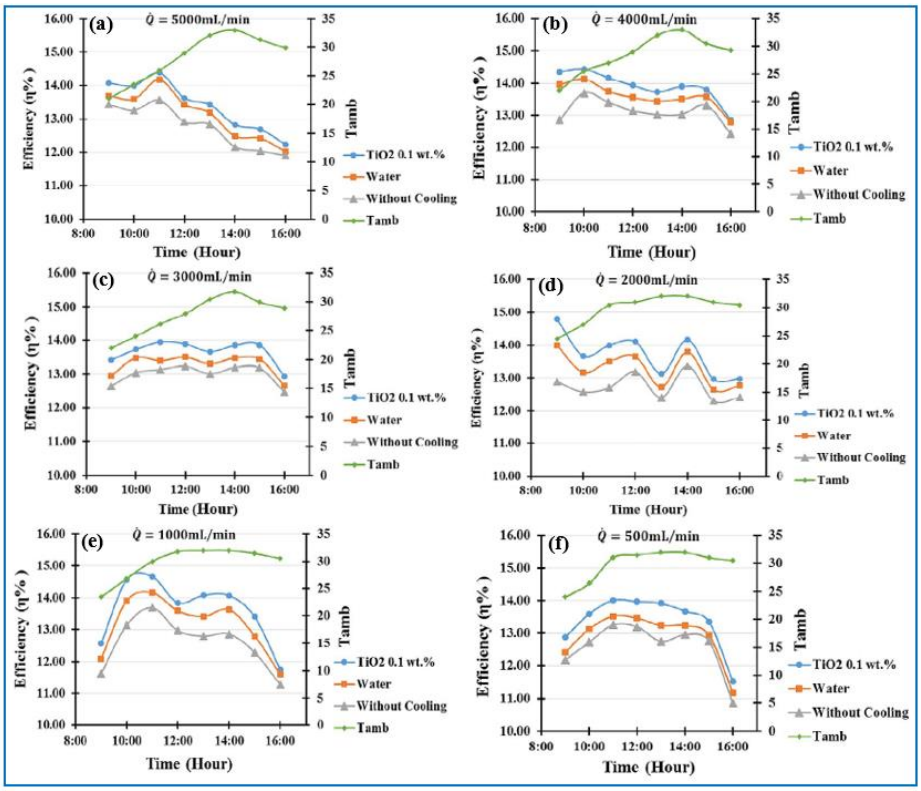

Fig. 88. PV electrical efficiency based on TiO_2 at different flow rates [93]

3.9 PV/T with zirconia nanofluid

Sarafraz et al. [55] compounded a hybrid zirconia-acetone (ZrO_2-C_3H_6O) nanofluid employed as a working fluid within a thermosiphon heat pipe system to analyze the influences of the ZrO_2-C_3H_6O nanofluid on the heat transfer coefficient and thermal resistance. The XRD, SEM and TEM photos of ZrO_2 nanoparticle with the average size of the 20 nm are presented in Fig. 89. It can be found from Fig. 90 that the ZrO_2-C_3H_6O nanofluid could decrease the thermal resistance and improve heat transfer coefficient of the evaporator section.

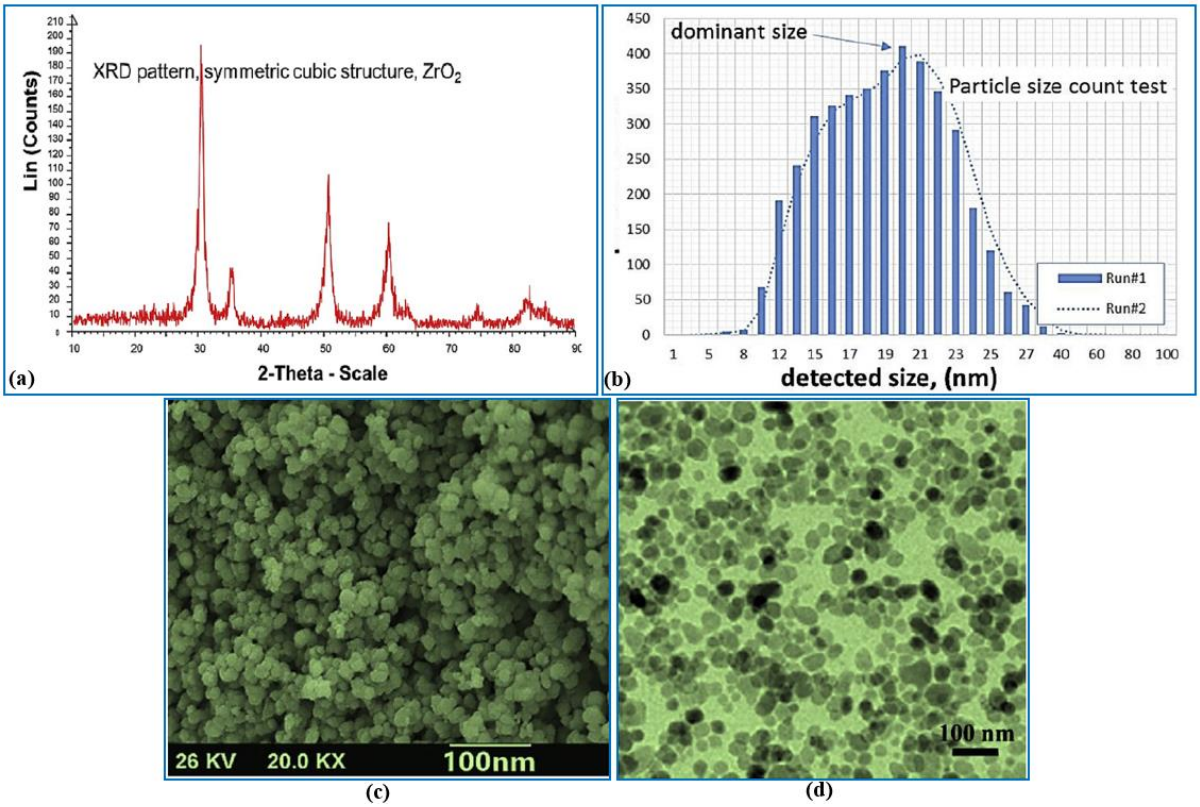

Fig. 89. Schematic diagram of properties and structural of the ZrO_2 nanofluid [55]

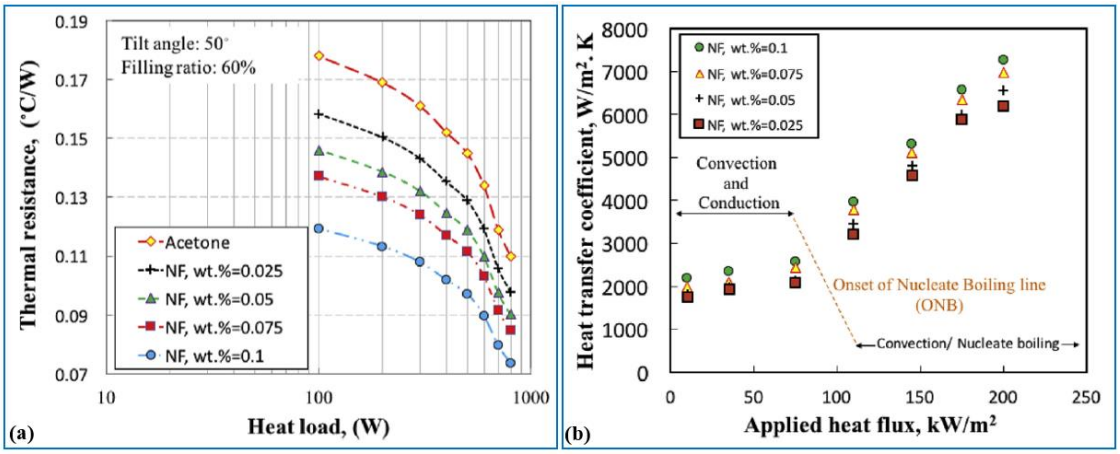

Fig. 90. Experimental analysis at different ZrO_2 nanofluid concentrations: (a) thermal resistance; (b) heat transfer coefficient [55]

3.10 PV/T with graphene nanofluid

Sarafraz and Safaei [94] investigated experimentally an evacuated tube solar collector with heat pipe using the graphene nanofluid as a working fluid. As shown in Fig. 91, the XRD and SEM photos present that the average length of the graphene nanoparticle is 123-424 nm with the thickness of 1.5-3 nm. Their results demonstrate from Fig. 92 that the system thermal efficiency rises with the mass concentrations of the graphene nanofluid, and the thermal efficiency reaches the maximum value of 0.95 at 0.1wt.%.

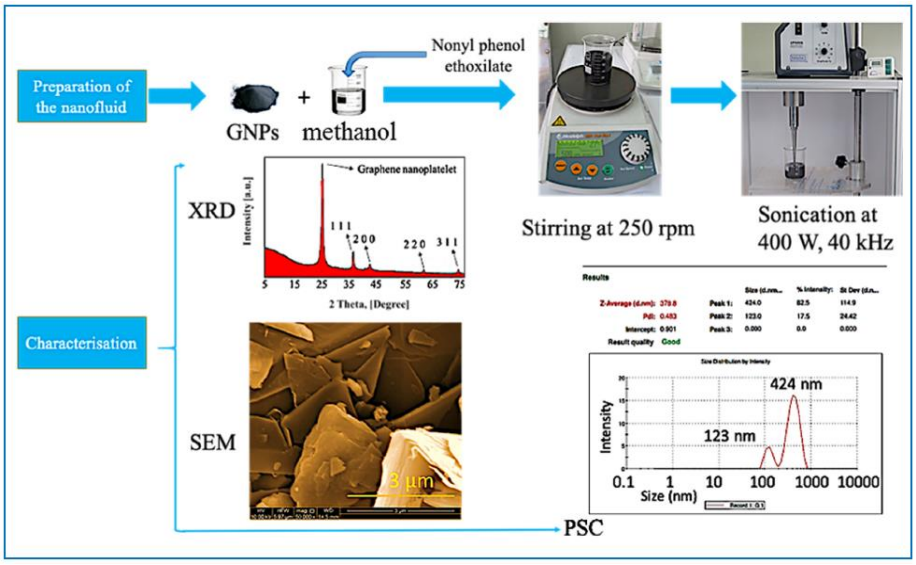

Fig. 91. XRD and SEM photos of the graphene nanofluid [94]

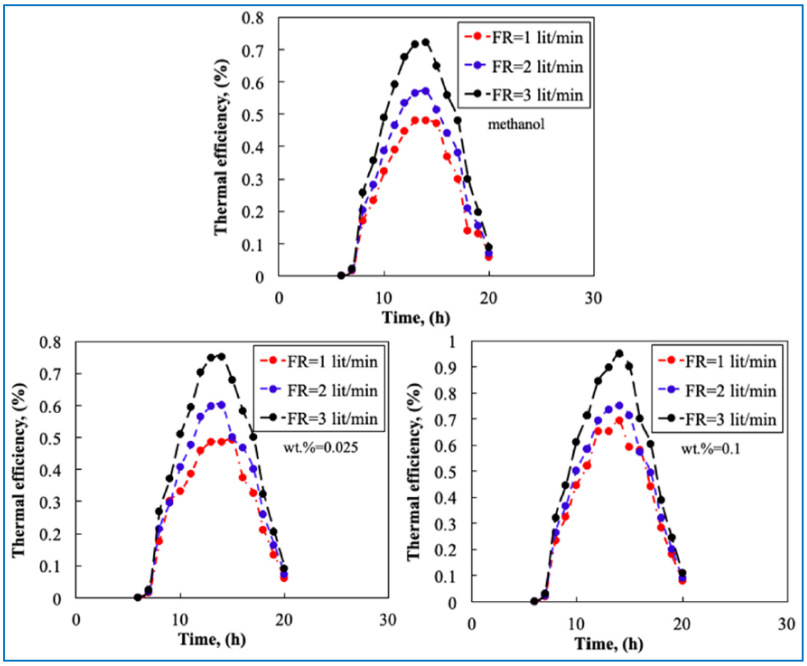

Fig. 92. System thermal efficiency at various concentrations: (a) methanol; (b) graphene nanofluid at 0.025 wt.%; (c) graphene nanofluid at 0.1 wt.% [94]

Later, Sarafraz et al. [95] performed a testing study to evaluate the influences of the filling ratio and installation angle on the heat transfer coefficient (HTC) of graphene nanofluid within a heat pipe. It can be demonstrated from Fig. 93 that the HTC could reach the maximum value when the optimum filling ratio and installation angle are 0.55 and 65°, respectively.

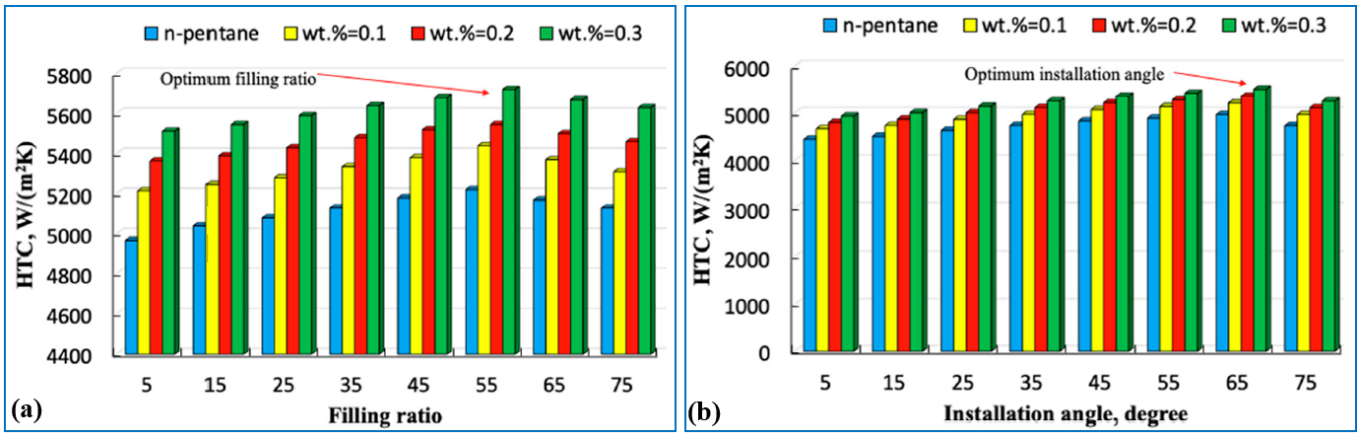

Fig. 93. Experimental results of HTC: (a) filling ratio; (b) installation angle [95]

3.11 PV/T with carbon nanofluid

Sarafraz et al. [96] performed a testing analysis of a solar collector system by using a novel mixture of carbon-acetone nanofluid. The images of XRD, SEM and TEM are shown in Fig. 94. It can be confirmed from Fig. 95 that the maximum thermal efficiency is about 70% for the pure acetone, while the carbon-acetone nanofluid has an enhancement in the thermal efficiency which could achieve about 90% for 0.025 and 0.1 wt.% because of the Brownian motion of the carbon nanoparticles within the heat pipes.

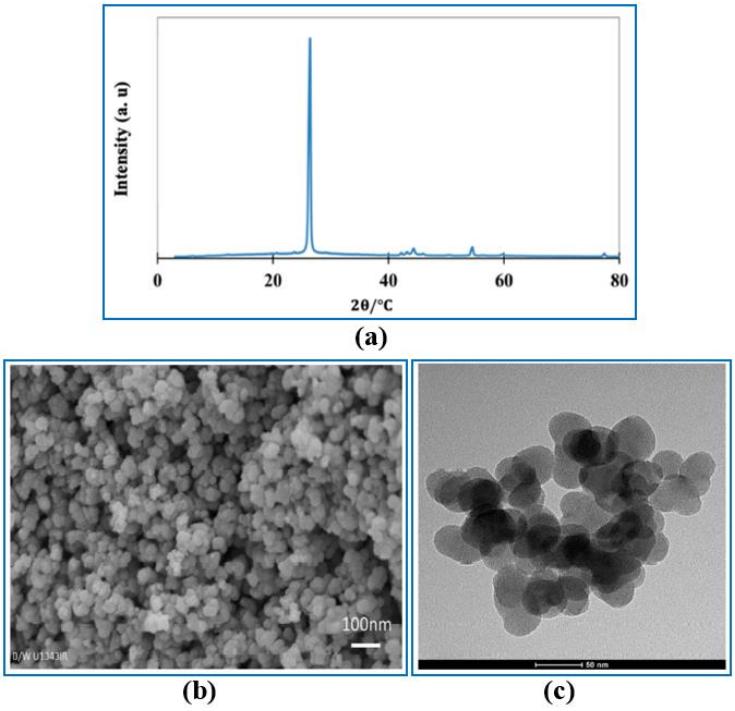

Fig. 94. Images of carbon nanoparticles: (a) XRD; (b) SEM; (c) TEM [96]

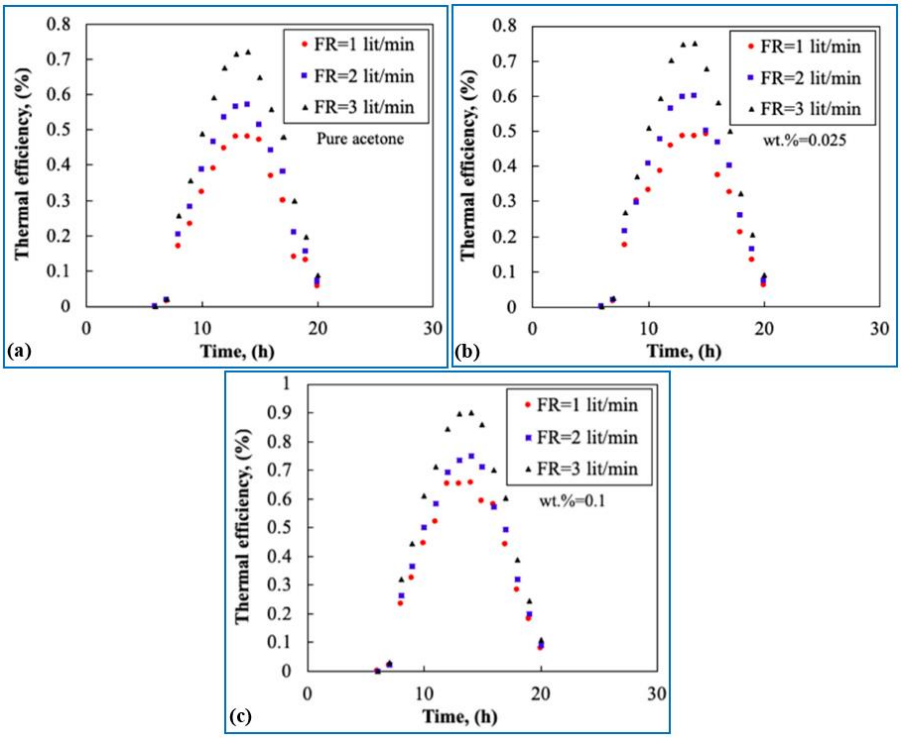

Fig. 95. Thermal efficiency at different mass fractions of carbon nano-powder/Acetone: (a) pure acetone; (b) wt.% =0.025; (c) wt.% =0.1 [96]

3.12 Comparison of different PV/T with nanofluids

The working fluid of PV/T system has been summarized based on various nanofluids. To assess the system performance, some comparison analyses are illustrated. For example, Sarafraz et al. [56] demonstrated that the nano-suspensions are able to improve the efficiencies of the CPV electricity modules, and the thermal conductivity of the water is improved by 24% due to the presence of alumina nanoparticles. Tong et al. [82] investigated the system thermal efficiency through using water, Al_2O_3 and CuO nanofluids as the refrigerant, and found from Fig. 96 (a) that the maximum efficiency could reach 63.6%, 77.5% and 73.9%, respectively. This indicates that the heat obtained with the Al_2O_3 nanofluid is higher in comparison with that of the CuO nanofluid whereas the heat loss with the Al_2O_3 nanofluid is lower compared with that of the CuO nanofluid. Consequently, when the Al_2O_3 nanofluid is utilized as the refrigerant within the system, the heat performance is comparatively high. Furthermore, as illustrated in Fig. 96 (b), when 20 nm 1.0 vol. % Al_2O_3 and 40 nm 0.5 vol. % CuO nanofluids are employed, the improvements of the system efficiencies are individually 3.4% and 3.7%. By comparison, when pure water is adopted, the improvement of the system efficiency is about 2.6% that is the lowest.

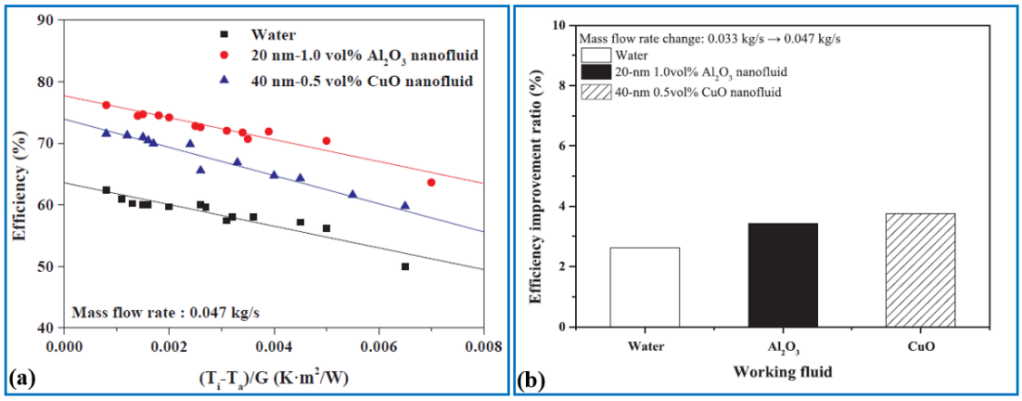

Fig. 96. Results comparison: (a) efficiency; (b) efficiency improvement ratio [82]

Sardarabadi et al. [97] compared the influences of using Al_2O_3/water, ZnO/water and Titanium-oxide (TiO_2)/water nanofluids as a coolant on a PV/T system by experimental testing. TEM photos of the ZnO, Al_2O_3 and TiO_2 nanoparticles are presented in Fig. 97. These sizes and properties of metal-oxides are shown in Table 10.

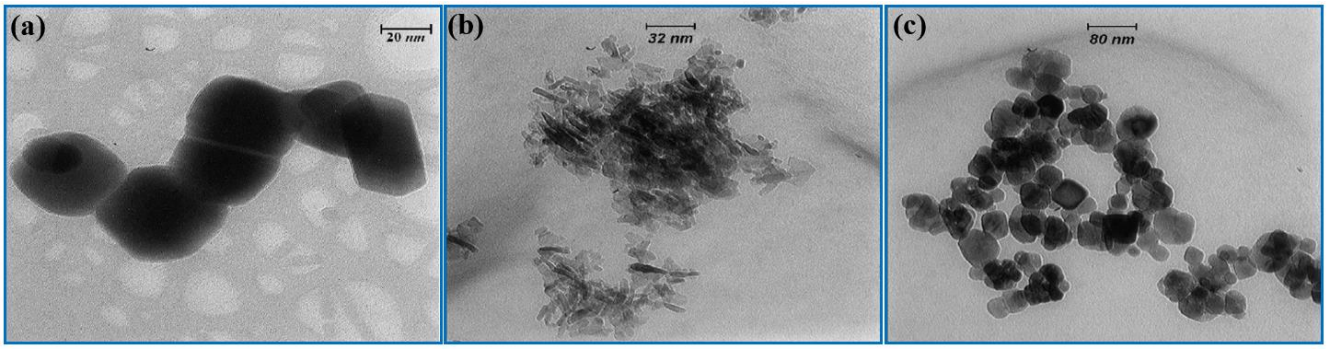

Fig. 97. TEM images of the nanoparticles: (a) ZnO; (b) Al_2O_3; (c) TiO_2 [97]

Table 10 The metal-oxides properties [97]

Metal-oxides	Size (nm)	Density (kg/m^3)	Heat capacity (J/kg·K)	Thermal conductivity (W/m·K)
ZnO	35-45	5600	495	13
Al_2O_3	10-30	3970	765	40
TiO_2	20-60	4250	686	8.9

According to Fig. 98 (a), compared to the traditional PV/T system with water, the PV/T systems with ZnO, Al_2O_3 and TiO_2 can increase the thermal output by 34.31%, 8.12% and 31.01%, respectively. However, compared with the conventional PV system, the electrical productions are improved by 6.73%, 5.50%, 6.99% and 5.33% for the cases of ZnO, Al_2O_3, TiO_2 and water. This indicates that the highest electrical output improvement is presented for the PV/T system with TiO_2 whereas the PV/T system with ZnO displays the highest thermal output improvement. According to Fig. 98 (b), the PV/T systems with TiO_2 and ZnO have the better performance in comparison to other systems with thermal and power efficiencies of 59.64% and 57.97%, respectively.

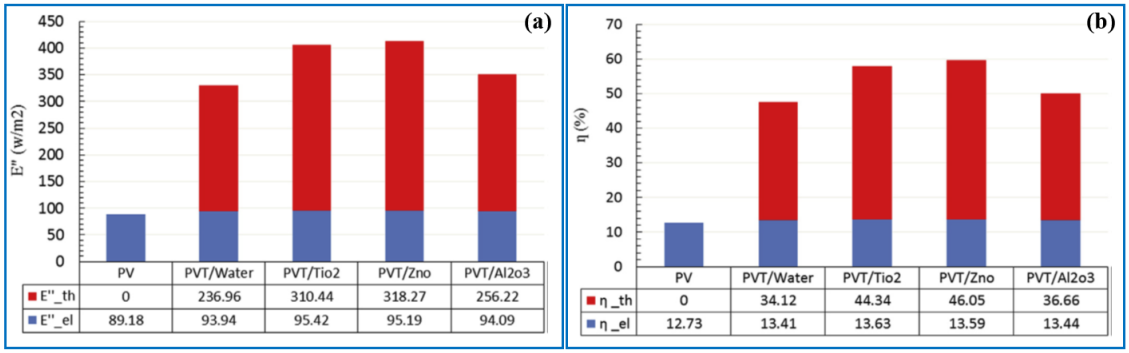

Fig. 98. The schematic diagram of mean thermal and electrical: (a) output; (b) efficiencies [97]

Eidan et al. [98] performed a testing of a PV/T system to analyse the impacts of Al_2O_3 and CuO nanofluids on the system thermal performance for two concentrations (0.25 and 0.5 vol. %.) and mass flow rates (1 and 2 litre/hour). It can be found from Fig. 99 that the efficiency gradually grows with the mass flow rate. What is more, these results reveal that the system efficiencies for both Al_2O_3 and CuO nanofluids at a higher volumetric concentration (0.5 vol. %) are superior to that with the lower concentration (0.25%).

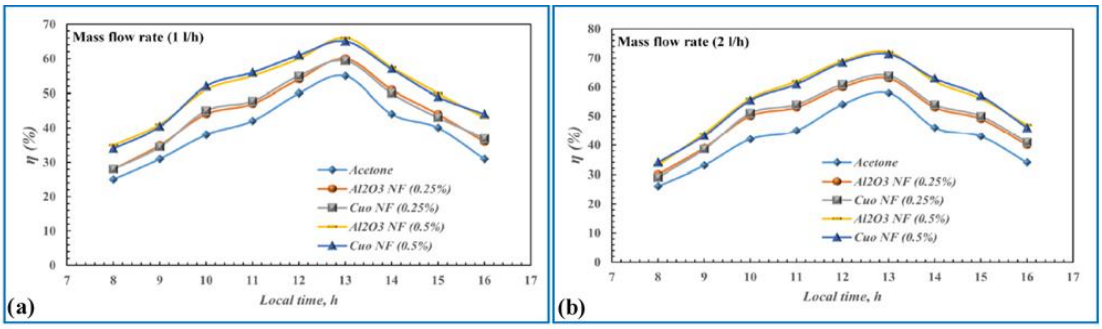

Fig. 99. Results comparison at different mass flow rates: (a) 1 litre/hour; (b) 2 litre/hour [98]

Mercan and Yurddaş [99] investigated the effects of Al_2O_3 and CuO nanofluids with 5 vol. % concentration on outlet temperature for 24 tubes collector. Their results conclude from Fig. 100 that the outlet temperature for Al_2O_3 nanofluid can be increased by 4.13% whereas the one for CuO nanofluid in the same conditions is raised by 6.80%. This means that the best enhancement is obtained with CuO nanofluid.

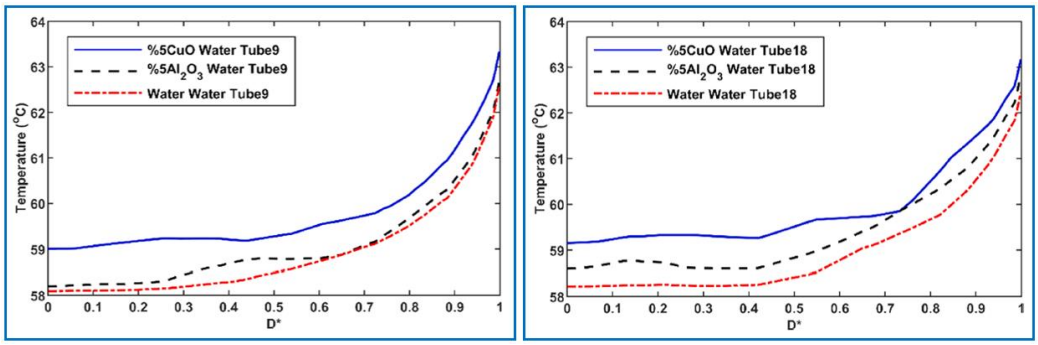

Fig. 100. Temperature variation for Al_2O_3 and CuO nanofluids with 5 vol. % concentration [99]

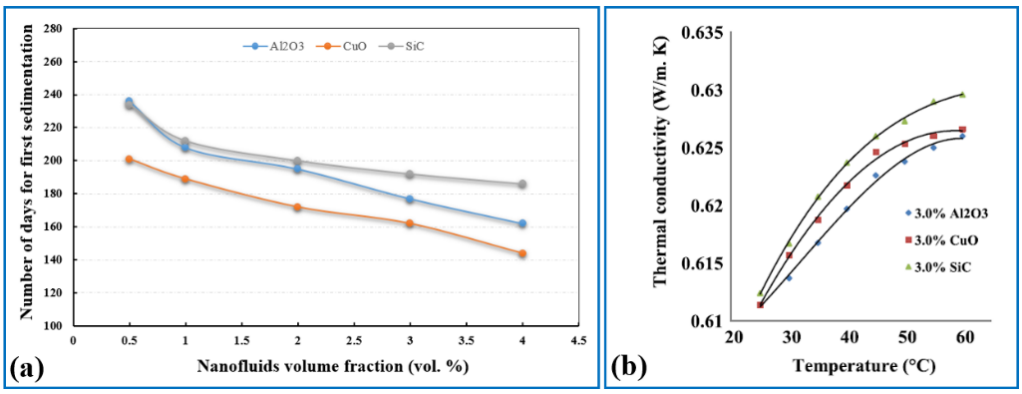

Fig. 101. Comparative results: (a) stability; (b) thermal conductivity [100]

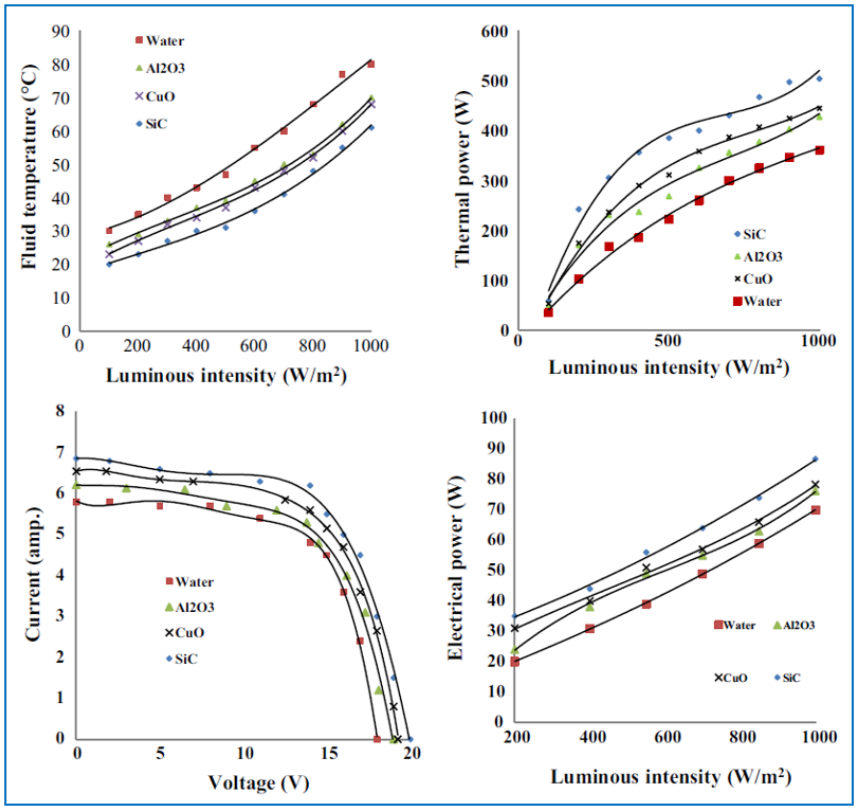

Fig. 102. Effects of different nanofluids on fluid temperature and system performance [100]

Al-Waeli et al. [100] carried out a comparative analysis to determine which nanofluid is more suitable for the PV/T system. It can be found from Fig. 101 that SiC nanofluid has greater stability and thermal conductivity than the Al_2O_3 and CuO nanofluids, meanwhile, the lower the volume concentration, the higher the stability of the nanofluids. Moreover, it can be seen from Fig. 102 that SiC nanofluid is able to decrease the fluid temperature within the absorber and enhance the system efficiency in comparison with other two nanofluids. What is more, thermal physical properties of different nanoparticles utilized in PV/T system and major effects are generalized in Table 11.

Table 11 Comparison of nanoparticles associated with the thermal properties and key findings

Nanoparticle type	Researcher	Base fluid	Particle size (nm)	Temperature (°C)	Volume fraction (vol. %)	Mass flux rate ($kg/s \cdot m^2$)	Mass flow rate (L/min)	Key findings
Al_2O_3	Ghaderian and Sidik [81]	Distilled water	40	30	0.03 and 0.06	N/A	0.33, 0.67 and 1.0	• The maximum thermal efficiency achieves 58.65% when the concentration reaches 0.06 vol.%. • Result confirmed that Al_2O_3 nanofluid contributes to enhancing the heat transfer rate and system performance.
	Tong et al. [82]	Water	20	30	0.5,1 and1.5	0.047	N/A	• The highest efficiency could achieve 77.5% when the 1.0 % concentration of Al_2O_3 nanofluid is adopted, which is 21.9% higher compared to water. • The system exergy efficiency based- 1.0 vol.% Al_2O_3 nanofluid is improved by 56.9% compared to water.
	Sardarabadi et al. [97]	Water	32	30	0.2	N/A	0.67	• The thermal output of the PV/T based-Al_2O_3 could enhance 8.12% in comparison with that of the PVT/water. • The electrical output of the PV/T based-Al_2O_3 could improve 5.5% compared with conventional PV array. • Using Al_2O_3 nanofluid as working fluidcontributes to decreasing the system exergy loss and entropy production.
	Eidan et al. [98]	Acetone	20	30	0.25 and 0.5	N/A	0.017 and 0.033	• The system thermal efficiency based-Al_2O_3 could enhance 18% and 30% for different concentrations of 0.25% and 0.5%, respectively. • Higher concentration (0.5%) Al_2O_3 nanlofluid provides a greater performance in comparison with the lower concentration one (0.25%).
	Mercan and Yurddaş [99]	Water	30	30, 45 and 60	1, 3 and 5	0.025, 0.05 and 0.07	N/A	• The heat transfer rate improves when the nanoparticles ratio grows. • The system thermal output based-Al_2O_3 increased by 4.13% for the 24-tube collector.
	Al-Waeli et al. [100]	Water	30-60	25	0.5, 1, 2, 3 and 4	N/A	N/A	• The Al_2O_3 nanofluid has more stability than CuO nanofluid.
CuO	Tong et al. [82]	Water	40	30	0.1, 0.3, 0.5 and 0.7	0.047	N/A	• The CuO nanofluid could achieve the maximum efficiency of 73.9%, which is 16.2% higher than water. • The system exergy efficiency based- 0.5 vol. % CuO nanofluid is enhanced by 49.6% compared to water.
	Ghaderian J et al. [83]	Distilled water	30-50	40	0.03 and 0.06	N/A	0.33 and 1.0	• The mean outlet fluid tempertaure could be increased by 14% for 0.03 vol. % concentration of CuO nanofluids in comparison with water. • The system performance is individually improved by 51.4% and 41.9% for 0.06 vol. % and 0.03. vol. % concentrations.
	Qu et al. [84]	Water	200-1350	30	0.25, 0.15, 0.05, 0.025 and 0.01	N/A	N/A	• The outlet temperature is improved by 9.2 °C in comparison with water when the concentration of 0.25 vol. %, CuO nanofluid is adopted in the system.
	Eidan et al. [98]	Acetone	25	30	0.25 and 0.5	N/A	0.017 and 0.033	• The system thermal efficiency based-CuO could enhance 16.7% and 28% for different concentrations of 0.25% and 0.5%, respectively.

								• Higher concentration (0.5%) CuO nanlofluid could provide a greater performance in comparison with the lower concentration one (0.25%).
	Mercan and Yurddaş [99]	Water	30	30, 45 and 60	1, 3 and 5	0.025, 0.05 and 0.07	N/A	• The heat transfer rate improves when the nanoparticles ratio grows. • The thermal output of the PV/T based-CuO nanlofluid could increase by 6.8% for the 24-tube collector.
	Al-Waeli et al. [100]	De-ionized Water	35-45	25	0.5, 1, 2, 3 and 4	N/A	N/A	• The CuO has greater thermal conductivity than Al_2O_3.
CuO-MWCNT	Qu et al. [84]	Water	200-1350	60-80	0.0015	N/A	N/A	• The maximum temperature could be improved by 14.1 °C when the hybrid CuO-MWCNT nanofluids is adopted. • Results indicated that the hybrid CuO-MWCNT nanofluids is a potential method to boost the system efficiency.
SiC	Al-Waeli et al. [85]	Water	40-60	20	1, 1.5, 2, 3 and 4	N/A	40.11	• The power efficiency of SiC nanofluid could enhance by 24.1% in comparison with conventional PV array. • The system heat efficiency of SiC nanofluid could improve by 100.19%. • The overall system effectiveness based SiC nanofluid has a greater efficiency of around 88.9% than the separate PV panel.
	Al-Waeli et al. [100]	Water	45-65	25	0.5, 1, 2, 3 and 4	N/A	N/A	• Results found that the SiC has the highest thermal conductivity and the best stability in comparison with CuO and Al_2O_3. • SiC nanofluid could enhance the system performance more than the CuO and Al_2O_3.
Ag	Aberoumand et al. [88]	Water	50	40 and 80	2 and 4	0.034, 0.064 and 0.116	N/A	• The electricity output and efficiency based-Ag nanofluid at the concentration of 4 vol. % have an improvement ranging from 8% to 10% and 14%, respectively, compared to water. • The exergy efficiency of the system based-Ag nanofluid has a 50% enhancement in comparison with pure water.
Ag-CoSO4	Han et al. [89]	Water/Ag	29-65	10	0.4	N/A	N/A	• Ag/$CoSO_4$ nanofluid could generate higher UV absorption and visible wavelengths compared to water.
MgO	Dehaj and Mohiabadi [90]	Deionized water	30	25	0.014 and 0.032	N/A	5, 8, 11 and 14	• The system efficiency with MgO nanofluid is higher compared with ones with water. • System performance improves with the growth in the concentration of the nanofluid.
CeO_2	Sharafeldin and Gróf [91]	Water	25	30	0.015, 0.025 and 0.035	0.013, 0.015 and 0.017	N/A	• The higher concentration of CeO_2 nanofluid could give higher temperature difference. • The maximum growth of heat obtained is higher by 42.3% compared with water. • The growth of the concentration of CeO_2 could boost the outlet temperature and system efficiency, however it also adds the coefficient of thermal loss. • The system best performance is found when the 0.025 vol % concentration is adopted.
WO_3	Sharafeldin and Gróf [92]	Water	90	30	0.014, 0.028 and 0.042	0.013, 0.015 and 0.017	N/A	• The system thermal-optical efficiency could achieve 72.83% and increase by 19.3% in comparison with water. • The maximum heat obtained is improved by 23% when the WO_3 nanoparticles is added in the system.

Ti_2O_3	Ebaid et al. [93]	Deionized water	80	20-60	0.2	N/A	0.5-5	• The overall PV/T system exergy efficiencies for the ZnO, Al_2O_3, TiO_2 and water are individually increased by15.45%, 18.27%, 15.93% and 12.34%. • Results revealed that Ti_2O_3 nanofluids could decrease the exergy loss and entropy production because of their heat transfer improvement in PV/T system.
	Sardarabadi et al. [97]	Water	30	30	0.01, 0.05 and 0.1	0.002, 0.012 and 0.0024	N/A	• Al_2O_3 nanofluid has a better performance compared with TiO_2 nanofluid. • In terms of electrical output and efficiency, TiO_2 nanofluid gives better performance in comparison with Al_2O_3 nanofluid.
ZrO_2	Sarafraz et al. [55]	Acetone	20	10-90	0.025, 0.05, 0.075 and 0.1	N/A	N/A	• The ZrO_2-C_3H_6O nanofluid could decrease the thermal resistance. • The ZrO_2-C_3H_6O nanofluid could improve the heat transfer coefficient of the evaporator section.
Graphene	Sarafraz and Safaei [94]	Methanol	123-424	5-75	0.025, 0.05, 0.075 and 0.1	N/A	3	• The thermal efficiency reaches the maximum value of 0.95 at 0.1wt.%. • The system thermal efficiency increases with the mass concentrations of the graphene nanofluid.
Carbon	Sarafraz et al. [96]	Acetone	50	3-80	0.025, 0.05, 0.075 and 0.1	N/A	1, 2 and 3	• The maximum thermal efficiency is about 70% for the pure acetone, while the carbon-acetone nanofluid has an enhancement in the thermal efficiency which could achieve about 90% for 0.025 wt.% and 0.1 wt.%.

4. Solar cells

4.1 Structure and manufacturing of current and next generation solar cells

Solar PV technology has developed steadily since it was first proposed by Bell Labs in 1954 [101], and could readily combined with other energy technologies, meanwhile, the price of panel has reduced by 80% since 2009 [102]. At present, PV technology is classified into the Si-wafer technology (the first generation), thin-film technology (the second generation) and multi-junction technology (the third generation) [103]. Additionally, many PV cell materials have been developed and be applied for electrical production, such as Si-wafer (Mono- and poly-crystalline silicon), thin-film silicon (Cadmium telluride (CdTe), copper indium gallium selenide (CIGS), Gallium arsenide (GaAs) and amorphous silicon (a-Si)) as well as multi-junction (gallium indium phosphide (GaInP), indium gallium arsenide (InGaAs) and germanium (Ge)) [103, 104]. To be more specific, the first generation of solar cell technology utilized silicon as the semiconductor for producing p-type and n-type layers, however it has the demerits of low efficiency and high cost. To overcome the drawback, the thin-film solar cells are developed and fabricated to produce power energy and decrease current losses. Compared to the traditional silicon semiconductor solar cell, the thin-film solar cells have only a few micro-meter layer thickness and more flexible installation. And also, it uses less material and lower cost for manufacturing processes that are relied on various of chemical substances involving the a-Si, CIGS, CdTe and GaAs. Compare with the first and second generations of solar cells, the third generation (multi-junction technology) is the introduction of nanotechnology and organic materials into the manufacturing process, but it is still in the research and development (R&D) phase and yet to be commercially applied [105]. There are currently five types of organic or polymer (OPV); dye-sensitized (DSSC), copper zinc tin sulphide solar cell (CZTS), quantum dot solar cell and perovskite solar cell [106-108]. Comparison between various types of solar cells is represented in Table 12.

To sum up, the development of solar cells has led to a huge enhancement on the electrical efficiency during these decades and there is a steady reduction in the environmental carbon footprint. Lots of the next generation solar cells depend on nanomaterials but they contain toxic heavy metals like lead and cadmium that are harmful to environment change and human health. Accordingly, the cleaner manufacturing processes, better regulatory regimes for nanomaterials, a fuller understanding of the toxic footprints and more solar PV recycling technology should be investigated in the future work.

Table 12 The comparison of various types of solar cells

Item	**The first generation PV (Si-wafer technology)**		**The second generation PV (thin-film technology)**				**The third generation PV (multi-junction technology)**				
Technology	Single Crystalline Silicon (c-Si)	Polycrystalline Silicon (p-Si)	Copper Indium Gallium Di-Selenide (CIS/CIGS)	Amorphous Silicon (a-Si)	Gallium Arsenide (GaAs)	Cadmium Telluride Cells (CdTe)	Dye-sensitized (DSSC)	Organic or Polymer (OPV)	Copper zinc tin sulphide solar cell (CZTS)	Perovskite solar cell	Quantum dot solar cell
Semiconductor materials	c-Si or p-Si		CdTe, a-Si, CIGS or GaAs				GaInP, InGaAs or Ge				
Commercial production mature	Large-scale	Large-scale	Medium-scale	Small-scale	Small-scale	Large-scale	R&D	R&D	R&D	R&D	R&D
PV module efficiency	14-19%	13-16%	7-11%	7-9%	25%-30%	6%-8%	25-30%	10%-11%	30% - 33%	6%-8%	19%-23%
Maximum PV module efficiency	25%	20.4%	19.8%	12.2%	30%	10.6%	40%	11%	42%	16.5%	26.7%
Maximum PV module output power	320W	N/A	120W	300W	300W	120W	120W	N/A	N/A	N/A	N/A

4.2 Micro-thermometry analysis of solar cells

To assess the electrical reduction of the PV panel caused by its temperature rise, accurate operational temperature measurements are essential. Typically, temperature measurement should be implemented at the actual semiconductor junctions, however, it is usually measured at the backside surface of the PV module which inevitably results in a small error because of temperature difference between backside surface and semiconductor [109]. The traditional approaches for temperature measurement of PV panel in the laboratory or outdoors are depended on the contact temperature sensors including scanning thermal probes, resistance thermometry and micro-thermocouples for point measurements whereas the noncontact-based thermometry includes infrared thermometry, liquid crystal thermometry and optical thermometry which are usually employed for larger region imaging of PV panels [110, 111]. Specifically, Lopez-Garcia et al. [112] analysed the temperature coefficients for the bifacial c-Si PV modules under natural sunlight and simulated indoor conditions based on the micro-thermocouples method, and revealed that the temperature coefficients mainly depend on the cell technology rather than on measurement condition. Meanwhile, the PV bifacial modules present a lower temperature coefficient compared with the standard c-Si modules. Buerhop et al. [113] used the infrared thermography method to get the operational temperature of the PV cells, and revealed that the temperature variation of normal PV cells could reach the maximum value of 45.1 ℃ whereas a specific damaged cell is about 62.1 ℃. Additionally, the resistance thermometry is one of the most widely utilized methods to monitor temperature change at the microscale. Sadat et al. [114] performed an experimentally and theoretically study on nanoscale heat transport based on the resistance thermometry, and presented that it is readily to solve temperature variation with a resolution of approximately 20–100 μK when the heating frequencies is in the range of 0.5 Hz to 20 Hz.

4.3 Recycling process and cost of PV panels waste

By 2016, the volume of solar PV waste is in the range between 43,000 and 250,000 tonnes around the world. This means that the number of solar PV panels reaching their end-of-life (EOL) stage will rise steadily due to the increasing in installations [115]. It is reported that the solar PV waste will accomplish about 4%-14% of whole energy production capacity by 2030 and increase over 80% by 2050 [116, 117]. At present, US, Europe and Japan have concentrated on research and development associated with recycling of PV panels waste [108-120]. There are currently two main categories of solar panels including silicon and thin-film based that could be recycled by using physical separation, thermal and chemical treatment approaches [117, 121] as described in Fig. 103.

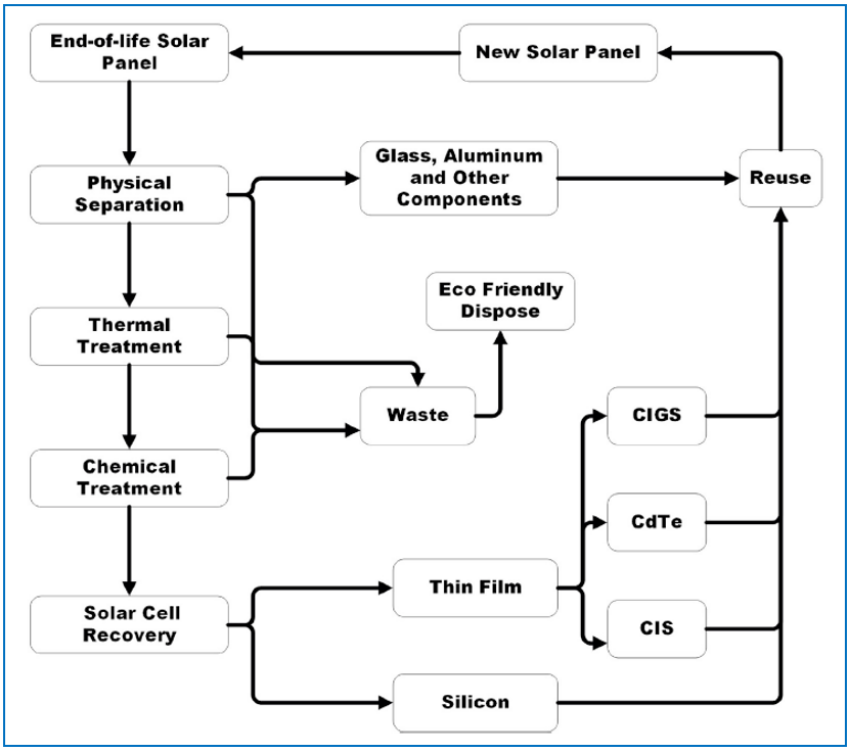

Fig. 103. Different types of solar PV recycling processes [117]

To be more specific, the physical separation process is mainly utilized to check and repair the PV panel, cables and junction-box faults [117, 122]. This contributes to improving the power production of the older PV panel, but this approach could only be employed for exterior junction boxes which is placed external the main body of the PV array. By comparison, for the thermal and chemical treatments, Doi et al. [120] dissolved the crystalline-silicon PV panel for removing the EVA layer by various organic solvents, and concluded that it is the most effective solution when the trichloroethylene temperature could reach 80 °C. Fiandra et al. [123] utilized the thermal treatment approach to recover the polycrystalline silicon, and found that the reactor could be heated to the maximum temperature of 500 °C when the heating rate is 450 °C/hour. Kim and Lee [124] recovered the damage-free solar cells within 30 minutes and demonstrated the organic dissolution of EVA in O-dichlorobenzene is the most effective method. Pagnanelli et al. [125] utilized the thermal treatment approach to recover the metal and glass fractions, and discovered that the overall glass recovery rate could achieve 91%. Wang and Fthenakis [126] implemented Cd and Te separation based on different ion-exchange resins method during different time periods, and revealed that about 90% of recovery rate could be achieved. Azeumo et al. [127] demonstrated that the completed dissolution of EVA is less than one hour in toluene with the presence of ultrasonic radiation. What is more, in terms of the costs of PV recycling and disposal, Deng et al. [128] implemented a feasible financial evaluation of the recycling of PV panels waste by using the Monte Carlo simulation model, and illustrated that the landfill is the cheapest choice but it is not environmentally friendly. The glass recycling appears an economically viable choice, but it has a high cost. The thermal and mechanical recycling processing could reach $700–800/tonne and $400–500/tonne, respectively, resulting in around 30% cost reduction. Faircloth et al. [129] implemented an economic evaluation of the PV panel

waste on the basis of the discounted cash flow (DCF) approach to calculate the net present value (NPV) and discounted payback period (DPBT), and found that when the initial investment is $10.5 million, the NPV of the PV recycling is in the range between $3,048,277 and $2,812,554 with 5 and 13 years of DPBT.

To sum up, physical or mechanical processes have the cheapest cost, but they produce a huge amount of dust, toxic and a source of noise pollution, whereas the thermal and chemical processes are advanced and coupled technologies, but they consume a large amount of energy and generate the toxic gases [128, 130]. Additionally, the expense and production capacity of the current chemical treatment still require to be improved, and the chemical substance utilized still has serious hazards to human health and environment.

5. Important observations and recommendations for future study

The solar PV/T system with loop pipe and nanofluid is one of the greatest interest and challenge research domains, and regarded as a significant realization for enhancing PV/T energy conversion efficiency by taking into account the influences of geometrical shape, low-cost base materials, angle of placement, thermal and optical properties, wind speed, global irradiance, nanoparticle types, nanofluids concentration, mass flow rate and so on. Regardless of being a vanguard and promising technique, the solar PV/T technology still has some weaknesses and challenges that need to be promoted to form the framework for the future scope as below:

- For the existing PV/T configurations, it is necessary to optimize geometrical and structural parameters and investigate the dynamic performance for a long-time operating period. Meanwhile, new explorations with regard to the tube thickness, tube roughness, reflective coating and base fluid with high conductance should be conducted for the system performance enhancement.
- Current researches have been focused on transparent screens in clean condition for the PV/T performance improvement. As for the future research, the effects of dust and dirt on the system performance should be clarified. This is because there are low occurrence and intensity of rain in some regions.
- In terms of thermal insulation materials, few studies have paid attention to the natural materials, such as coconut and palm wood. As a result, more comprehensive investigations should be carried out, which contribute to accepting the merits and demerits of the natural materials in this field.
- This techno-economic models of the CPV/T system allow for the future assessment of economic competitiveness in different fields, such as domestic hot water heating, food processing, oil recovery and chemical refining.
- It is necessary to explore the additional base fluids. Other types of the base fluid, including ionic liquid, ethylene glycol-water mixture and oil liquid, should be evaluated by using experimental method. This could become the best alternative method to achieve the highest performance.

- The influences of magnetic nanofluids and hybrid nanofluids on the PV/T system performance should be assessed based on various anticipated optical and thermal properties. Furthermore, the influences of some novel nanostructures like borophene should be estimated.
- A complete and comprehensive computational fluid dynamic (CFD) model of the PV/T system with nanofluids must be developed in the future to elaborate the relevant mechanism of heat transfer and find the key criterion.
- The reliability of the PV/T system with nanofluid must be evaluated in terms of technical, economic and environmental aspects. This mainly includes non-toxic nanoparticle constituents, fabrication methods and low expense nanoparticles. Furthermore, the establishing of standards, protocols and regulation concerning the aspects of nanofluids applications is a vital matter for the future technical application.

6. Conclusions

This paper provides a comprehensive vision in the field of the solar PV/T system with loop-pipe and nanofluid to enhance the overall thermal and power energy output, it contributes to configuring the suitable absorber to attain the optimum performance and solves the barriers that limit the PV/T technology development. Furthermore, the solar PV/T system with nanofluid as working fluid exhibits greater overall energy efficiency. In the meantime, the influences of the critical parameters, such as nanoparticle category, volume fraction, inlet temperature, solar irradiation, mass flux and mass flow rates, have been evaluated. Therefore, some vital outcomes are illustrated as below:

- The advanced PV/T configurations, like U-tube, triangular tube and micro channels, increase the system energy efficiency approximately 15–30% and provide homogeneity temperature distribution compared to traditional ones. Furthermore, the most fitting titled angle of PV/T system is in the range between 25° and 35°.
- The configuration of micro-channels has become a prevalent research area owing to high reliability, low contact thermal resistance, leak-proof property, high heat transfer capability and cost-effective production.
- Nanofluids can be regarded as the future thermal working fluids for different applications owing to high heat transfer rate and thermal conductivity. Hence, more researches with regards to the fundamentals of heat transfer and the friction factors should be investigated in order to extend their applications.
- The PV/T system with nanofluid is more efficient with the energy efficiency improvement about 10%-20% compared to the system with the conventional working fluid like water.
- The higher concentration of nanofluid, the better of the PV/T system performance. Moreover, the dispersion of nanoparticles is a crucial influence factor for absorbing solar radiation to achieve high thermal conductivity.
- The hybrid nanofluids, such as CuO-MWCNT and Ag-$CoSO_4$, contribute to attaining high thermal and electrical energy output by controlling solar radiation transmitted to the PV module effectively.

- The dispersion of nanoparticles in PCM-nano like SiC-Paraffin is a novel solution to boost electrical efficiency owing to reducing PV cell temperature and solving the PCM low thermal conductivity problem.

Acknowledgments

We thank the authors of the cited references for granting the copyright and publishing permissions related to the figures included in this paper.

References

[1] Global emission. Analysis: Coronavirus set to cause largest ever annual fall in CO2 emissions. Available at: <https://www.carbonbrief.org/analysis-coronavirus-set-to-cause-largest-ever-annual-fall-in-co2-emissions> [Accessed 09 April 2020].

[2] Renewables 2020 global status report. Available at: <https://www.ren21.net/wp-content/uploads/2019/05/gsr_2020_full_report_en.pdf > [Accessed 11 December 2019].

[3] The Paris Agreement. Available at: < https://unfccc.int/process-and-meetings/the-paris-agreement/the-paris-agreement > [Accessed 09 January 2016].

[4] 2019 Global status report for buildings and construction. Available at: <https://www.worldgbc.org/news-media/2019-global-status-report-buildings-and-construction > [Accessed 11 December 2019].

[5] Climate change. Becoming carbon neutral by 2030. Available at: < https://new.brighton-hove.gov.uk/climate-change/becoming-carbon-neutral-2030> [Accessed 09 February 2020].

[6] Brahim T, Jemni A. Economical assessment and applications of photovoltaic/thermal hybrid solar technology: A review. Solar Energy 2017; 153: 540–561.

[7] Wu et al. A review of thermal absorbers and their integration methods for the combined solar photovoltaic/thermal (PV/T) modules. Renewable and Sustainable Energy Reviews 2017; 75: 839-854.

[8] Das D, Kalita P, Roy O. Flat plate hybrid photovoltaic-thermal (PV/T) system: A review on design and development. Renewable and Sustainable Energy Reviews 2018; 84: 111-130.

[9] Sultan SM, Efzan MNE. Review on recent Photovoltaic/Thermal (PV/T) technology advances and applications. Solar Energy 2018; 173: 939-954.

[10] Shafieian A, Khiadani M, Nosrati A. Strategies to improve the thermal performance of heat pipe solar collectors in solar systems: A review. Energy Conversion and Management 2019; 183: 307-331.

[11] Kalogirou SA, Karellas S, Badescu V, Braimakis K. Exergy analysis on solar thermal systems: A better understanding of their sustainability. Renewable Energy 2016; 85: 1328-1333.

[12] Chauhan A, Tyagi VV, Anand S. Minimum entropy generation and its validation against Hottel Whillier model for PV/T and FPC collectors. Solar Energy 2019; 188: 143-157.

[13] Ooshaksaraei P, Sopian K, Zulkifli R, Zaidi SH, Sirwan R. Performance of single pass photovoltaic thermal solar collector with bifacial solar cells. International Review of Mechanical Engineering 2013; 7(2): 358-363.

[14] Rashidi S, Y Liu, Khoosh-Ahang A, Jing D, Mahian O. Entropy generation analysis of different solar thermal systems. Environmental Science and Pollution Research 2020; 27: 20699–20724.

[15] Gholampour M, Ameri M. Energy and exergy study of effective parameters on performance of photovoltaic/thermal natural air collectors. Journal of Solar Energy Engineering 2014; 136: 1-11.

[16] Grubišić-Čabo F, Nižetić S, Marco T. Photovoltaic panels: A review of the cooling techniques. Transactions of FAMENA 2016; 40: 63-74.

[17] Elbreki AM, Alghoul MA, Sopiana K. Hussein T. Towards adopting passive heat dissipation approaches for temperature regulation of PV module as a sustainable solution. Renewable and Sustainable Energy Reviews 2017; 69: 961–1017.

[18] Skoplaki E, Palyvos J. On the temperature dependence of photovoltaic module electrical performance: a review of efficiency/power correlations. Solar Energy 2009; 83: 614–24.

[19] Farhana Z, Irwan YM, Azimmi RMN, Gomesh N. Experimental investigation of photovoltaic modules cooling system. 2012 IEEE Symposium on Computers & Informatics (ISCI), Penang, 2012, pp. 165-169.

[20] Du B, Hu E, Kolhe M. Performance analysis of water cooled concentrated photovoltaic (CPV) system. Renewable and Sustainable Energy Reviews 2012; 16: 6732–6736.

[21] Rosa-Clot M et al. Submerged photovoltaic solar panel: SP2. Renewable Energy 2010; 35; 1862–1865.

[22] Chandrasekar M et al. Passive cooling of standalone flat PV module with cotton wick structures. Energy Conversion and Management 2013; 71: 43–50.

[23] Maiti S et al. Self-regulation of photovoltaic module temperature in V-trough using a metal–wax composite phase change matrix. Solar Energy 2011; 85: 1805–1816.

[24] Tang X, Quan Z, Zhao Y. Experimental investigation of solar panel cooling by a novel micro heat pipe array. Energy and Power Engineering 2010; 2: 171-174

[25] Moradgholi M, Nowee SM, Abrishamchi I. Application of heat pipe in an experimental investigation on a novel photovoltaic/thermal (PV/T) system. Solar Energy 2014; 107: 82–88.

[26] Al-Shamani AN, Yazdi MH, Alghoul MA, Abed AM, Ruslan MH, Mat S, Sopian K. Nanofluids for improved efficiency in cooling solar collectors – A review. Renewable and Sustainable Energy Reviews 2014; 38: 348–367.

[27] Karami N, Rahimi M. Heat transfer enhancement in a PV cell using Boehmite nanofluid. Energy Conversion and Management 2014; 86: 275–285.

[28] Sardarabadi M, Passandideh-Fard M, Heris SZ. Experimental investigation of the effects of silica/water nanofluid on PV/T (photovoltaic thermal units). Energy 2014; 66: 264-272.

[29] Said Z, Arora S, Bellos E. A review on performance and environmental effects of conventional and nanofluid-based thermal photovoltaics. Renewable and Sustainable Energy Reviews. 2018; 94: 302-316.

[30] Saidur R, Leong KY, Mohammad HA. A review on applications and challenges of nanofluids. Renewable and Sustainable Energy Reviews 2011; 15: 1646–1668.

[31] Yazdanifard F, Ameri M, Ebrahimnia-Bajestan E. Performance of nanofluid-based photovoltaic/thermal systems: A review. Renewable and Sustainable Energy Reviews 2017; 76: 323-352.

[32] Muhammad MJ, Muhammad IA, Sidik NAC, Yazid MNAWM, Mamat R, Najafi G. The use of nanofluids for enhancing the thermal performance of stationary solar collectors: A review. Renewable and Sustainable Energy Reviews 2016; 63: 226-236.

[33] Khanafer K, Vafai K. A review on the applications of nanofluids in solar energy field. Renewable Energy 2018; 123: 398-406.

[34] Sahin AZ, Uddin MA, Yilbas BS, Al-Sharafi A. Performance enhancement of solar energy systems using nanofluids: An updated review. Renewable Energy 2020; 145:1126-1148.

[35] Verma SK, Tiwari AK. Progress of nanofluid application in solar collectors: A review. Energy Conversion and Management 2015; 100: 324-346.

[36] Li X, Chen W, Zou C. An experimental study on β-cyclodextrin modified carbon nanotubes nanofluids for the direct absorption solar collector (DASC): Specific heat capacity and photo-thermal conversion performance. Solar Energy Materials and Solar Cells 2020: 204: 110240.

[37] Goel N, Taylor RA, Otanicar T. A review of nanofluid-based direct absorption solar collectors: Design considerations and experiments with hybrid PV/Thermal and direct steam generation collectors. Renewable Energy 2020; 145: 903-913.

[38] Abbas N et al. Applications of nanofluids in photovoltaic thermal systems: A review of recent advances. Physica A: Statistical Mechanics and its Applications 2019; 536: 122513.

[39] Mallah AR, Zubir MNM, Alawi OA, Newaz KMS, Badry ABM. Plasmonic nanofluids for high photothermal conversion efficiency in direct absorption solar collectors: Fundamentals and applications. Solar Energy Materials and Solar Cells 2019; 201: 110084.

[40] Ahmadi MH, Ghazvini M, Sadeghzadeh M, Nazari MA, Ghalandari M. Utilization of hybrid nanofluids in solar energy applications: A review. Nano-Structures & Nano-Objects 2019; 20: 100386.

[41] Al-Waeli AHA, Sopian K, Kazem HA, Chaichan MT. Nanofluid based grid connected PV/T systems in Malaysia: A techno-economical assessment. Sustainable Energy Technologies and Assessments 2018; 28: 81-95.

[42] Hazra SK, Ghosh S, Nandi TK. Photo-thermal conversion characteristics of carbon black-ethylene glycol nanofluids for applications in direct absorption solar collectors. Applied Thermal Engineering 2019; 163: 114402.

[43] Kamyar A, Saidur R, Hasanuzzaman M. Application of computational fluid dynamics (CFD) for nanofluids. International Journal of Heat and Mass Transfer 2012; 55: 4104-4115.

[44] Purohit N, Jakhar S, Gullo P, Dasgupta MS. Heat transfer and entropy generation analysis of alumina/water nanofluid in a flat plate PV/T collector under equal pumping power comparison criterion. Renewable Energy 2018; 120: 14-22.

[45] Sadeghi R, Haghshenasfard M, Etemad SG, Keshavarzi E. Theoretical investigation of nanoparticles aggregation effect on water-alumina laminar convective heat transfer. International Communications in Heat and Mass Transfer 2016; 72: 57-63.

[46] Reeser A, Wang P, Bar-Cohen A. Energy efficient two-phase micro-cooler design for a concentrated photovoltaic triple junction cell. Proceedings of the ASME 2012 International Mechanical Engineering Congress & Exposition IMECE 2012, November 9-15, 2012, Houston, Texas, USA.

[47] Bianco V, Chiacchio F, Manca O, Nardini S. Numerical investigation of nanofluids forced convection in circular tubes. Apply Thermal Engineering 2009; 29: 3632-3642.

[48] Davarnejad R, Jamshidzadeh M. CFD modeling of heat transfer performance of MgO-water nanofluid under turbulent flow. Engineering Science and Technology, an International Journal 2015;18: 536-542.

[49] Hu M, Zheng R, Pei G, Wang Y, Li J, Ji J. Experimental study of the effect of inclination angle on the thermal performance of heat pipe photovoltaic/thermal (PV/T) systems with wickless heat pipe and wire-meshed heat pipe. Applied Thermal Engineering 2016; 106: 651–660.

[50] Li H, Sun Y. Operational performance study on a photovoltaic loop heat pipe/solar assisted heat pump water heating system. Energy and buildings 2018; 158: 861-872.

[51] Li H, Sun Y. Performance optimization and benefit analyses of a photovoltaic loop heat pipe/solar assisted heat pump water heating system. Renewable Energy 2019; 134: 1240-1247.

[52] Yu M, Diallo TMO, Zhao X, Zhou J, Du Z, Ji J, Cheng Y. Analytical study of impact of the wick's fractal parameters on the heat transfer capacity of a novel micro-channel loop heat pipe. Energy 2018; 158: 746-759.

[53] Diallo TMO, Yu M, Zhou J, Zhao X, Ji J, Hardy D. Analytical investigation of the heat-transfer limits of a novel solar loop-heat pipe employing a mini-channel evaporator. Energies 2018; 11:148.

[54] Yu et al. Experimental investigation of a novel solar micro-channel loop-heat-pipe photovoltaic/thermal (MC-LHP-PV/T) system for heat and power generation. Applied Energy 2019; 256: 113929.

[55] Sarafraz MM, Pourmehran O, Yang B, Arjomandi M. Assessment of the thermal performance of a thermosyphon heat pipe using zirconia-acetone nanofluids. Renewable Energy 2019; 136: 884-895.

[56] Sarafraz MM, Goodarzi M, Tlili I, Alkanhal T A, Arjomandi M. Thermodynamic potential of a high-concentration hybrid photovoltaic/thermal plant for co-production of steam and electricity. Journal of Thermal Analysis and Calorimetry. Available at < https://doi.org/10.1007/s10973-020-09914-2> [Accessed 21.06. 2020].

[57] Widyolar B et al. Design, simulation and experimental characterization of a novel parabolic trough hybrid solar photovoltaic/thermal (PV/T) collector. Renewable Energy 2017; 101: 1379-1389.

[58] Abdelhamid et al. Novel double-stage high-concentrated solar hybrid photovoltaic/thermal (PV/T) collector with nonimaging optics and GaAs solar cells reflector. Applied Energy; 2016; 182: 68-79.

[59] Zhou C, Liang R, Zhang J, Riaz A. Experimental study on the cogeneration performance of roll-bond-PVT heat pump system with single stage compression during summer. Applied Thermal Engineering 2019; 149: 249-261.

[60] Zhou C, Liang R, Riaz A, Zhang J, Chen J. Experimental investigation on the tri-generation performance of roll-bond photovoltaic thermal heat pump system during summer. Energy Conversion and Management 2019; 184: 91-106.

[61] Lu S, Liang R, Zhang J, Zhou C. Performance improvement of solar photovoltaic/thermal heat pump system in winter by employing vapor injection cycle. Applied Thermal Engineering 2019; 155: 135–146.

[62] Fayaz H, Nasrin R, Rahim NA, Hasanuzzaman M. Energy and exergy analysis of the PVT system: Effect of nanofluid flow rate. Solar Energy 2018; 169: 217-230.

[63] Nasrin R, Rahim NA, Fayaz H, Hasanuzzaman M. Water/MWCNT nanofluid based cooling system of PVT: Experimental and numerical research. Renewable Energy 2018; 121: 286-300.

[64] Abdallah SR, Saidani-Scott H, Abdellatif OE. Performance analysis for hybrid PV/T system using low concentration MWCNT (water-based) nanofluid. Solar Energy 2019; 181: 108-115.

[65] Aste N, Pero CD, Leonforte F, Manfren M. Performance monitoring and modeling of an uncovered photovoltaic-thermal (PVT) water collector. Solar Energy 2016; 135: 551-568.

[66] Zhang P, Rong X, Yang X, Zhang D. Design and performance simulation of a novel hybrid PV/T-air dual source heat pump system based on a three-fluid heat exchanger. Solar Energy 2019; 191: 505-517.

[67] Khelifa A, Touafek K, Moussa HB, Tabet I. Modeling and detailed study of hybrid photovoltaic thermal (PV/T) solar collector. Solar Energy 2016; 135: 169-176.

[68] Zhou J, Zhao X, Ma X, Qiu Z, Ji J, Du Z, Yu M. Experimental investigation of a solar driven direct-expansion heat pump system employing the novel PV/micro-channels-evaporator modules. Applied Energy 2016; 178: 484-495.

[69] Zhou J, Na X, Zhao X, Yuan Y, Yu M, Li J. Numerical simulation and experimental validation of a micro-channel PV/T modules based direct-expansion solar heat pump system. Renewable Energy 2020; 145: 1992-2004.

[70] Hou L, Quan Z, Zhao Y, Wang L, Wang G. An experimental and simulative study on a novel photovoltaic-thermal collector with micro heat pipe array (MHPA-PV/T). Energy and Buildings 2016; 124: 60-69.

[71] Wang G, Zhao Y, Quan Z, Tong J. Application of a multi-function solar-heat pump system in residential buildings. Applied Thermal Engineering 2018; 130: 922-937.

[72] Zhu T, Diao Y, Zhao Y, Li F. Thermal performance of a new CPC solar air collector with flat micro-heat pipe arrays. Applied Thermal Engineering 2016; 98: 1201-1213.

[73] Korres D, Tzivanidis C. A new mini-CPC with a U-type evacuated tube under thermal and optical investigation. Renewable Energy 2018; 128: 529-540.

[74] Gu Y, Zhang X, Myhren JA, Han M, Chen X, Yuan Y. Techno-economic analysis of a solar photovoltaic/thermal (PV/T) concentrator for building application in Sweden using Monte Carlo method. 2018; 165: 8-24.

[75] Riggs BC et al. Techno-economic analysis of hybrid PV/T systems for process heat using electricity to subsidize the cost of heat. Applied Energy 2017; 208: 1370-1378.

[76] Boudries R et al. Techno-economic assessment of solar hydrogen production using CPV-electrolysis systems. Energy Procedia 2016; 93: 96-101.

[77] Gunasekar N, Mohanraj M, Velmurugan V. Artificial neural network modeling of a photovoltaic-thermal evaporator of solar assisted heat pumps. Energy 2015; 93: 908-922.

[78] Jouhara H, Milko J, Danielewicz J, Sayegh MA, Szulgowska-Zgrzywa M, Ramos JB, Lester SP. The performance of a novel flat heat pipe based thermal and PV/T (photovoltaic and thermal systems) solar collector that can be used as an energy-active building envelope material. Energy 2016; 108: 148-154.

[79] Jouhara H, Szulgowska-Zgrzywa M, Sayegh MA, Milko J, Danielewicz J, Nannou TK, Lester SP. The performance of a heat pipe based solar PV/T roof collector and its potential contribution in district heating applications. Energy 2017; 136: 117-125.

[80] Khordehgah K, Guichet V, Lester SP, Jouhara H. Computational study and experimental validation of a solar photovoltaics and thermal technology. Renewable Energy 2019; 143: 1348-1356.

[81] Ghaderian J, Sidik NAC. An experimental investigation on the effect of Al_2O_3/distilled water nanofluid on the energy efficiency of evacuated tube solar collector. International Journal of Heat and Mass Transfer 2017; 108: 972–987.

[82] Tong Y, Lee H, Kang W, Cho H. Energy and exergy comparison of a flat-plate solar collector using water, Al_2O_3 nanofluid, and CuO nanofluid. Applied Thermal Engineering 2019; 159: 113959.

[83] Ghaderian J et al. Performance of copper oxide/distilled water nanofluid in evacuated tube solar collector (ETSC) water heater with internal coil under thermosyphon system circulations. Applied Thermal Engineering 2017; 121: 520–536.

[84] Qu J, Zhang R, Wang Z, Wang Q. Photo-thermal conversion properties of hybrid CuO-MWCNT/H2O nanofluids for direct solar thermal energy harvest. Applied Thermal Engineering 2019; 147: 390-398.

[85] Al-Waeli AHA, Sopian K, Chaichan MT, Kazem HA, Hasan HA, Al-ShamaniAN. An experimental investigation of SiC nanofluid as a base-fluid for a photovoltaic thermal PV/T system. Energy Conversion and Management 2017; 142: 547–558.

[86] Al-Waeli AHA, Sopian K, Chaichan MT, Kazem HA, Ibrahim A, Mat S, Ruslan MH. Evaluation of the nanofluid and nano PCM based photovoltaic thermal (PVT) system: An experimental study. Energy Conversion and Management 2017; 151: 693–708.

[87] Al-Waeli AHA, Sopian K, Chaichan MT, Kazem HA, Ibrahim A, Mat S, Ruslan MH. Comparison of prediction methods of PV/T nanofluid and nano-PCM system using a measured dataset and artificial neural network. Solar Energy 2018; 162; 378–396.

[88] Aberoumand S, Ghamari S, Shabani B. Energy and exergy analysis of a photovoltaic thermal (PV/T) system using nanofluids: An experimental study. Solar Energy 2018; 165: 167-177.

[89] Han X, Chen X, Wang Q, Alelyani SM, Qu J. Investigation of CoSO4-based Ag nanofluids as spectral beam splitters for hybrid PV/T applications. Solar Energy 2019; 177: 387-394.

[90] Dehaj MS, Mohiabadi MZ. Experimental investigation of heat pipe solar collector using MgO nanofluids. Solar Energy Materials and Solar Cells 2019; 191: 91-99.

[91] Sharafeldin MA, Gróf G. Evacuated tube solar collector performance using CeO2/water nanofluid. Journal of Cleaner Production 2018; 185: 347-356.

[92] Sharafeldin MA, Gróf G. Efficiency of evacuated tube solar collector using WO3/Water nanofluid. Renewable Energy 2019; 134: 453-460.

[93] Ebaid MSY, Ghrair AM, Al-Busoul M. Experimental investigation of cooling photovoltaic (PV) panels using (TiO_2) nanofluid in water -polyethylene glycol mixture and (Al_2O_3) nanofluid in water- cetyltrimethylammonium bromide mixture. Energy Conversion and Management 2018; 55: 324-343.

[94] Sarafraz MM, Safaei MR. Diurnal thermal evaluation of an evacuated tube solar collector (ETSC) charged with graphene nanoplatelets-methanol nano-suspension. Renewable Energy 2019; 142: 364-372.

[95] Sarafraz, MM, Tlili, I, Tian, Z, Bakouri, M, Safaei, MR, Goodarzi, M. Thermal evaluation of graphene nanoplatelets nanofluid in a fast-responding HP with the potential use in solar systems in smart cities. Applied Science 2019; 9: 2101.

[96] Sarafraz MM, Tlili I, Baseer MA, Safari, MR. Potential of solar collectors for clean thermal energy production in smart cities using nanofluids: experimental assessment and efficiency improvement. Applied Science 2019; 9: 1877.

[97] Sardarabadi M, Hosseinzadeh M, Kazemian A, Passandideh-Fard M. Experimental investigation of the effects of using metal-oxides/water nanofluids on a photovoltaic thermal system (PVT) from energy and exergy viewpoints. Energy 2017; 138: 682-695.

[98] Eidan AA, AlSahlani A, Ahmed AQ, Al-fahham M, Jalil JM. Improving the performance of heat pipe-evacuated tube solar collector experimentally by using Al_2O_3 and CuO/acetone nanofluids. Solar Energy 2018; 173: 780-788.

[99] Mercan M, Yurddaş A. Numerical analysis of evacuated tube solar collectors using nanofluids. Solar Energy 2019; 191: 167-179.

[100] Al-Waeli AHA, Chaichan MT, Kazem HA, Sopian K. Comparative study to use nano-(Al_2O_3, CuO, and SiC) with water to enhance photovoltaic thermal PV/T collectors. Energy Conversion and Management 2017; 148: 963-973.

[101] Bell labs. The Solar Battery Available at: <https://www.beatriceco.com/bti/porticus/bell/belllabs_photov oltaics.html>.

[102] Khatibi A, Astaraei FR, Ahmadi MH. Generation and combination of the solar cells: A current model review. Energy Science Engineering 2019; 7: 305–322.

[103] Ahmadi MH et al. Solar power technology for electricity generation: a critical review. Energy Science Engineering 2018; 6 (5): 340-361.

[104] What is thin-film solar? Available at: <https://solarfeeds.com/wiki/thin-film-solar/#Types_of_Thin-film_Solar_cells> [Accessed February 2020].

[105] Multijunction III-V Photovoltaic Research. Available at < https://www.energy.gov/eere/solar/multijunction-iii-v-photovoltaics-research>.

[106] Next-generation solar panels boost efficiency but may carry toxic risks. Available at: <https://theconversation.com/next-generation-solar-panels-boost-efficiency-but-may-carry-toxic-risks-130921> [Accessed 25 March 2020].

[107] Siegler TD, Shimpi TM, Sampath WS, Korgel BA. Development of wide bandgap perovskites for next-generation low-cost CdTe tandem solar cells. Chemical Engineering Science 2019; 199: 388–397.

[108] Tala-Ighil R. Handbook of nanoelectrochemistry. Springer International Publishing Switzerland. Available at: < https://link.springer.com/content/pdf/10.1007%2F978-3-319-15207-3_26-1.pdf > [Accessed July 2015].

[109] Jovanoviæ U, Manèiæ D, Jovanoviæ I, Petrušiæ Z. Temperature measurement of photovoltaic modules using non-contact infrared system. Journal of Electrical Engineering and Technology 2017; 12 (2): 904-910.

[110] Jankovec M, Topi.c M. Intercomparison of temperature sensors for outdoor monitoring of photovoltaic modules. Journal of Solar Energy Engineering 2013; 135 (3): 31012-31017.

[111] Cao Y et al. In situ contactless thermal characterisation and imaging of encapsulated photovoltaic devices using phosphor thermometry. Progress in Photovoltaics 2019; 27: 673–681.

[112] Lopez-Garcia J, Pavanello D, Sample T. Analysis of temperature coefficients of bifacial crystalline silicon PV modules. IEEE Journal of Photovoltaics 2018; 8(4): 960-968.

[113] Buerhop C, Schlegel D, Niess M, Vodermayer C, Weißmann R, Brabec CJ. Reliability of IR-imaging of PV-plants under operating conditions. Solar Energy Mater Solar Cells 2012; 107:154-164.

[114] Sadat S, Meyhofer E, Reddy P. High resolution resistive thermometry for micro/nanoscale measurements. Review of Scientific Instruments 2012; 83: 084902.

[115] Shin J, Park J, Park N. A method to recycle silicon wafer from end-of-life photovoltaic module and solar panels by using recycled silicon wafers. Solar Energy Materials & Solar Cells 2017; 162: 1–6.

[116] Deng R, Chang NL, Ouyang Z, Chong CM. A techno-economic review of silicon photovoltaic module recycling. Renewable and Sustainable Energy Reviews 2019; 109: 532-550.

[117] Chowdhury MS, Rahman KS, Chowdhury T, Nuthammachot N, Techato K, Akhtaruzzaman M, Tiong S. An overview of solar photovoltaic panels' end-of-life material recycling. Energy Strategy Reviews 2020; 27: 100431.

[118] Conference record of the, IEEE Electron Devices Society., & Institute of Electrical and Electronics Engineers, IEEE Photovoltaic Specialists Conference, New York, 1970. Institute of Electrical and Electronics Engineers).

[119] E.P.S.E. Conference, 20th European Photovoltaic Solar Energy Conference: Proceedings of the International Conference Held in Barcelona, WIP-Renewable Energies, Spain, 2005, 6-10 June 2005.

[120] Doi T, Tsuda I, Unagida H, Murata A, Sakuta K, Kurokawa K. Experimental study on PV module recycling with organic solvent method. Solar Energy Materials and Solar Cells 2001; 67 (1-4): 397-403.

[121] The opportunities of solar panel recycling. Available at: <https://www.greenmatch.co.uk/blog/2017/10/the-opportunities-of-solar-panel-recycling> [Accessed 10 March 2020]

[122] Dias P, Schmidt L, Gomes LB, Bettanin A, Veit H, Bernardes AM. Recycling waste crystalline silicon photovoltaic modules by electrostatic separation. Journal of Sustainable Metallurgy 2018; 4: 176–186.

[123] Fiandra V, Sannino L, Andreozzi C, Corcelli F, Graditi G. Silicon photovoltaic modules at end-of-life: removal of polymeric layers and separation of materials. Waste Management 2019; 87: 97–107.

[124] Kim Y, Lee J. Dissolution of ethylene vinyl acetate in crystalline silicon PV modules using ultrasonic irradiation and organic solvent. Solar Energy Material Solar Cells 2012; 98: 317–322.

[125] Pagnanelli F, Moscardini E, Granata G, Atia TA, Altimari P, Havlik T, Toro L. Physical and chemical treatment of end of life panels: an integrated automatic approach viable for different photovoltaic technologies, Waste Management 2017; 59: 422–431.

[126] Wang W, Fthenakis V. Kinetics study on separation of cadmium from tellurium in acidic solution media using ion-exchange resins. Journal of Hazardous Materials 2005; 125 (1–3): 80–88.

Nomenclature

A	Area (m^2)
c_p	Heat capacity of fluid (kJ/kg·K)
h	Heat transfer coefficient [W/(m·K)]
m	Mass flow rate (kg/s)
P	Pressure (k·Pa)
Q	Energy (kW)
T	Temperature (°C)

t	Time (s)

Greek Letters

α	Absorptivity
β	Title-angle of PV panels
γ	PV cell temperature coefficient ($°C^{-1}$)
λ	Thermal conductivity (W/m·K)
σ	Stefan-Boltzmann constant (5.67×10^{-8} $W/m^2 \cdot K^4$)
η	Efficiency (%)
τ	Transmittance
ε	PV cell conversion factor

Abbreviations

Al_2O_3	Aluminum-oxide
ANN	Artificial neural networks
ASHP	Air source heat pump
a-Si	Amorphous silicon
CdTe	Cadmium telluride
CeO_2	Cerium oxide
CFD	Computational fluid dynamic
CIGS	Copper indium gallium selenide
COP	Coefficient of performance
COV	Coefficient of variance
CPC	Compound parabolic concentrator
CPV/T	Concentrated photovoltaic/thermal

CuO	Copper-oxide
CZTS	Copper zinc tin sulphide solar cell
DCF	Discounted cash flow
DPBT	Discounted payback period
DSSC	Dye-sensitized
EEW	Electrical explosion of wire
EOL	End-of-life
FESEM	Field emission scanning electron microscope
FMHPA	Flat micro-heat pipe arrays
GaAs	Gallium Arsenide
GaInP	Gallium indium phosphide
Ge	Germanium
GHG	Greenhouse gases
Hg	Tribute
HPSC	Heat pipe solar collector
InGaAs	Indium gallium arsenide
LCOE	Levelized cost of energy
LHP	Loop heat pipe
MCLHP	Micro-channel loop heat pipe
MF	Merit function
MgO	Magnesium oxide
MHPA	Micro heat pipe array
MWCNT	Multi-walled carbon nanotube
NDC	Nationally determined contribution

NPV	Net present value
OPV	Organic or polymer
PCM	Phase change material
PP	Payback period
PV	Photovoltaic
PV-HP	Photovoltaic with heat pump
PV/T	Photovoltaic/thermal
RB	Roll bond
RMS	Root mean square
SAC	Solar air collector
SAHP	Solar-assisted heat-pump
SEM	Scanning electron microscopy
SiC	Silicon carbide
TEM	Transmission electronic microscope
Ti_2O_3	Titanium-oxide
TPT	Tedlar-Polyester-Tellar
TRNSYS	TRaNsient system simulation
VI	Vapor injection
WGBC	World green building council
WO_2	Tungsten oxide
WSHP	Water source heat pump
XRD	X-ray diffraction
ZnO	Zinc-oxide
ZrO_2	Zirconia-oxide